TECHNISCHE UNIVERSITÄT DARMSTADT

Towards the engineering of a magneto sensitive potassium channel

at the Department of Biology

of the Technischen Universität Darmstadt

submitted in fulfilment of the requirements for the degree of *Doctor rerum naturalium*
(Dr. rer. nat.)

Doctoral thesis

by Lorenzo Brocca

First assessor: Prof. Gerhard Thiel

Second assessor: Prof. Adam Bertl

Darmstadt 2021

Table of contents

Abstract **1**

Zusammenfassung **3**

List of abbreviations **5**

List of figures **6**

Introduction **7**

Optogenetics: controlling neuronal activity with light gated ion channels 7

Magneto-genetics: a promising alternative to optogenetics 9

Are magneto-genetic tools acting through a temperature-regulated mechanism? 11

How to evaluate mechanical and thermal effects of magnetic fields on ferritins 15

The need to build a temperature sensitive K^+ channel 18

Viral Potassium channels can be efficiently engineered with heterologous domains 20

Aim of the thesis **22**

Material and methods **23**

Molecular biology 23

Cell culture and transfection 24

Confocal imaging 24

Electrophysiology 24

Temperature experiments 25

Magnetic field stimulation 25

Cell membrane bursting 25

TICK1-HA immunofluorescence 26

Ferritin crude lysate and purification 26

Protein native gel 26

Dynamic Light Scattering (DLS) 27

Purification and temperature dependence analysis of mT-Sapphire and mCherry 27

gTEMP2 tested in HEK cells 27

Raster Image Correlation Spectroscopy (RICS) measurements 28

Inductively coupled plasma atomic emission spectroscopy (ICP-OES) 28

Result and discussion **29**

Chapter 1: Engineering temperature sensitivity in the potassium channel Kcv_{NTS} 29

Addition of the temperature domain to Kcv_{NTS} 31
Functional test of v1 and v2 constructs 32
The synthetic Kcv_{NTS} constructs are localized in the plasma membrane 34
The synthetic channel v1 can be efficiently activated by an increase in temperature 36
Single point mutations in the CTD of v1 affect the temperature dependence of the channel . 38
TICK1 trafficking is lower than other well-trafficking ion channels 42
Activation-deactivation kinetics of TICK1 are in the second to minute range 43
TICK1 opening is in the range of tens of seconds 45
TICK1 closure kinetic is highly variable, ranging from few to tens of minutes 47
Chapter 2: Engineering magneto sensitivity in the temperature-dependent potassium channel 49
Iron content of ferritins extracted from HEK 293 cells 50
Purified EGFP-mFT disassembles in native protein gel 54
EGFP-mFT contains 583 Fe atoms for each protein 55
A novel approach to accurate temperature measurements 57
Further steps towards MAGNETO: connecting the ferritin moiety to the TICK channel 60
Oscillating magnetic field can triggers the opening of MagKCV 63
20% of cells expressing MagKCV shows channel activation after MF 65
Further experiments are required to assess the magnetic activation of MagKCV 67
Conclusions 68
Bibliography 70
Declaration of own work 78
Acknowledgments 79
Curriculum Vitae 80
Ehrenwörtliche Erklärung 82

Abstract

Optogenetics is the most widely used technique employed by neuroscientists to control neuronal activity with high spatial and temporal resolution either *in vitro* and *in vivo*. Optogenetics relies on naturally occurring or synthetic ion channels whose gating is controlled by light. Both excitatory and inhibitory optogenetic tools are currently available to remotely promote or prevent neuronal firing. Inhibitory tools are of particular interest as therapeutic agent for the treatment of neuropathic pain, a pathology caused by nerve lesion/inflammation that generates uncontrolled firing in peripheral sensory neurons. Given the limited penetration of light into tissues that greatly hampers the usage of optogenetic tools *in vivo*, the search is on for novel, alternative ways to stimulate inhibitory tools. Magneto-genetics was recently proposed as an alternative technique to optogenetics. It relies on the capability of external magnetic fields, which deeply penetrate into tissues, to activate ion channels. Initially, the heat-activated channel TRPV1 was conjugated to exogenously supplied iron oxide nanoparticles. The latter generate heat in response to an oscillating magnetic field and this rise in temperature is responsible for the opening of TRPV1. In the second generation of magneto-genetic tools the TRPV channels (TRPV1-4) have been linked to ferritin, a 24-mer protein forming an hollow sphere that can store up to 4500 iron atoms. Activation of ferritin-engineered TRPV channels by oscillating magnetic fields was reported to occur both *in vitro* and *in vivo* experiments. The physical principle behind the working mechanism of magneto-genetic tools is unclear and presently debated. However, in the case of Magneto2.0, a TRPV4-based channel, it was shown experimentally that opening is due to the rise in temperature, generated by ferritin upon exposure to an oscillating magnetic field.

To date, all magneto-genetic tools use TRPV channels, which mainly conduct calcium, magnesium and sodium ions, limiting the spectrum of application of these tools to neuronal excitation. The aim of this work is to generate a potassium (K^+) magneto-genetic tool, with the long term aim to use it in the treatment of neuropathic pain. In nature, all known temperature-sensitive potassium channels are polymodal, i.e., they respond to a number of stimuli, beside temperature. This finding motivated us to engineer a member of the viral potassium channel family, Kcv Next to Smith (Kcv_{NTS}), into a temperature sensitive channel. To this end, we fused at its C terminus the cytosolic domain of the temperature sensitive bacterial sodium channel Na_vAe1. One of the engineered constructs, called v1, showed the wanted property of being closed at 37°C and open >45°C. We introduced single point mutations in the C-terminal of v1 to fine-tune the temperature range of gating. Mutation M267A decreased the opening temperature of the channel from 45°C to 40°C, making this a good tool for mammals. The M267A mutant was renamed “Temperature Induced Channel for K^+” (TICK1). TICK1 activation and deactivation kinetics were characterized, showing an activation τ of around 10 seconds and a variable deactivation τ, ranging from 66 to 672 seconds.

In parallel, we also characterized the ferritin that we intended to connect to TICK. According to Stanley et al, 2015, the moiety is formed by a dimer, obtained by the fusion of light and heavy chain monomers. This ensures a light/heavy chain ratio of 1:1, which was reported to increase the iron uptake. We further added a EGFP at the N terminus of the dimer and demonstrated that this construct, construct EGFP-mFT, assembles into 12mer ferritins in HEK293 cells. We then tested by

correlation spectroscopy if magnetic fields affect the engineered ferritins, but no changes in diffusion coefficients were found in the presence of static magnetic fields. Purified ferritins were further analyzed by Inductively coupled plasma - optical emission spectrometry (ICP-OES) to measure their iron content, revealing that each ferritin in average contains 583 atoms of iron, a result in accordance with the physiological iron content of mammalian ferritins.

As a next step we built our magneto-genetic tool: TICK1 was modified with an N-terminal EGFP nanobody (nanoTICK1) and this construct was co-expressed in HEK293T cells with EGFP-mFT. The nanobody ensures the binding of ferritin to the channel that was renamed MagKCV. After preliminary testing proper MagKCV membrane localization and temperature activation, we investigated the magnetic properties of this synthetic channel. An experimental setup was built with a cylindrical permanent magnet manually moved back and forth from the cell at 1Hz generating a maximum magnetic field of around 50mT. Experiments were conducted with cells maintained at 37°C. Around 20% of tested cells expressing MagKCV showed an activation of the channel in response to magnetic field. The activation of MagKCV is slower than the one of TICK1, but still maintains the typical TICK1 current-voltage relationship and barium sensitivity. In the control condition, with no magnetic field exposure, 1cell over 40 tested (2,5%) showed an open channel, indicating that MagKCV might be slightly less regulated than TICK1 (100% of temperature regulation, n=37). MagKCV appears to be a promising prototype for the development of the first K+ magneto-genetic tool.

Zusammenfassung

Die Optogenetik ist die am weitesten verbreitetese Technik, die von Neurowissenschaftlern zur Steuerung der neuronalen Aktivität mit hoher räumlicher und zeitlicher Auflösung *in vitro* und *in vivo* eingesetzt wird. Optogenetik stützt sich auf natürlich vorkommende oder synthetische Ionenkanäle, deren Gating durch Licht gesteuert wird. Derzeit sind sowohl exzitatorische als auch inhibitorische optogenetische Werkzeuge verfügbar, um elektrische Aktivität in Neuronen aus der Ferne zu fördern oder zu verhindern. Inhibitorische Werkzeuge sind von besonderem Interesse als therapeutische Mittel für die Behandlung von neuropathischen Schmerzen, einer Pathologie, die durch Nervenläsionen/Entzündungen verursacht wird und unkontrolliertes Feuern in peripheren sensorischen Neuronen erzeugt. Angesichts der begrenzten Eindringtiefe von Licht in Gewebe, die den Einsatz optogenetischer Werkzeuge *in vivo* stark behindert, wird nach neuen, alternativen Wegen zur Stimulierung hemmender Werkzeuge gesucht. Vor kurzem wurde die Magneto-Genetik als alternative Technik zur Optogenetik vorgeschlagen. Sie beruht auf der Fähigkeit externer Magnetfelder, die tief in das Gewebe eindringen, Ionenkanäle zu aktivieren. Dazu wurde zunächst der hitzeaktivierte Kanal TRPV1 mit exogen zugeführten Eisenoxid-Nanopartikeln konjugiert. Letztere erzeugen als Reaktion auf ein oszillierendes Magnetfeld Wärme und dieser Temperaturanstieg ist für die Öffnung von TRPV1 verantwortlich. In der zweiten Generation von magneto-genetischen Werkzeugen wurden die TRPV-Kanäle (TRPV1-4) mit Ferritin verknüpft, einem 24-meren Protein, das eine Hohlkugel bildet, die bis zu 4500 Eisenatome speichern kann. Die Aktivierung von TRPV-Kanälen mit Ferritin durch oszillierende Magnetfelder wurde sowohl *in vitro* als auch *in vivo* Experimenten nachgewiesen. Das physikalische Prinzip, das hinter dem Wirkmechanismus der magneto-genetischen Werkzeuge steht, ist unklar und wird derzeit diskutiert. Im Fall von Magneto2.0, einem TRPV4-basierten Kanal, konnte jedoch experimentell gezeigt werden, dass die Öffnung auf den Temperaturanstieg zurückzuführen ist, der durch Ferritin bei Einwirkung eines oszillierenden Magnetfelds erzeugt wird.

Bislang verwenden alle magneto-genetischen Werkzeuge TRPV-Kanäle, die hauptsächlich Kalzium-, Magnesium- und Natriumionen leiten, was das Anwendungsspektrum dieser Werkzeuge auf neuronale Erregung beschränkt. Ziel dieser Arbeit ist es, ein magnetogenetisches Werkzeug für Kalium (K^+) zu entwickeln, das langfristig zur Behandlung von neuropathischen Schmerzen eingesetzt werden soll. In der Natur sind alle bekannten temperatursensitiven Kaliumkanäle polymodal, d. h. sie reagieren auf eine Reihe von Reizen neben der Temperatur. Diese Erkenntnis hat uns dazu motiviert, ein Mitglied der viralen Kaliumkanalfamilie, Kcv Next to Smith (Kcv_{NTS}), in einen temperaturempfindlichen Kanal zu verwandeln. Zu diesem Zweck haben wir die zytosolische Domäne des temperaturempfindlichen bakteriellen Natriumkanals NavAe1 an seinen C-Terminus fusioniert. Eines der Konstrukte, v1 genannt, zeigte die gewünschte Eigenschaft, bei 37°C geschlossen und >45°C geöffnet zu sein. Wir führten einzelne Punktmutationen in den C-Terminus von v1 ein, um den Temperaturbereich für das Gating den Kanals fein abzustimmen. Die Mutation M267A verringerte dabei die kritische Öffnungstemperatur des Kanals von 45°C auf 40°C, was ihn zu einem guten Werkzeug für Säugetiere macht. Die M267A-Mutante wurde in "Temperaturinduzierter Kanal für K^+" (TICK1) umbenannt. Die Aktivierungs- und Deaktivierungskinetik von TICK1 wurde charakterisiert. Sie zeigt eine exponentill zunehmende

Aktivierung mit einer Zeitkonstante τ von etwa 10 Sekunden; die Deaktivierung ist varaibale mit τ Weren zwischen 66 und 672 Sekunden.

Parallel dazu haben wir auch das Ferritin charakterisiert, das wir mit TICK verbinden wollten. Nach Literaturangaben wird eine Ferritin Einheit durch ein Dimer gebildet, das durch die Fusion von Monomeren der leichten und schweren Kette entsteht. Dies gewährleistet ein Verhältnis von leichter zu schwerer Kette von 1:1, was Berichten zufolge die Eisenaufnahme erhöht. Wir fügten außerdem ein grün fluoreszierendes Protein (EGFP) am N-Terminus des Dimers hinzu und wiesen nach, dass dieses Konstrukt, EGFP-mFT, in HEK293-Zellen zu 12mer-Ferritinen assembliert. Anschließend testeten wir mittels Korrelationsspektroskopie, ob Magnetfelder die konstruierten Ferritine beeinflussen. In diesen Experimenten wurden jedoch keine Veränderungen der Diffusionskoeffizienten in Gegenwart statischer Magnetfelder festgestellt. Gereinigte Ferritine wurden weiter mit induktiv gekoppeltem Plasma - optischer Emissionsspektrometrie (ICP-OES) analysiert, um ihren Eisengehalt zu messen. Dabei zeigte sich, dass jedes Ferritin im Durchschnitt 583 Eisenatome enthält, ein Ergebnis, das mit dem physiologischen Eisengehalt von Säugetierferritinen übereinstimmt.

In einem nächsten Schritt bauten wir unser magneto-genetisches Werkzeug: TICK1 wurde dazu mit einem N-terminalen EGFP-*Nanobody* (nanoTICK1) modifiziert und dieses Konstrukt wurde in HEK293T-Zellen zusammen mit EGFP-mFT exprimiert. Der *Nanobody* gewährleistet die Bindung von Ferritin an den Kanal, der in MagKCV umbenannt wurde. Nach ersten Tests zur korrekten Membranlokalisierung und Temperaturaktivierung von MagKCV haben wir die magnetischen Eigenschaften dieses synthetischen Kanals untersucht. Dazu wurde ein Versuchsaufbau mit einem zylindrischen Dauermagneten aufgebaut, der manuell mit 1 Hz von der Zelle hin und her bewegt wurde und ein maximales Magnetfeld von etwa 50 mT erzeugte. Die Experimente wurden mit Zellen durchgeführt, die bei 37°C gehalten wurden. Etwa 20% der getesteten Zellen, die MagKCV exprimieren, zeigten eine Aktivierung des Kanals als Reaktion auf das Magnetfeld. Die Aktivierung von MagKCV ist langsamer als die von TICK1, behält aber immer noch die typische TICK1-Strom-Spannungs-Eigenschaften und die Bariumempfindlichkeit bei. In der Kontrollbedingung, ohne Magnetfeld-Exposition, zeigten nur 1 von 40 getesteten Zellen (2,5%) einen offenen Kanal, was darauf hindeutet, dass MagKCV etwas weniger reguliert sein könnte als TICK1 (100%ige Temperaturregulation, n=37). MagKCV scheint ein vielversprechender Prototyp für die Entwicklung des ersten magneto-genetischen K^+-Tools zu sein.

List of abbreviations

Wt	Wild type
HEK	Human Embryonic Kidney cells
TM	Transmembrane
TMD	Transmembrane domain
CTD	C-terminal domain
MF	Magnetic field stimulation
Mw	Molecular weight
TICK1	Temperature Induced Channel for K^+
MagKCV	Magnetic Kcv
ROS	Reactive oxygen species
RF	Radio frequency
FCS	Fluorescence Correlation Spectroscopy
RICS	Raster Image Correlation Spectroscopy
ICP-OES	Inductively coupled plasma atomic emission spectroscopy
EGFP	Enhanced Green Fluorescent Protein
Kcv_{NTS}	Kcv Next to Smith
PAGE	Poly Acrylamide Gel Electrophoresis
N.t.	Not transfected
mFT	Mouse ferritin
hFTH	Human ferritin heavy chain gene
Pf-FT	*Pyrococcus furiosus* ferritin
E. coli	*Escherichia coli*
Ex / Em	Excitation / Emission

List of figures

Figure 1: Controlling neuronal excitability with optogenetic tools. 8
Figure 2: Development and evolution of magneto-genetic tools. 11
Figure 3: Experimental analysis of "Magneto2.0" demonstrate the temperature activation pathway. 13
Figure 4: Fluorescence Correlation Spectroscopy and temperature-sensitive fluorescent proteins can be used to evaluate the ferritin magnetic properties. 17
Figure 5: BacNa$_v$ channels possess a cytoplasmatic temperature sensitive domain. 19
Figure 6: Structure and possible engineering of viral potassium channel Kcv. 20
Figure 7: Effect of N or C-terminus EGFP addition to Kcv$_{NTS}$. 30
Figure 8: Strategies of Na$_v$Ae1 addition to the C-terminal domain of Kcv$_{NTS}$. 32
Figure 9: CTD addition to EGFP:KcvNTS has different effect depending on how much of the original sequence is maintained. 33
Figure 10: Membrane localization of different Kcv constructs demonstrate that they all localize at plasma membrane. 35
Figure 11: v1 is a temperature activated channel that opens efficiently at 50°C. 37
Figure 12: Single point mutations are sufficient to decrease the activation temperature of v1. 39
Figure 13: Effect of the combination of three different single points mutations of the coiled-coil region of CTD. 41
Figure 14: TICK1 trafficking is lower than mHCN2. 43
Figure 15: Activation and deactivation kinetic analysis of TICK1 made in gap-free on the same cell. 45
Figure 16: TICK1 activation reach saturation after 40 seconds at 40°C. 46
Figure 17: Deactivation kinetic of TICK1 is highly variable. 48
Figure 18: Characterization of expression pattern and dimension of the chimeric EGFP-Ferritin fusion. 50
Figure 19: Iron content and magnetic properties of EGFP-mFT. 53
Figure 20: Purification and native protein gel of EGFP-mFT. 55
Figure 21: EGFP-mFT iron quantification by ICP-OES reveals that are present 583 iron atoms for each ferritin. 57
Figure 22: Characterization of a modified version of gTEMP. 59
Figure 23: Design, localization and temperature sensitivity of "Magnetic KCV" (MagKCV). 62
Figure 24: Activation of MagKCV through a moving permanent magnet. 64
Figure 25: Cells expressing MagKCV subjected to MF shows higher percentage of channel activation. 66

Introduction

Optogenetics: controlling neuronal activity with light gated ion channels

The pre-eminent goal of neuroscience is to dissect the complexity of nervous system and understand how this works from the molecular level up to the behavioral readout. The action potential is one of the basic mechanisms that control the transmission of signal along the nervous system and the generation of action potential is called firing. To elicit an action potential (Figure *1*A), the membrane potential of the cell must exceed a threshold value. During the action potential, sodium voltage gated channels are responsible for the depolarization phase while potassium voltage gated channels contribute to the repolarization. For neuroscientist, the ability to remotely control the firing of specific neurons in the context of a complex neurons network is essential to correlate the neuronal activity with the behavior. Thus, tools enabling the remote activation or inactivation of firing in precise neuron populations are extremely important in neuroscience. In the last years, one of the greatest revolution in neuroscience was the development of optogenetic, which combine genetic and optic methods to make specific neuron populations express light controllable ion channels (Fenno et al., 2011). These channels, which are called optogenetic tools, can be either found in nature, like bacterial opsin, or synthetic channel created ad hoc in laboratory. When a specific light wavelength is absorbed by the channel, this change its conformation leading to the passage of ion for which is selective (Figure 1B). When this occurs in a neuron expressing an optogenetic tool, the light-controlled gating of the channel can alter the firing rate of that neuron (Figure 1C); optogenetic tools are considered excitatory when they increase or promote firing, while are considered inhibitory tools when they prevent, block or reduce firing rate. Channlerhodopsin-2 (ChR2) was the first bacterial opsin expressed in neurons and used to precisely control firing activity (Boyden et al., 2005). ChR2 is a seven transmembrane domain opsin isolated from the green alga *Chlamydomonas reinhardtii*. This is a non-specific cation channel that contains an all-trans-retinal chromophore that undergoes isomerization after 470nm blue light absorption and this causes a conformational change in the whole protein leading to the opening of ChR2 pore (Radu et al., 2009). The opening of ChR2 pore promotes a cation influx that depolarize cell's membrane promoting neuronal firing (Boyden et al., 2005). ChR2 was used also *in vivo* for instance to restores visual responses in mice with photoreceptor degeneration (Bi et al., 2006) or for mapping neural circuits (Arenkiel et al., 2007).

A particular chronic pain disease, called neuropathic pain, is caused by lesion of somatosensory nerves which leads to an extreme firing rate that causes the permanent pain sensation (Colloca et al., 2017). Inhibitory tools could be of particular interest, in perspective, as therapeutic agent for this class of pathologies. The first optogenetic inhibitory tools that were used to inhibit neuron firing were based on chloride channels, that rely on the negative electrochemical equilibrium of chloride ions to hyperpolarize the membrane potential thus preventing neuronal firing (F. Zhang et al., 2007), or on outward proton pump that moves H^+ out of the cells promoting again an inhibitory effect on neuronal activity (Chow et al., 2010). The use of chloride channel has the limitation that immature neurons use chloride as excitatory ion instead of inhibitory (Ben-Ari, 2002; Watanabe & Fukuda, 2015), and this conditions is maintained also in adult Dorsal Root Ganglion (DRG) neurons

(Nogueron, 1988), in primary sensory neurons of trigeminal ganglia (Schöbel et al., 2012), in olfactory sensory neurons (Kaneko et al., 2004) and can be even associated with neuropathic pain (J. T. C. Chen et al., 2014). On the other hand, the use of proton pump in neurons lead to a pH shift that activates calcium influx leading to spontaneous vesicle release in synaptic terminal leading (Mahn et al., 2016). For these reasons, a K^+ based optogenetic tool would be preferable. In contrast to the above-mentioned nature occurring light-gated channels, up to date no light controlled K^+ channels have been found in nature. To create K^+ inhibitory optogenetic tools different synthetic biology strategies were adopted, with the aim to combine a light sensitive domain to a K^+ channel. Several attempts were made (Banghart et al., 2004; D. L. Fortin et al., 2011; Janovjak et al., 2010; Kang et al., 2013), but the first fully genetically encoded K^+ light gated channel developed was BLINK1 (Cosentino et al., 2015), in which a viral potassium channel was coupled to a blue light sensitive domain. BLINK1 was tested in vivo in zebrafish, where it was inhibiting the touch response of three days old embryos exposed to 455nm blue light. This channel was later improved in BLINK2 (Alberio et al., 2018), with the addition of a C-terminal trafficking sequence to enhance its membrane expression. BLINK2 was shown to inhibit firing in brain slices and to reduce chronic neuropathic pain in a rat model.

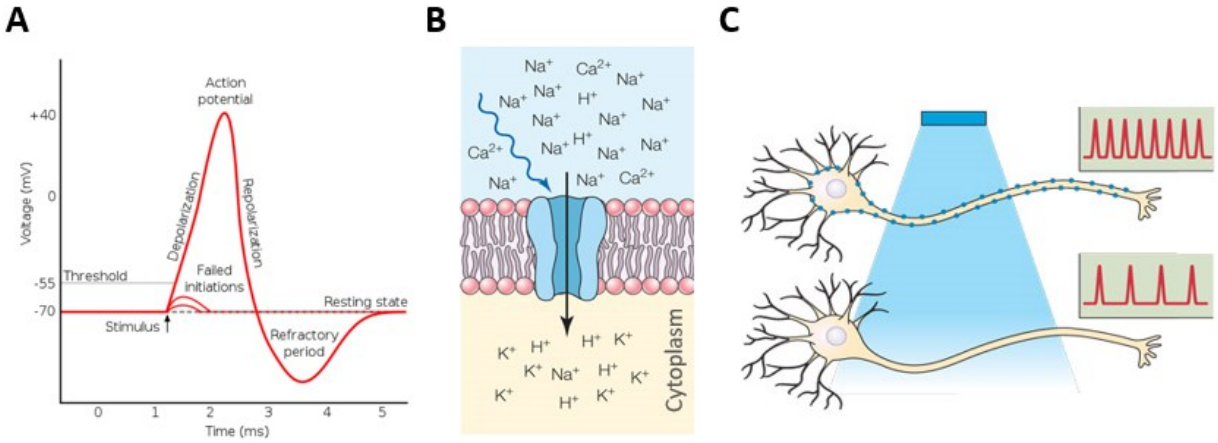

Figure 1: Controlling neuronal excitability with optogenetic tools.

A) *Scheme of a typical action potential. When a stimulus depolarizes the membrane potential above the voltage threshold, the action potential is evoked. During the depolarizing phase, the voltage gated sodium channel moves Na inside the cells, while during repolarization the voltage gated potassium channels drive K^+ efflux.* ***B)*** *Cartoon representation of a blue light gated ion channel (in this case cation aspecific) expressed in the plasma membrane. Upon absorption of light the ion channel opens and translocates different ions across the membrane according to their electro-chemical gradient.* ***C)*** *When a neuron expresses an optogenetic tool, its firing activity can be regulated by appropriate light. Optogenetic tool can be either excitatory (i.e. depolarizing, they promote neuronal firing) or inhibitory (i.e. hyperpolarizing, they prevent or block firing).*

Optogenetic tools are fully genetically encoded and are generally expressed in the neuronal population of interest by means of adeno associated viruses (AAV); they are usually fast (in the range of seconds or milliseconds) enabling high temporal resolution; they can be remotely activated using an external source of light. Regarding the latter point, even if is true that optogenetic tools can be

controlled by external light, its penetration into tissues is very low. For this, optogenetics requires the invasive implantation of fiber optics and, in many cases, of quite powerful light sources. Therefore, the application of optogenetic as therapeutic tool in humans, is greatly hampered and only recently the first example of optogenetic-based therapy in human has been published (Sahel et al., 2021).

Magneto-genetics: a promising alternative to optogenetics

To overcome the limits of optogenetics, scientists are searching for stimuli with a better tissue penetration than light and that can be considered safe. A good alternative is represented by magnetic fields that freely penetrate the tissues and are routinely used in medicine, as a diagnostic tool (MRI). Therefore, the search is on for a magnetic field-controlled ion channel. There are two possible scenarios: to search for a naturally occurring channel gated by magnetic fields, or to a synthetic protein composed by a magnetic receptor coupled to an ion channel. Unlike the naturally occurring light gated ion channels, there are no channels up to now known to be magnetic field activated and in general the understanding of how the animals sense the magnetic field, like in bird migrations in which earth magnetic field act as a compass, at the molecular level is still not clear (Qin et al., 2016). Thus, the synthetic pathway seems to be the most feasible approach for now.

The first attempts to create a magneto-genetic tool have exploited the magnetic properties of iron oxide nanoparticles. In fact, iron nanoparticles can be efficiently heated by electromagnetic waves with the appropriate frequency (J. P. Fortin et al., 2008). The heat generated can be used to trigger the opening of a temperature sensitive channel (Figure 2A). Several groups used this method to activate TRPV1 by means of external electromagnetic waves (R. Chen et al., 2015; Huang et al., 2010; Stanley et al., 2012). TRPV are cation channels, with a mild selectivity for divalent ions like Ca^{2+} and Mg^{2+}, that belongs to the family of TRP channel (Transient Receptor Potential) and are involved in sensing of chemical and physical stimuli in peripheral nociceptor terminals but are also part of inflammatory pathway (Patapoutian et al., 2003). To accomplish so many different functions, this class of channel is sensitive to several stimuli, like chemicals (capsaicin for instance is a strong activator of TRPV1), mechanical stimuli or heating. TRPV1 activates at temperature >42°C (Grandl et al., 2010) and this make it a suitable candidate to be activate through the heating of magnetic nanoparticles.

This was a very important first step leading to what is now called magneto-genetics. The next step was to create a fully genetically encoded tool, by substituting the exogenous iron nanoparticles with a protein with similar magnetic properties, ferritin. Ferritin is an iron storage protein found in the cytosol of bacteria, archaea and eukaryotes (Arosio et al., 2015). It is assembled by 24 subunits that form a spherical shell of about 12nm with an inner cavity of about 8nm that can store up to 4500 iron atoms. Mammalian ferritin are composed by light and heavy chains that assemble in a 24-mer with variable ratio in different tissues and organs; bacterial ferritin is composed by heavy chains only. Light chains have a structural role, promoting the folding of the complete structure, while heavy chains provide the catalytic activity necessary to oxidize Fe^{2+} in Fe^{3+} and to accumulate it inside the cavity (Arosio et al., 2017).

The possibility to use ferritin instead of iron nanoparticles to remotely activates TRPV1 was first demonstrated in 2015 (Stanley et al., 2015). In this work, three different conditions were tested in which the main difference is the distance between TRPV1 and ferritin. The ferritin used is composed by the joining of mouse ferritin light and heavy chain by a flexible linker, which was demonstrated to store iron more efficiently than ferritin in which the stoichiometry between the two chains is not 1:1 fixed (Iordanova et al., 2010). In the first case, TRPV1 and ferritin were simply co-expressed in HEK cells, resulting in the membrane expression of the channel and the cytosolic expression of the ferritin. In the second case, ferritin was fused to a myristoylation sequence to ensure ferritin membrane localization. In the third case, TRPV1 was engineered with an N-terminal EGFP nanobody (Kirchhofer et al., 2010) and this was co-expressed with EGFP-ferritin fusion, to ensure a direct interaction between the two (Figure 2B). Nanobodies are miniaturized versions of normal nanobodies which are generated by the isolation of the variable region of camelid single chain antibodies and bind their partners with very high affinity (Wesolowski et al., 2009). Together with the expression of TRPV1 and ferritin, a synthetic calcium response reporter gene was used to increase the production of insulin in response to calcium influx. HEK293T cells expressing one of the three TRPV1/ferritin expression system, together with the insulin reporter, were exposed to an oscillating magnetic field produced by a 465kHz radiofrequency (RF) generated through alternate current (AC) driven to a 2-turn solenoid coil surrounding the petri dish. The magnetic field strength can be tuned by varying the AC intensity and the produced field was of 29-32mT. A significative calcium influx, measured by calcium imaging, and insulin release increase were observed in all the three conditions, with the strongest effect when TRPV1 and ferritin are physically in contact through EGFP/nanobody interaction. The same system was applied in neurons to control firing rate or *in vivo* to control the level of blood glucose in mice (Stanley et al., 2016). For electrophysiology experiment, a permanent magnet was placed within the sample for 5 seconds, since the use of RF generates electrical artifacts in the measurement that did not allowed a precise recording (Stanley et al., 2016).

With a similar concept, TRPV4 was engineered with an N-terminal human ferritin dimer of light and heavy chain creating a synthetic TRPV4 called “Magneto2.0” (Wheeler et al., 2016). In this case the correct folding of ferritin is assured by the interaction between the ferritin fused to the TRPV4 and the endogenous ferritins produced by the expression system. Magneto2.0 was first tested in HEK cells which were subjected to an oscillating 50mT magnetic field produced by an electromagnet (3-6 pulses of 10 seconds each). A significative increase of intracellular calcium concentration was observed only in cells expressing Magneto2.0 exposed to the magnetic field. Magneto2.0 was also expressed in mouse brain slices, were the application of 50mT magnetic field through a permanent magnet elicit neurons firing; this effect was abolished in presence of a TRPV4 specific inhibitor. The permanent magnet was slowly moved to neurons generating a magnetic field gradient until 50mT were reached and neurons were exposed to period magnetic field stimulations. As *in vivo* proof of Magneto2.0 action, a real-time place preference test was done on mice expressing Magneto2.0 via AAV1 injection. Mice were placed in a chamber divided in two arms: a magnetized arm, lined with eight permanent magnets creating a magnetic field gradient of 50-250mT, and a non-magnetized arm. Only mice expressing Magneto2.0 shown a preference for the magnetized arm, while wild type mice have no preferences.

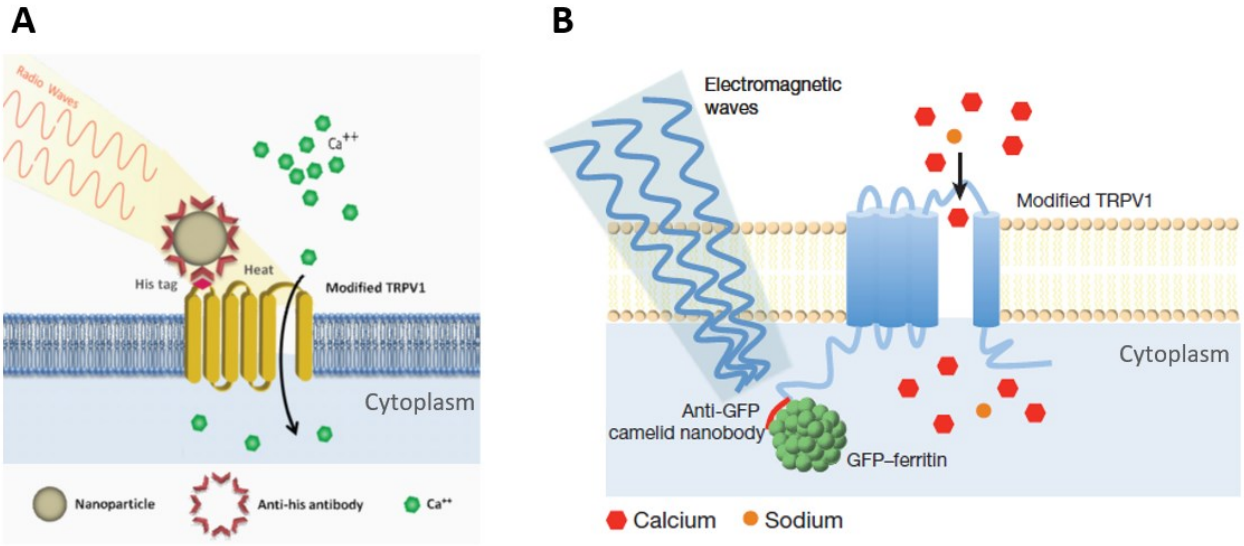

Figure 2: Development and evolution of magneto-genetic tools.

A) *Scheme of the first prototype of a magneto-genetic tool. TRPV1 was modified to interact with a magnetic iron nanoparticle on the extracellular side. In particular, a histidine tag was inserted in an extracellular loop of TRPV1 while an anti-histidine antibody was used to coat the iron nanoparticle. Radio waves have been used to induce the opening of TRPV1 with the following entry of calcium. Image adapted from "Stanley, S. A., Gagner, J. E., Damanpour, S., Yoshida, M., Dordick, J. S., & Friedman, J. M. (2012). Radio-wave heating of iron oxide nanoparticles can regulate plasma glucose in mice. Science, 336(6081), 604–608. https://doi.org/10.1126/science.1216753". Reprinted with permission from AAAS.* ***B)*** *Evolution of the previous magneto-genetic tool to make it completely genetically encoded. Magnetic nanoparticles have been substituted with the iron storage protein ferritin. Interaction between ferritin and TRPV1 is achieved through GFP exposed on the ferritin and a GFP-nanobody on TRPV1 N-terminus. Again, radio frequency application activates the channel with the following entry of* Ca^{2+}*. Image adapted from "Stanley, S. A., Kelly, L., Latcha, K. N., Schmidt, S. F., Yu, X., Nectow, A. R., Sauer, J., Dyke, J. P., Dordick, J. S., & Friedman, J. M. (2016). Bidirectional electromagnetic control of the hypothalamus regulates feeding and metabolism. Nature, 531(7596), 647–650. https://doi.org/10.1038/nature17183" and reprinted with permission.*

Are magneto-genetic tools acting through a temperature-regulated mechanism?

The mechanism of activation of ferritin-coupled TRPV- channels generated a great debate in the field which is still ongoing (Nimpf & Keays, 2017). Two main hypotheses have been proposed: i) ferritins activate the temperature sensitive TRPV by a thermal effect, similar to what occurs in the case of iron oxide nanoparticles; ii) ferritins activate the mechano-sensitive TRPV channels by mechanical forces. Both stimuli, increase in temperature and/or mechanical, could in principle be generated by the interaction of ferritins with the exogenous magnetic fields. At the same time, a first theoretical work that has analyzed this two possible pathways, concluded that both the mechanical forces or the increase in temperature generated by the ferritins are 5 to 10 fold lower than minimum values necessary to open TRPV channels (Meister, 2016). Recently, another study of the physic behind the magneto-genetic tools, came to completely different conclusions by using a different description of how the iron core forms cluster inside the ferritin. According to this approach, either mechanic and thermal pathways are possible (Barbic, 2019). With the aim to clarify

the real mechanism behind magneto-genetic, another group (Duret et al., 2019) used an experimental approach to test the activation of the magneto-genetic tool “Magneto 2.0” (Figure *3*A). In their paper, Duret and colleagues try to discriminate between the mechanical and heating pathway by impairing either the mechanical sensitivity of TRPV4 (-Mech) by pBPB, a phospholipase A2 (PLA2) inhibitor, or its temperature sensitivity (-Therm) by introducing two point mutations (Duret et al., 2019). HEK cells expressing wt Magneto2.0 or its -Mech or -Therm versions were exposed to a 275mT magnetic field generated by a permanent magnet moved at 0.08Hz. Only the temperature-sensitive version of the channel maintained a magnetic activation similar to the wt channel, while the mechano-sensitive channel did not. This is shown by the increase in calcium in cells transfected with either the wt or the two above mentioned versions of Magneto 2.0 (Figure *3*B). With the same approach, the application of a sham magnet, identical in size, weight and coating but with no magnetic moment, or a constant magnet did not elicit any calcium influx (Figure 3B). To explain this result the author refers to the magnetocaloric effect, which describes the relationship between magnetic entropy and temperature changes of a magnetic material exposed to a magnetic field (Franco et al., 2012). The magnetocaloric effect is represented in a schematic way in Figure *3*C: the iron inside the ferritin has a magnetic moment that is randomly orientated in the absence of a magnetic field. When a magnetic field is applied, the magnetic moments of iron atoms align with field reducing the magnetic entropy of the system. The decrease in entropy generates heat, which is absorbed by the TRPV4 triggering its opening. The authors estimated the heat generated by the ferritin in the condition they have tested, concluding that it is enough to activate TRPV4 or at least a fraction of the channel expressed by the cell. It is interesting to notice that the Magneto2.0 activation occurs only in presence of a moving magnet, while the static magnetic field produced by a constant permanent magnet does not affect calcium influx. The authors state that this is expected for the magnetocaloric effect, which relies on the magnetization process described in Figure 3C. The need of a non-static magnetic field was manifested also by the creator of Magneto2.0 in a paper in which he replied to different works that reported the impossibility to use Magneto2.0 to activate neuronal firing (Wheeler et al., 2019). This suggests that, even though the precise biophysical explanation of this phenomenon is still lacking (Meister, 2016), temperature is the mechanism through which TRPV4-based magneto-genetic tools seem to operate and this occurs only in the presence of an oscillating magnetic field.

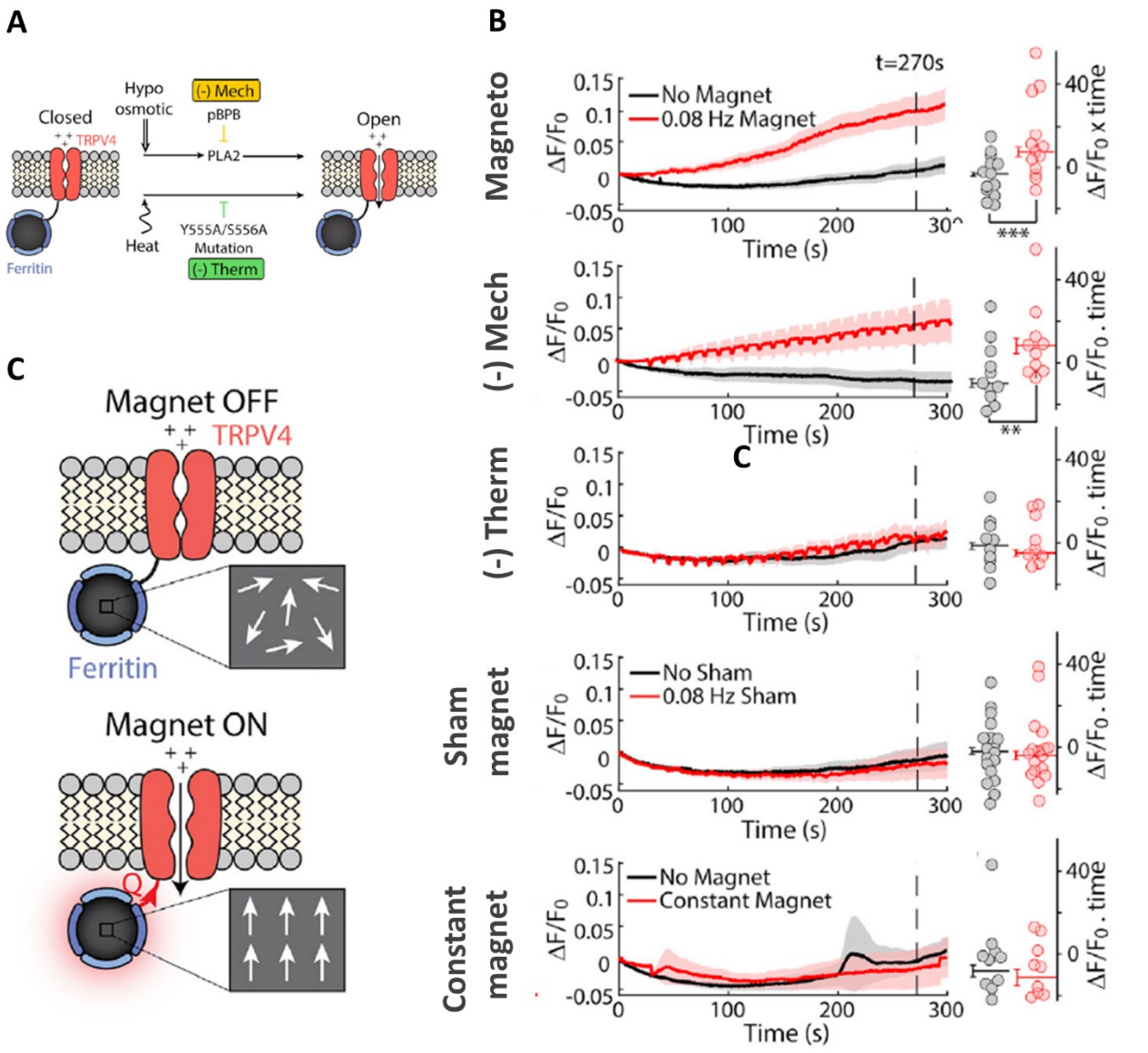

Figure 3: Experimental analysis of "Magneto2.0" demonstrate the temperature activation pathway.

A) *Cartoon scheme of the magneto-genetic tool "Magneto2.0", composed by TRPV4 fused at its N-terminus to ferritin. To understand the mechanism responsible of Magneto2.0 activation under magnetic field stimulation, a chemical inhibitor of mechano-sensitivity (condition -Mech) or two points mutation that makes TRPV4 temperature insensitive (condition -Therm) have been tested.* ***B)*** *A permanent magnet at 0.08Hz was applied on HEK293 cells expressing Magneto wt, -Mech, -Therm, sham magnet of constant magnet. No magnet was used as control in all the experiments. Calcium imaging was performed for 300s in the absence or presence of magnet for all conditions and changes in fluorescence were evaluated either during time (left panel) or after 270s (right panel). Only the -Mech construct still maintain the same magnetic effect of the wt construct, indicating that temperature is the mechanism of magnetic activation of Magneto2.0. Moreover, the application of a constant magnet has no effect on Magneto2.0.* ***C)*** *Magnetocaloric effect describes that the application of a magnetic field aligns the magnetic moment of iron inside ferritin, reducing magnetic entropy. The decrease in entropy produces heat (Q), which is transferred to TRPV4 inducing its opening. Images adapted from "Duret, G., Polali, S., Anderson, E. D., Bell, A. M., Tzouanas, C. N., Avants, B. W., & Robinson, J. T. (2019). Magnetic Entropy as a*

Proposed Gating Mechanism for Magnetogenetic Ion Channels. Biophysical Journal, 116(3), 454–468. https://doi.org/10.1016/j.bpj.2019.01.003" and reprinted with permission.

In the case of TRPV1 too, there are some evidences that temperature is the key factor underlying the magneto-genetic mechanism. As mentioned above, in the pioneering work of 2015, Stanley and colleagues tested several ways to associate the ferritin to the TRPV1 channel. When ferritin was tethered directly to the TRPV1 channels through the EGFP/nanobody, the magnetic effect was highest. However a significant increase of insulin release was observed even when the ferritin remained cytoplasmatic or when it was targeted to the plasma membrane through a myristoyl sequence (Stanley et al., 2015). This cannot happen if the ferritin dependent TRPV1 activation relies on a mechanical stimulation, while it is coherent with a temperature activation, where the heat transfer is more efficient when ferritin is in contact with TRPV1, as mentioned by the authors in the paper's discussion.

The final case is TRPV^{FeRIC} (Fe^{3+} redistribution to ion channels), a magnetogenetic tool created by (Hutson et al., 2017), exploiting a ferritin binding domain isolated from kininogen-1. They have used this tool to demonstrate that birth defects are associated with TRPV1 and 4 activations in neural crest cells of embryos during crucial phase of heart and face development. TRPV1^{FeRIC} and TRPV4^{FeRIC} have been expressed in HEK cells, where they interact with endogenous ferritin, and were remotely activated by radiofrequency (175MHz producing a 36μT magnetic field). Endogenous ferritins are needed for channel activation. TRPV^{FeRIC} channels expressed in HEK293T cells knockout for heavy chain ferritin gene (FTH1) do not respond to RF, but the response can be rescued by transfecting a plasmid carrying the FTH1 gene. In addition, when temperature dependence of TRPV1^{FeRIC} is abolished, by the insertion of three points mutations, RF does not give any effect, even if the channel is still responsive to its natural activator capsaicin. The same group published another paper in 2020, in which they further analyze TRPV^{FeRIC} mechanism of action and discover a major role of ROS (Hernández-Morales et al., 2020). They have described a mechanism in which an efflux of iron from ferritin iron core occurs during RF treatment, the free iron generates ROS (oxygen reactive species) that induce lipid oxidations that in turn activates the channel. Oxidized lipid, like arachidonic acid, are known TRPV agonist (Taberner et al., 2015). They have also tried to replicate the experiment of 2017 paper, introducing point mutations that abolish temperature dependence this time in TRPV4^{FeRIC} instead of TRPV1^{FeRIC}. In the case of TRPV4^{FeRIC}, the RF dependent activation was still present in the mutant and was not statistically different from the wt channel. Nevertheless, the author did not comment on the different results obtained with TRPV4^{FeRIC} and TRPV1^{FeRIC}, simply stating *"while the oxidation mechanism does not require direct temperature activation of the channels, the mechanism does not exclude the possibility of localized heating or synergy of lipid oxidation and heating mechanisms"*. The discovery that ROS could be related to activation of magneto-genetic tool have inspired the research of another group, that have shown how ROS production during RF treatment of HEK293 expressing the TRPV1/ferritin construct from Stanley et al., 2016 contributes to channel opening (Brier et al., 2020). The authors also measured the minimum magnetic field strength necessary to activate the tool, showing that an effect was observed with at least 23.4mT, while the frequency of RF has a smaller impact since all the tested

frequency (ranging from 354 to 501kHz) were activating the channel. In these last papers ROS are emerging as a possible player in magneto-genetic tools activation, however it is not clear if this mechanism of action prevails over the temperature activation or if the two mechanisms work together.

How to evaluate mechanical and thermal effects of magnetic fields on ferritins?

The work of (Duret et al., 2019) experimentally demonstrated the mechanism behind the magneto-genetic tools. However, direct measurements of mechanical forces or temperature changes generated by the ferritin in response to magnetic field are still lacking. In this chapter I will introduce two experimental approaches that we have identified for testing possible mechanical or thermal effect of MF on ferritins.

Mechanical effect:

HEK cells expressing iron over-loaded ferritin can be physically attracted from a permanent magnet generating a static magnetic field of around 600mT (Kim et al., 2012). This system was used to separate cells basing on their ferritin expression (Kim et al., 2012). At the intracellular level, a possible way to evaluate if ferritins respond to magnetic fields could be Fluorescent Correlation Spectroscopy.

Fluorescent Correlation Spectroscopy is a widely used technique to accurately measure local concentration, hydrodynamic radius, protein interaction and also diffusion coefficient (Yu et al., 2021). With this method, it should be possible to measure the diffusion coefficient of GFP-ferritins and evaluate if it is influenced by a static magnetic field. In a typical FSC experiment, a fluorescent molecule solution is observed by a confocal microscope (Figure 4A, top image); in the observation volume the molecules freely diffuse generating fluctuations in the recorded fluorescent intensity (Figure 4A, middle image). The amplitude of the fluctuation is related to the number of molecules present in the observation volume, while the duration is related to the time that the molecules spend in the observation volume. Big particles move slowly and thus spend more time in the observation volume and vice-versa for small particles. A mathematical analysis is performed to obtain the autocorrelation curve, in function of sampling lag time τ, which describes signal persistence in the observation volume. This curve is fitted with a function modeling diffusion as unique cause of fluorescence intensity fluctuations (Figure 4A, bottom image). The fitting allows the calculation of τ_D, the average time that the molecule needs to cross the whole observation volume. τ_D is clearly related to the diffusion coefficient of the molecule, which is inversely proportional to the hydrodynamic radius (stokes law). Among the different methodology using FCS principle, we decided to use Raster Image Correlation Spectroscopy (RICS). This method uses sequential acquisition of images by a scanning confocal microscope and a mathematical bidimensional analysis to obtain, through fitting, the diffusion coefficient (Rossow et al., 2010). RICS advantage consist in the autocalibration of the method: compared to single point FCS, which needs a preventive observation calibration volume, in RICS the observation volume became a parameter of fitting function and thus determined together with diffusion coefficient. Our idea is to use this technique on a solution containing EGFP labelled ferritin and to analyze its diffusion in presence or absence of

static magnetic fields. If the magnetic field generates ferritin movement, as theoretically postulated (Meister, 2016) or experimentally demonstrated (Kim et al., 2012), the diffusion coefficient should be affected.

Thermal effect:

Genetically encoded thermometer, called gTEMP, are fluorescent proteins that can measure local changes in temperature directly inside cells or living organisms (Nakano et al., 2017). gTEMP were used to measure temperature difference in cytoplasm and nucleus of the same cell or thermogenesis produced by mitochondrial activity (Nakano et al., 2017). Among many fluorescent proteins analyzed (Figure 4B, top image), mT-Sapphire was the one with less temperature sensitivity, while Sirius decreased its fluorescence of 60% passing from 20 to 50°C. To build a ratiometric sensor, mT-Sapphire and Sirius were expressed in 1:1 ratio in mammalian cells and the ratio between 509nm (due to mT-Sapphire) and 425nm (due to Sirius) fluorescent intensity was calculated at different temperatures (Figure 4A, bottom image). This ratio increases its values at increasing temperature, enabling a precise measurement of temperature changes. We have used this system to evaluate the temperature changes produced by ferritin during the magnetic field application (see Results).

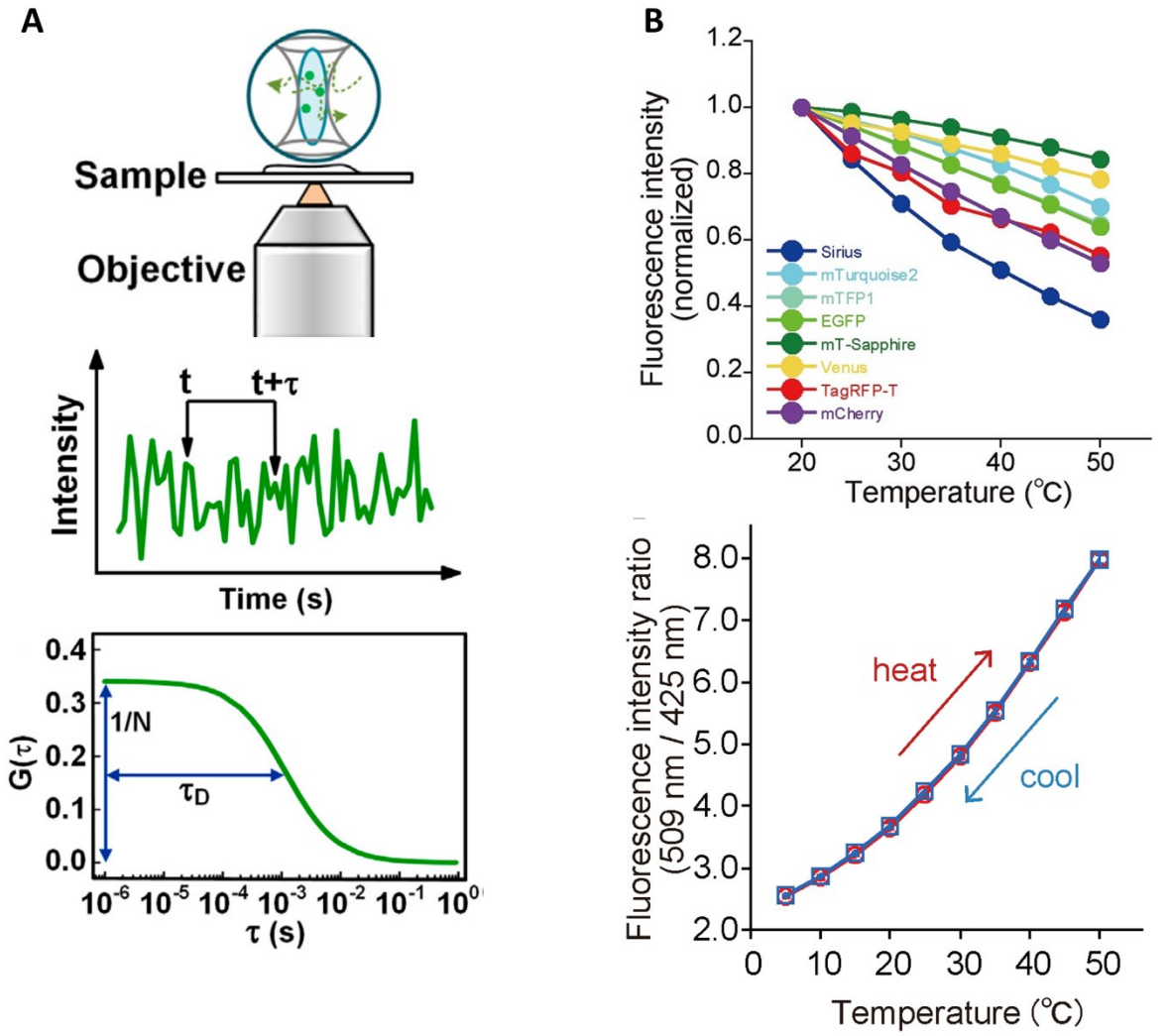

Figure 4: Fluorescence Correlation Spectroscopy and temperature-sensitive fluorescent proteins can be used to evaluate the ferritin magnetic properties.

A) *Principle of Fluorescent Correlation Spectroscopy technique (FCS). The sample contains a fluorescent molecule in solution that is imaged by a confocal microscope. The diffusion of the molecules in and out from the observation volume (blue circle) produces fluctuations in the fluorescence intensity over time (middle graph). Trough an auto-correlation function is possible to derive the characteristic* τ_D *of the molecule that corresponds to the average time that the molecules need to cross the observation volume. This is correlated with the size of the molecule since bigger particles will move slower while smaller particles will be faster. Images adapted from "Yu, L., Lei, Y., Ma, Y., Liu, M., Zheng, J., Dan, D., & Gao, P. (2021). A Comprehensive Review of Fluorescence Correlation Spectroscopy. Frontiers in Physics, 9(April), 1–21. https://doi.org/10.3389/fphy.2021.644450" and reprinted with permission.* ***B)*** *Design of a genetically encoded fluorescent thermometer. In the upper image are reported the temperature sensitivity of fluorescent intensity of different fluorescent proteins. mT-Sapphire is the less temperature sensitive while Sirius fluorescence is greatly affected by temperature. These two proteins were expressed in mammalian cells in a 1:1 ratio. In the lower image is shown the changing in fluorescent intensity ratio of the two proteins at different temperatures. This ratio was used to measure the temperature directly inside cells. Images adapted from "Nakano, M., Arai, Y., Kotera, I., Okabe, K., Kamei, Y., & Nagai, T. (2017). Genetically encoded ratiometric fluorescent*

thermometer with wide range and rapid response. PLoS ONE, 12(2), 1–14. https://doi.org/10.1371/journal.pone.0172344" and reprinted with permission.

The need to build a temperature sensitive K^+ channel

To date, all the magneto-genetic tools available are based on ferritin coupled TRPV channels, which mainly conduct Na^+ and Ca^{2+}, limiting the range of application of these tools to depolarizing and/or intracellular calcium increase. To create a magneto-genetic inhibiting tool TRPV should be substitute with a K^+ channel and this must be temperature sensitive to be efficiently activated by the local rise of temperature induced by ferritin after magnetic field stimulation. The best scenario would be to have a channel whose opening relies only on the increase of temperature, to further demonstrate that temperature is the mechanism exploited in magneto-genetic tools. Indeed, part of the uncertainty surroundings magnetic activation of TRPV-based constructs, originated from the fact that these channels are poly-modal, are indeed activated by several stimuli (mechano, temperature, lipids and so on). In the case of K^+ channels too, temperature-dependent channels are also polymodal. For instance, the K2P channel TREK1, is dually responsive to temperature and mechanical forces (Honoré, 2007). In this work we therefore exploited the possibility to create a synthetic temperature gated K^+ channel by joining a temperature sensitive domain to a K^+ conducting pore. A temperature sensitive domain was recently identified and characterized in the voltage-gated bacterial sodium channels $BacNa_v$ (Arrigoni et al., 2016; Shaya et al., 2014) (Figure *5*A). This is a C-terminal cytoplasmatic domain (CTD) that undergoes a partial unfolding with temperature increase, and modifies the voltage dependent gating of the channel, as shown in Figure 5B (Arrigoni et al., 2016). The structure of this domain is an α-helix that is the continuation of the S6 transmembrane helix of the pore module of the channel. The CTD is composed by two main regions: the neck and the coiled coil. The neck is the region closer to the plasma membrane and is composed almost exclusively by hydrophilic residues while the coiled-coil domain comprises six hydrophobic residue layers (Figure 5C). Overall, the CTD of $BacNa_v$ act as a constrain for the pore region and the intensity of this constrain can be regulated unfolding the neck region by temperature. Is particularly interesting the comparison between the behavior of two different $BacNa_v$ channels: Na_vAe1 and Na_vSp1. The first, when expressed in HEK293 cells, does not give any measurable current when tested at room temperature with a voltage protocol from +80 to -40mV (Figure 5D, top left panel). On contrary, the second gives a measurable current using a protocol from +70 to -60mV (Figure 5D, bottom left panel). When the CTD of Na_vAe1 is deleted (Figure 5D, top middle panel) or substituted with the Na_vSp1 CTD (Figure 5D, top right panel), measurable currents are obtained. The properties of Na_vAe1 can be transferred to Na_vSp1 inverting the CTD of the two channels; in fact, Na_vSp1 in which CTD is substituted with the one Na_vAe1 does not give any measurable current (Figure 5D, bottom right panel). The membrane expression of all these constructs was confirmed by western blot, excluding a trafficking problem. The CTD from NavAe1 is able to maintain close the channel, at least at room temperature, and this property can be transferred to other channel of the same family. Na_vAe1 is the only $BacNa_v$ channel with this characteristic and thus its CTD is a promising candidate to be installed on an open K^+ channel to make it temperature sensitive.

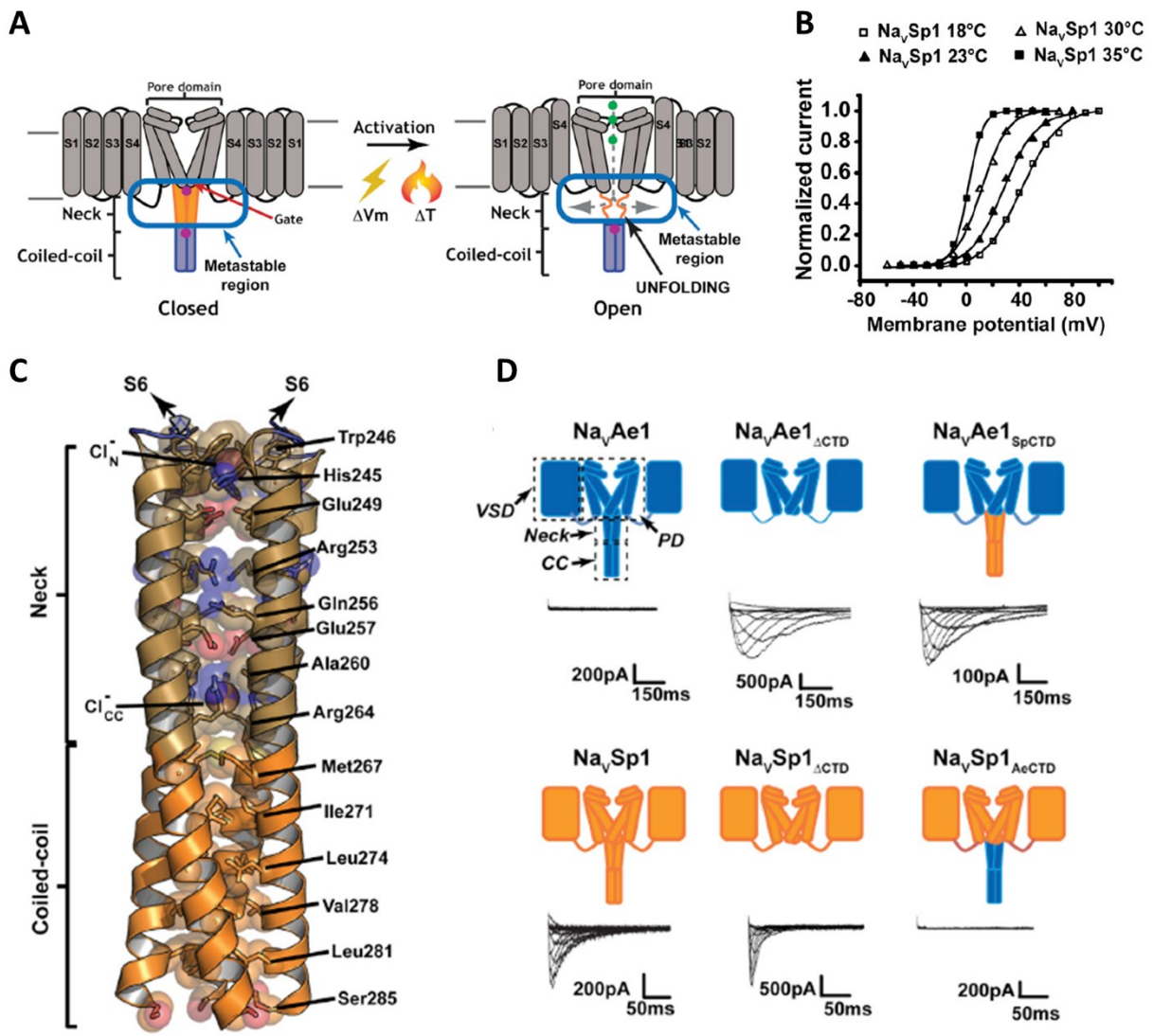

Figure 5: BacNa$_v$ channels possess a cytoplasmatic temperature sensitive domain.

A) *Cartoon of BacNav structure showing the voltage sensor domain (S1-S4), the pore domain (S5-S6) and the cytoplasmatic C-terminal domain (CTD) composed by the neck and the coiled coil. Voltage triggers the activation of the channel and temperature, trough the unfolding of the neck region, modulating the voltage dependence of the channel.* ***B)*** *Voltage dependence of Na$_v$Sp1 at various temperature. The same cell expressing Na$_v$Sp1 was tested with the same voltage step protocol at different temperature. When temperature increases, the $V_{1/2}$ of the channel is shifted to more negative potentials.* ***C)*** *Crystal structure of the CTD of Na$_v$Ae1. The neck, which is the domain closer to S6 helix, is composed by hydrophilic residues while the coiled coil is composed by layers of hydrophobic side chains. This difference is reflected in the role of the two domains: the neck is the metastable region that unfolds when temperature increase while the coiled coil is more compact and has a structural role.* ***D)*** *Comparison between Na$_v$Ae1 and Na$_v$Sp1 CTD properties. In the upper panel, in blue are shown the cartoon structures of Na$_v$Ae1 wild type, without the CTD (ΔCTD) or with Na$_v$Sp1 CTD (SpCTD). Under every cartoon are shown the corresponding currents recorded in HEK cells expressing the indicated construct. In the lower panel, in orange are shown the cartoon structures of Na$_v$Sp1 wild type, ΔCTD or with Na$_v$Ae1 CTD (AeCTD). Images adapted from "Arrigoni, C., Rohaim, A., Shaya, D., Findeisen, F., Stein, R. A., Nurva, S. R., Mishra, S., McHaourab, H. S., & Minor, D. L. (2016). Unfolding of a Temperature-Sensitive Domain Controls*

Voltage-Gated Channel Activation. Cell, 164(5), 922–936. https://doi.org/10.1016/j.cell.2016.02.001" and reprinted with permission.

Viral Potassium channels can be efficiently engineered with heterologous domains

To insert the CTD from $BacNa_v$ on a potassium channel is essential to find a feasible candidate for this purpose. The chosen channel should be not regulated by other stimulus (so that after the engineering process temperature will be the only gating mechanism), selective for K^+ and easy to handle and modify. Viral potassium channels (Kcv) fulfill all these requirements. Kcv are potassium channels that have been isolated from algae infecting viruses (called chloroviruses) and are the smallest and most primitive form of potassium channels (Gazzarrini et al., 2009; Plugge et al., 2000). Different Kcv channels were identified from several chloroviruses and, despite some structural and physiological differences, they all share the same architecture (Figure 6A). They are composed of only 2 transmembrane domains (TMD1 and TMD2), with short or even absent cytoplasmatic termini, and assemble in tetramers that traffic to the plasma membrane. They are selective for potassium thanks to the typical K^+ selectivity filter with the signature sequence TxTGY/FGD and are blocked by the known K^+ channel blocker $BaCl_2$ (Plugge et al., 2000). One of the most interesting features of this class of channels is the possibility to engineer them with the goal to confer new properties and gating mechanisms (Figure 6B). PBCV1-Kcv has been efficiently transformed in a blue light sensitive channel through the addition of the LOV domain from Phototropin-1 of *Avena sativa* (Cosentino et al., 2015), in a voltage gated K^+ channel by the addition of the VSD (Voltage Sensor Domain) from *Ciona intestinalis* (Arrigoni et al., 2013) and finally in an intracellular Ca^{2+} sensor exploiting the interaction between the calcium-binding protein Calmodulin and its interacting peptide M13 (DiFrancesco et al., 2015). Considering all these evidences, we decided to engineer Kcv with the cytosolic temperature domain from $BacNa_v$ to make it temperature sensitive and thus prone to be magnetically activated after the addition of ferritin.

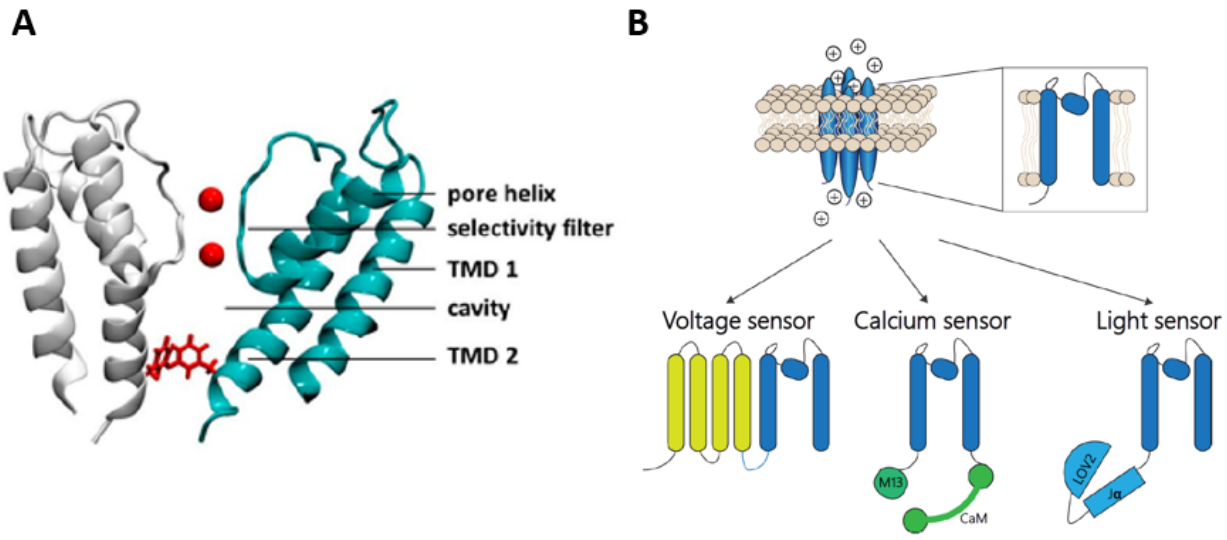

Figure 6: Structure and possible engineering of viral potassium channel Kcv.

A) *Structure of two opposing monomer subunit of Kcv_S from ATCV-1 virus derived from a molecular dynamics simulation. Are indicated the 2 transmembrane helices TMD1 and TMD2, the selectivity filter, the pore helix and the cavity. The two red spheres are K^+ ions while the side chain of F78 is explicated in red. This residue is responsible for the gating of the channel. Images adapted from "Rauh, O., Urban, M., Henkes, L. M., Winterstein, T., Greiner, T., Van Etten, J. L., Moroni, A., Kast, S. M., Thiel, G., & Schroeder, I. (2017). Identification of Intrahelical Bifurcated H-Bonds as a New Type of Gate in K+ Channels. Journal of the American Chemical Society, 139(22), 7494–7503. https://doi.org/10.1021/jacs.7b01158" and reprinted with permission.* ***B)*** *Examples of engineering of Kcv. In the upper panel on the left is shown the tetramer of KCV inserted in the plasma membrane while on the right inset only one monomer is present. In the lower panel are shown three different examples of Kcv modifications. From left to right: addition of Ciona intestinalis voltage sensor domain, addition of Calmodulin and its partner M13 and addition of Avena sativa LOV domain. All these modifications make Kcv respectively a voltage gated K^+ channel, an intracellular Ca^{2+} sensor and a blue light activated K^+ channel.*

Aim of the thesis

The goal of this thesis work is to create the first magneto-genetic tool based on a potassium channel. To date, all the magneto-genetic tools described in literature are based on TRPV channel coupled to the iron storage protein ferritin (Hutson et al., 2017; Stanley et al., 2016; Wheeler et al., 2016). When a magnetic field is applied, the ferritin magnetic core respond to the magnetic field locally increasing the temperature and this activates TRPV channel, that is temperature sensitive (Duret et al., 2019). The great advantage of magneto-genetic over optogenetic tools, is the very high tissue penetration of electro-magnetic radiation compared to light. This overcome the need of fiber optic implantation or the usage of high-intensity light that can damage the animal when optogenetic tools are used for *in vivo* experiments. Moreover, the widespread use of MRI in diagnostic demonstrates that magnetic field are considered safe even for human applications. To achieve this result, the first step is the creation of a K^+ channel controlled by temperature. We will join a viral potassium channel (Kcv) with a cytosolic temperature sensitive domain found in bacterial sodium channels (Arrigoni et al., 2016). The temperature-sensitive Kcv will be then tethered to ferritin using the same rational of TRPV based magneto-genetic tools. The functionality of all these constructs will be tested by electrophysiology, while localization and ferritin-Kcv interaction will be analyzed by fluorescent confocal microscopy. A K^+ magneto-genetic tool could find useful application for noninvasive neuronal inhibition, not only in neuroscience research but also in the future treatment of pathologies correlated with uncontrolled neuronal firing, such as neuropathic pain (Colloca et al., 2017). Moreover, another outcome of this study will be to confirm that the magnetic effect depends on ferritin-induced temperature increase.

Material and methods

Molecular biology

All the constructs present in Table1 were generated by Gibson cloning (Gibson et al., 2009). Briefly, the nucleotide sequence of interest was amplified by standard PCR using primers containing complementary sequence for the insertion region or for the adjacent fragment. PCR was performed using Phusion™ High-Fidelity DNA Polymerase (Thermo Scientific, product number #F530S) following manufacturer indications. Aliquots of PCR products were separated by electrophoretic agarose gel stained with SYBR™ Safe (Invitrogen, catalog number #S33102). If DNA bands were resembling the right molecular weight, controlled by comparison with 1Kb DNA ladder (Invitrogen, catalog number #10787018), the remaining PCR product was purified using Expin™ Combo GP kit (GeneAll, catalog number #GA-112-150) and DNA concentration was measured by Spectrophotometer (Biospectrophotometer ®, Eppendorf). The vector backbone was prepared by restriction enzymes digestion. For Gibson assembly, 100 ng of linearized vector was mixed with 1:3 molar ratio of each insert and incubated in a 15uL master mix containing T5 Exonuclease (New England BioLabs, catalog number #M0663S), Phusion polymerase (New England BioLabs, catalog number #M0530S), and Taq DNA Ligase (New England BioLabs, catalog number #M0208S). Master mix was prepared as described in (Gibson et al., 2009). Total volume reaction of 20uL was reached by adding H_20 and then reaction mix was incubated at 50°C for 1 hour. 5uL of the reaction were transformed in 50uL STBL2 or DH5alfa *E. coli* strain following standard transformation protocol. To verify the insertion of all the inserts in the vector backbone, Colony-PCR was performed on the colonies obtained after transformation. The colonies positive at Colony-PCR were send for sequencing to assess nucleotide sequence correctness. For site directed mutagenesis QuikChange Lightning kit (Agilent, catalog number #210518) was used following manufacturer instructions.

Construct name	Vector backbone	Details
KcvNTS:EGFP	pEGFP N2	KcvNTS (1-82) :: EGFP
EGFP:KcvNTS	pcDNA	EGFP :: KcvNTS (1-82)
v1	pcDNA	EGFP :: Kcv_{NTS} (1-75) :: Na_vAe1 (231-288)
v2	pcDNA	EGFP :: Kcv_{NTS} (1-80) :: Na_vAe1 (235-288)
TICK1	pcDNA	EGFP :: Kcv_{NTS} (1-75) :: Na_vAe1 (231-288) M267A
EGFP-mFT	pcDNA	EGFP :: mFTL (1-183) :: mFTH (1-185)
EGFP-hFTH	pcDNA	EGFP :: hFTH1 (1-184)
gTEMP2	pcDNA	mCherry (1-236) :: T2A :: mT-Sapphire (1-240)
nanoTICK1	pcDNA	EGFP nanobody (1-114) :: tagRFP-T :: Kcv_{NTS} (1-75) :: Na_vAe1 (231-288) M267A
MagKCV	pcDNA	nanoTICK1 :: T2A :: EGFP-mFT

Table 1: *List of clones generated in this thesis*

KcvNTS:EGFP cloned in pEGFP N2 vector was kindly provided from Gerhard Thiel's lab (Technical University of Darmstadt, Darmstadt, Germany). NavAe1 gene was kindly provided from Dan Minor's lab (University of California, San Francisco, U.S.A.). EGFP nanobody and mouse ferritin genes were

cloned from the Addgene plasmid #79649, while human ferritin heavy chain gene was cloned from the Addgene plasmid #81879 (Addgene, Watertown, U.S.A.). All the other genes and backbone plasmids were already present in the lab.

DNAs used for transfection were prepared using the Exprep™ Plasmid SV kit (GeneAll, catalog number #GA-101-150) following manufacturer instructions.

Cell culture and transfection

HEK293T cells were cultured in Dulbecco's modified Eagle's medium (Euroclone) supplemented with 10% fetal bovine serum (Euroclone), 1% Pen Strep (100 U/mL of penicillin and 100 µg/ml of streptomycin) and stored in a 37°C humidified incubator with 5% CO2. Cells were periodically split using trypsin to avoid overgrowth. Cells were grown in 25mm^2 flasks and then transferred in 35mm petri dishes one day before transfection. For confocal imaging, cells were plated on 35mm glass petri dishes. Transfections were made on 70% confluent petri dishes using 1ug of DNA and 2uL of TurboFect Transfection Reagent (Thermo Scientific, catalog number #R0531) according to manufacturer protocol.

Confocal imaging

Images of HEK transfected cells were acquired 24 hours after transfection trough an Eclipse-Ti (Nikon) inverted confocal microscope interfaced with an A1 series of confocal laser point scanning system which allows for excitation at 405, 488, 561 and 640 nm. Petri dishes were observed with a 40x 1.2 NA water or 60x 1.4 NA oil immersion objective. The pinhole aperture was set to 1.0 Airy. The images were collected using low lasers excitation power and acquiring the emission range through bandpass filters by means of built-in GaAsP PMT detectors of the confocal microscope. Table 2 shows for each fluorescent molecule the used excitation laser end emission filter. 1uL of CellMask™ Deep Red Plasma membrane Stain (Invitrogen, catalog number#C10046) was used to stain plasma membrane of cells.

Fluorescent molecule	**Excitation laser**	**Emission filter**
EGFP	488nm	525/50
tagRFP-T	561nm	595/50
mCherry	561nm	595/50
mT-Sapphire	405nm	525/50
CellMask	640nm	700/70

Table 2: *Excitation laser and emission filter used in the confocal imaging experiments*

Electrophysiology

Currents were recorded in whole-cells configuration with a Axopatch 200B (Molecular Devices, San Jose, U.S.A.); data were digitized with an Axon Digidata 1550B (Molecular Devices, San Jose, U.S.A.) converter and analyzed off-line with Axon pClamp9. Patch pipettes were fabricated from 1.5mm

O.D. and 0.86 I.D. borosilicate glass capillaries (Sutter, Novato, CA, USA) with a P-97 Flaming/Brown Micropipette Puller (Sutter, Novato, CA, USA) and had resistances of 3–5MΩ.

The pipettes were filled with a solution containing: 10 mM NaCl, 130 mM KCl, 1 mM egtazic acid (EGTA), 0.5 mM MgCl2, 2 mM ATP (Mg salt) and 5 mM HEPES–KOH buffer (pH 7.4). The extracellular bath solution contained 100 mM KCl, 1.8 mM CaCl2, 1 mM MgCl2, 80 mM D-mannitol and 5 mM HEPES–NaOH buffer (pH 7.4). When extracellular solution with lower KCl molarity were used, D-mannitol was used to reach correct osmolarity. The standard voltage protocol used in this work is composed by a holding potential at -6mV (100ms), voltage steps from +80 to -120mV (20mV steps, 300ms) and a post pulse at -80mV (100ms). Holding potential was switched to -20mV in experiments with 40mM KCl extracellular solution, while voltage steps were extended to +60/-160mV in case of recordings on EGFP:Kcv_{NTS} or Kcv_{NTS}:EGFP constructs. A gap-free protocol at -60mV was also used.

Only cells in which a 1 GΩ seal or better was achieved were kept for analysis. Patch-clamp currents were acquired with a sampling rate of 5 KHz and lowpass filter of 0.5 kHz. Currents were normalized to cell capacitance. Neither series resistance compensation nor leak correction were applied.

Temperature experiments

To warm cells from 25°C to 50°C, QE-1 Quick Exchange Platform (Warner Instruments, catalog number#64-0375), powered by TC-324C Single channel Heater control (Warner Instruments, catalog number#64-2400), was used to heat the whole petri dish. Temperature was set on the heater control.

Experiments using warmed perfused solution were carried out using a device from Rein Dan Electronic, which was kindly provided from Dr. Paul Heppenstall (SISSA, Trieste, Italy). Temperature was set directly on the instrument itself. Cell temperature was controlled placing an IT-23 Ultra-Fast Flexible Implantable Microprobe (Physitemp) about 50-100um from the cell. Microprobe has a diameter of 0.2mm and a temperature resolution of 0.1°C. Microprobe was connected to BAT-12 Microprobe Thermometer (Physitemp) to read the temperature. Measured temperature was manually annotated during the recording.

Magnetic field stimulation

To perform magnetic stimulation a N55 grade cylindrical neodymium permanent magnet (1.5x6.35mm, axially magnetized, K&J Magnetics) was used. The permanent magnet was manually moved back and forth with a micromanipulator for 5 minutes at 1Hz. The magnetic field intensity was measured with a DC-Gaussmeter (GM-1-HS, AlphaLab Inc.). In the closest position magnetic field was around 50mT, while in the further position around 3mT. Particularly attention was made to not touch the extracellular solution of the petri, to avoid movement of the recording setup.

Cell membrane bursting

To isolate cells plasma membrane an optimized version of a previously published protocol was adopted (Bezrukov et al., 2009). Cells were seeded on poly-lysine treated glass petri dishes prior to

transfection. 24 hours after transfection CellMask was added to stain cell membrane. Confocal imaging was performed before bursting to control transfection efficiency. Afterwards, medium solution was removed, and the petri was vigorously washed 3-5 times with 2mL of ice cold ddH20. H20 was changed in every washing to remove any cellular debris. Membranes that remain attached to petri bottom were visualized by confocal imaging.

TICK1-HA immunofluorescence

24 hours post transfection HEK293T cells were washed twice with PBS and then incubated 30 minutes at 37°C with PBS + 2% BSA. After, cells were passed to PBS + 2% BSA + α-HA (Anti-HA (12CA5) from mouse IgG2bκ, Roche catalog number #11583816001, 2.5uL each sample) and incubated for 60 minutes at 37°C. After 1 washing with PBS + 2% BSA, cells were incubated with PBS + 2% BSA + Alexa633 α-mouse (Invitrogen, Catalog #A-21050, 2uL each sample) for 50 minutes at 37°C. Cells were then washed once with PBS + 2% BSA and twice with PBS. Cells fluorescence was followed by confocal microscope imaging.

Ferritin crude lysate and purification

HEK293F cells growing in suspension (37°C / 5% CO2 / 85RPM) in FreeStyle™ 293 Expression Medium (Gibco, catalog number #12338018) were transfected with EGFP-mFT and EGFP-hFTH. Transfection was made using PEI MAX® transfection reagent (Polysciences, catalog number # 24765) according to manufacturer instruction. 24 hours after transfection, cells were pelleted and then broken using low-salt buffer (10mM HEPES pH7.5, 10mM $MgCl_2$, 10mM KCl, 20ug/uL DNAse, 10ug/uL RNAse, 1:1000 Complete protease inhibitor (catalog number #11697498001**,** Roche) and 0.5mM PMSF). After cells breaks low salt buffer was brought to PBS (140mM NaCl, 10mM KCl, 10mM Na_2HPO_4, 1.8mM KH_2PO_4) adding the necessary salts. 0.5mM TCEP was also added. Samples were then centrifuged 40 minutes at 37000 RPM / 4°C. After centrifuge, the obtained supernatant is called crude lysate (containing all cells cytosolic proteins). Crude lysates were injected in a Superose 6 increase 5 150 GL HPLC connected to F-SEC. Samples fluorescence was evaluated with a detector set at 488nm for excitation and 509nm for emission.

If purification was necessary, the crude lysate was incubated under agitation with a nickel resin (Ni^{2+}-NTA resin, QIAGEN) overnight at 4°C. Nickel resin solution containing the sample of interest was loaded on a manual column and washed with 5 column volumes of PBS 1X + 50mM Imidazole. Column was eluted with 12 column volumes of PBS1X + 300mM Imidazole. Eluate was concentrated up to 400uL and injected in a Superose Increase 10300 HPLC equilibrated with PBS 1X. Protein profile was obtained following UV 280nm signal.

Protein native gel

Crude lysates or purified proteins were loaded on NativePAGE™ gel (Invitrogen, catalog number # BN1001BOX) after addition of homemade 6X Native loading dye (375mM TRIS-HCl pH6.8, 4.8% glycerol, 0.03% Bromophenol Blue) to a final 1X dilution. NativeMark™ protein standards mix (Invitrogen, catalog number # LC0725) was used to have molecular weights references. Gels were always made in double. One was stained with Comassie brilliant blue solution (Sigma Aldrich, ctalog

number #B0770). The other was subject to Prussian blue staining: a solution containing 2% $K_4Fe(II)(CN)_6$ + 2% HCl was added to the gel, the gel was then left for 1 hour in dark under agitation and then 4 washings with H_2O of 15 minutes each were performed. The chemical reaction that produce the Prussian blue staining is the following: $4FeCl_3 + 3K_4Fe(CN)_6 \rightarrow Fe_4[Fe(CN)_6]_3 + 12KCl$. $Fe_4[Fe(CN)_6]_3$ is the Prussian blue pigment. The addition of HCl increases the availability of iron during the reaction.

Dynamic Light Scattering (DLS)

DLS measurements were performed using a "Protein Solutions Dynapro" (Wyatt Technology, Santa Barbara, U.S.A.). Samples were first centrifuged at >13000RCF for 10 minutes to remove any precipitate and then analyzed using standard device protocol.

Purification and temperature dependence analysis of mT-Sapphire and mCherry

mT-Sapphire and mCherry were cloned in pRSET-B plasmid containing a 6xHistidine N-terminal tag. Both plasmids were transformed in Rosetta *E. coli* strain and grown in 500mL LB+50ug/mL Ampicillin at 37°C/280RPM. When OD_{600} has reached 0.5, 400uM IPTG was added to induce protein expression and then bacteria were grown overnight at 20°C/100RPM. The day after the bacteria were pelleted at 3000RCF for 10 minutes at 4°C. Pellets were then resuspended in 25mL lysis buffer (1mM beta-ME-OH, 1:1000 protease inhibitor cocktail, 1mM PMSF, 0.1mM DNAse, 1mM Lysozyme in 50mM TRIS-HCl pH 8.0, 300mM NaCl). Resuspended bacteria were left 30 minutes in ice and then sonicated (30 repetitions of 10 seconds). Bacteria were then centrifuged at 13000 RCF for 40 minutes at 4°C. Supernatant was separated from the pellet and to this was added 20mM Imidazole and then incubated in a nickel column. Column was eluted from nickel column with 300mM Imidazole and the eluate was injected in Superose Increase 10300 HPLC equilibrated with 20mM HEPES pH 7.4. Protein profile was obtained following UV 280nm signal.

Purified mCherry and mT-Sapphire were quantified by 280nm absorption at spectrophotometer. Then, a Real-Time PCR (Thermo-fluorometer, Applied Byosistem PCR) machine was used to assess temperature dependence. 6 wells containing equimolar amount of mCherry or mT-Sapphire were subjected to temperature ramp from 10 to 50°C with 5°C steps. To ensure temperature stability the fluorescence intensity was recorded after 1 minute at the set temperature. mT-Sapphire fluorescence was recorded with 380nm excitation light and 520nm emission filter, while for mCherry a 580nm excitation light and 610nm emission filters were used.

gTEMP2 tested in HEK cells

HEK293T cells were transfected with gTEMP2 plasmid (mT-Sapphire-T2A-mCherry) and then visualized at different temperature at confocal microscope. Petri dish was placed in the QE-1 Quick Exchange Platform to control temperature. Temperature was monitored trough the same thermocouple used in electrophysiology recording. First, cells solution was changed with ice cold PBS. An image of a field containing 25 transfected cells was taken at 9°C. Then heater controller of QE-1 was turned and set to 50°C. During the warming, images were taken at 24, 27.5, 29, 33 and finally at 50°C.

Raster Image Correlation Spectroscopy (RICS) measurements

RICS measurements were performed with a scanning confocal microscope Nikon Eclipse-Ti (Nikon). For each measurement, 100 images were collected with oil 60X objective, 256x256 pixels, 50nm pixel size, 488nm laser power 1, detector 520/50 gain 100 (HV linear correction), pinhole 2, dwell time 9.5us/pixels, 3.668 ms per line. Permanent neodymium magnet used were a ring magnet (26mm width, 20mm internal diameter, 2mm height) or a bar magnet (5mmx5mmx20mm). Both magnets are axially magnetized and were purchased at Magfine Srl. For ring magnet experiment, magnet was placed in the middle of the petri and observation volume was in the middle of the ring, with a measured magnetic field of about 80mT. For the bar magnet experiment, magnet was placed inside the petri and the observation volume was at the edge of bar corner, with a measured magnetic field of about 80mT. Image stacks were analyzed with SimFCS software using a moving average of 10 frames. The fitting was performed with a single component function by using the experimental parameter of the acquisition described above.

Inductively coupled plasma atomic emission spectroscopy (ICP-OES)

Prior to ICP-OES measurement, samples were mineralized using a Mars One Microwave Digester (CEM, Matthews, U.S.A.). 5mL of nitric acid were added to the samples and then diluted to 30mL with MilliQ water. For the mineralization, 20 minutes at 200°C with a power of 500-800W at a pressure of 800 psi were done. ICP-OES analysis was performed with a 5800 ICP-OES instrument (Agilent) following standard protocol for iron detection.

Result and discussion

Chapter 1: Engineering temperature sensitivity in the potassium channel Kcv_{NTS}

The first step in the creation of a potassium magneto-genetic tool, is to build a K^+ temperature sensitive channel. To accomplish this task, we have used a synthetic biology approach, coupling a K^+ channel that is not regulated by any stimuli with a cytosolic temperature sensitive domain added at the pore C terminus. We decided to take advantage of the family of viral potassium channel Kcv, which have been successfully used in other synthetic biology approaches (Alberio et al., 2018; Arrigoni et al., 2013; DiFrancesco et al., 2015). The Kcv channel from ATCV-1 viruses has a critical phenylalanine, Phe78, at the very end of the second transmembrane domain, that is crucial for the pore gating (Rauh et al., 2017). A phenylalanine in the same position was found also in the ATP-sensitive K^+ (K_{ATP}) channel Kir2.6 (Rojas et al., 2007) and interesting enough also in $BacNa_v$ channels (Shaya et al., 2014), the bacterial channels containing the cytosolic temperature sensitive domain (CTD). Therefore, Kcv coming from ATCV-1 seemed an ideal candidate for our engineering project. In particular, we have chosen Kcv_{NTS} (Kcv Next To Smith) because of its high open probability compared to other ATCV-1 Kcv_s (Kcv_{NTS} P_o=0.84 vs Kcv_S P_o=0.35) (Rauh et al., 2017).

EGFP fusion to the protein of interest is a common method to evaluate the protein expression and localization. Since the temperature sensitive domain of BacNav channels is a cytosolic C-terminal domain, we have created the fusion protein EGFP:Kcv_{NTS} in which EGFP is fused at N-terminus of KcvNTS. We compared the electrophysiological properties of EGFP:Kcv_{NTS} with those of the already characterized Kcv_{NTS}:EGFP (with the EGFP at the C-terminus) (Greiner, 2011). Both constructs were transiently expressed in HEK293T cells and whole cell currents were recorded at room temperature with the voltage step protocol shown in Figure 7A, that consists of 20mV voltage steps from +60 to -160mV with a holding at -6mV and a post pulse at -80mV. The pipette solution contained 130mM K^+ while the bath solution contained 100mM K^+, giving a theoretical K^+ Nerst potential of -6mV. Figure 7B shows a representative recording of a cell expressing EGFP:Kcv_{NTS} before (upper image) and after (lower image) addition of 5mM $BaCl_2$, a known blocker of Kcv_{NTS} (Greiner, 2011). The same is shown also for Kcv_{NTS}:EGFP in Figure 7C. In both cases the channel is constitutively open in the range of 0 to -80 mV and can be closed by the addition of $BaCl_2$. However while Kcv_{NTS}:EGFP is an outward rectifier, showing a negative slope conductance at negative voltages, EGFP:Kcv_{NTS} shows inverse rectification, and the appearance of a slow, time-dependent component at negative voltages. (Figure 7B, upper panel). To better understand the differences between the two constructs, the I/V relationship obtained by the average of 5 cells expressing EGFP:Kcv_{NTS} or Kcv_{NTS}:EGFP is reported in Figure 7D in which currents were normalized to the cell capacitance and the values are expressed in pA/pF. Kcv_{NTS}:EGFP (in green) has the typical feature of many Kcv channels which is a negative slope conductance at extreme (< -100 mV) negative voltages (Gazzarrini et al., 2009; Greiner, 2011; Plugge et al., 2000). Instead, currents elicited from EGFP:Kcv_{NTS} construct (in red) have a non-linear I/V relationship at negative voltages. In conclusion, addition of EGFP at the N-terminus decreases the amount of outward current and increases the inward current compared to the construct with C-terminal EGFP.

We have further followed the localization of the two channels by fluorescent confocal imaging. Figure 7E shows on the left the localization of EGFP:Kcv_{NTS} and on the right Kcv_{NTS}:EGFP. The expression pattern of the two construct is greatly affected by the position of the EGFP: when EGFP is at N-terminus there is no green fluorescent signal inside the nucleus, and the signal is restricted to the internal compartments and plasma membranes (Figure 7E); while when is located at C-terminus the green signal is homogenously diffused in the cell, also in the nucleus. The EGFP localization observed in the case of Kcv_{NTS}:EGFP resembles that published for EGFP alone in the same cells (G. Zhang et al., 1996). It is therefore possible that, in this construct, the EGFP is cleaved from the channel.

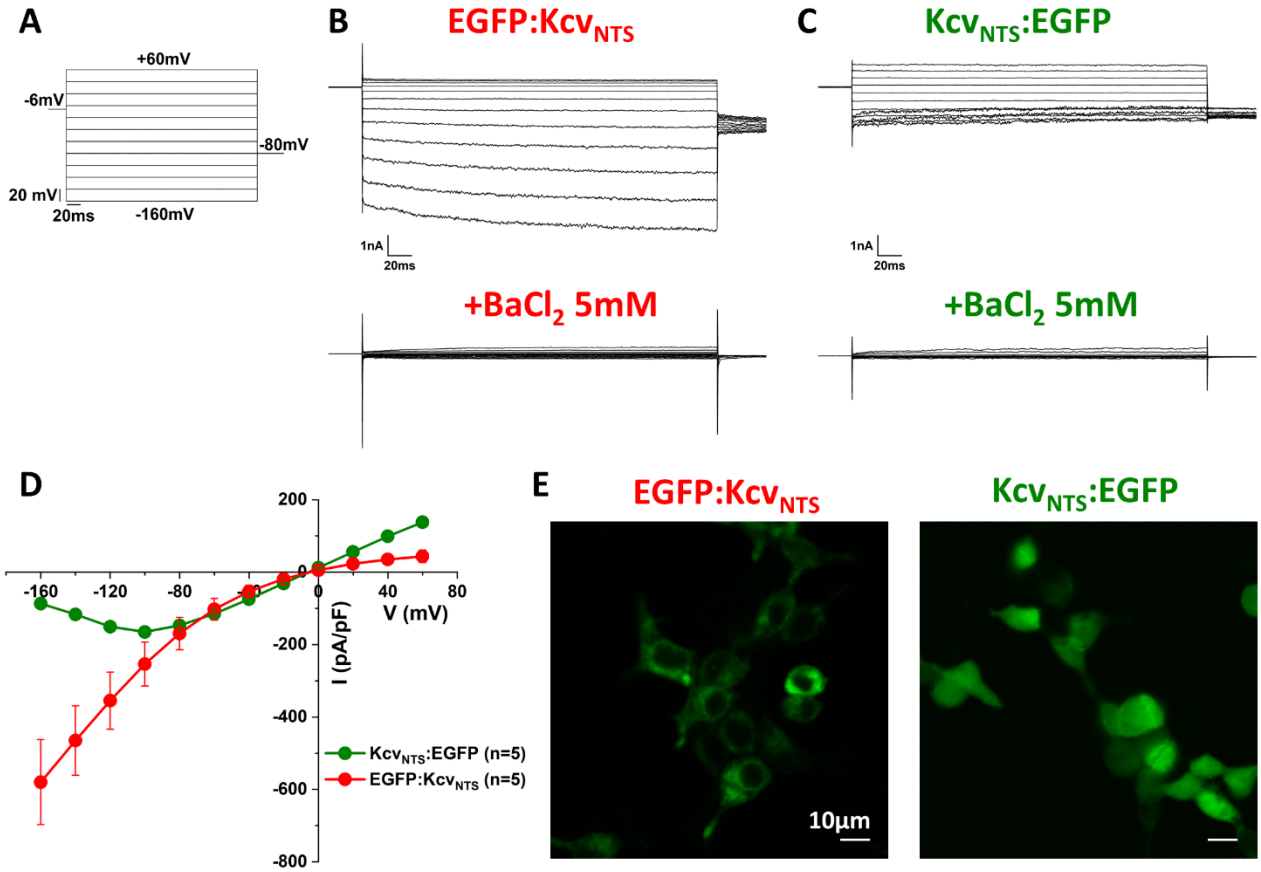

Figure 7: Effect of N or C-terminus EGFP addition to Kcv_{NTS}.

A) *Voltage step protocol used in the recordings present in this figure. 20mV steps were applied from +60 to -160mV. Holding was set at -6mV and tail current was recorded at -80mV. Intracellular solution contains 130mM K^+ while extracellular solution contains 100mM K^+ (calculated Nerst potential for K^+ is -6mV). All measurements were done at 25°C.* ***B)*** *Representative whole cell recording of HEK cell expressing Kcv_{NTS} with a N-terminus or a C-terminus* ***(C)*** *fused EGFP before (upper panel) and after (lower panel) the addition of 5mM $BaCl_2$. The scale is the same in all the recordings, while the scale bar is shown only in the recording before $BaCl_2$ addition.* ***D)*** *I/V relationship for 5 cells expressing EGFP:Kcv_{NTS} or Kcv_{NTS}:EGFP. Current values were normalized for the capacitance of every single cell. Data are shown as average of current density values (pA/pF) ± the standard error of the mean for each construct. The construct with C-terminus EGFP shows the typical feature of Kcv channel, a moderate negative conductance at extreme (< -100 mV) negative*

voltages (Gazzarrini et al., 2009; Greiner, 2011; Plugge et al., 2000). When EGFP is moved to N-terminus the outward current is reduced compared to C-terminal EGFP and the negative conductance at very negative voltages is replaced by an increase of current at increasing negative voltages with a non-linear relationship. ***E)*** *Confocal imaging of green fluorescence of HEK cells transfected with EGFP:Kcv_{NTS} or Kcv_{NTS}:EGFP. The EGFP localization is different in the two constructs: at N-terminus EGFP does not enter in the nucleus while it does enter in the nucleus when it has at C-terminus, probably because of cleavage between EGFP and Kcv_{NTS}. Scale bar is the same in both pictures.*

Addition of the temperature domain to Kcv_{NTS}

Once we have analyzed the impact of EGFP added at N-terminus of Kcv_{NTS}, we started to design the construct comprising the temperature sensitive domain from $BacNa_v$. Among the different channels belonging to the $BacNa_v$ family, we decided to graft on Kcv_{NTS} the C-terminal domain (CTD) of Na_vAe1 (GenBank accession #CP000453.1, PDB ID: 5HK7). This was chosen because Na_vAe1 is the only $BacNa_v$ that is closed in physiological condition and this could be related to the intensity of the constrain that its CTD exerts on the pore module, as discussed in the introduction (Arrigoni et al., 2016). Therefore, this peptide seemed the right choice for obtaining a closed Kcv_{NTS}, that is constitutively open in the physiological range of voltages, as shown in Figure 7B.

The cartoon of the monomer of this construct is shown in Figure 8A, together with the expected behavior of the tetrameric channel inserted in the membrane: the four CTDs, one CTD/monomer, presumably assemble in the cytosolic side of the channel forming a coiled-coil interaction that keeps the pore closed until an increase in temperature induces partial unfolding of the CTDs and the opening of the channel. With the aim of efficiently joining the TM2 α-helix of Kcv_{NTS} with the CTD α-helix of Na_vAe1, we created two possible constructs shown in Figure 8B: version 1 (v1) composed of Kcv_{NTS} 1-75 + Na_vAe1 231-288 and the version 2 (v2) from Kcv_{NTS} 1-80 + Na_vAe1 235-288. Figure 8B shows the alignment of EGFP:Kcv_{NTS}, v1 and v2, with in light-blue highlighted the aminoacids from Kcv_{NTS} and in red the ones from Na_vAe1. The black arrow indicates the phenylalanine involved in gating of Kcv_{NTS} (Phe78), that in v1 is coming from NavAe1 while in v2 is maintained from Kcv_{NTS}. In both constructs the EGFP is at the N terminus.

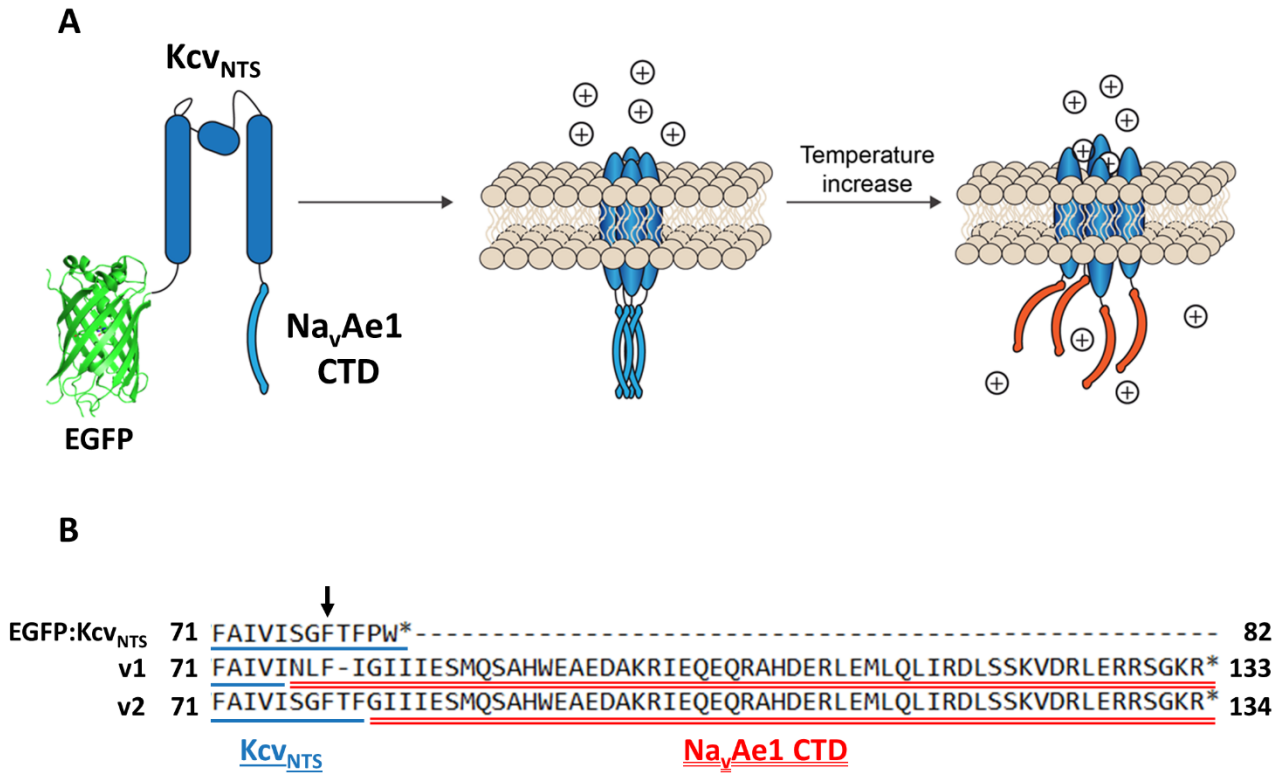

Figure 8: Strategies of Na$_V$Ae1 addition to the C-terminal domain of Kcv$_{NTS}$.

A) *Cartoon representation of the building blocks composing temperature sensitive K^+ channel prototype: to EGFP:Kcv$_{NTS}$ C-terminus was added the C-terminal domain (CTD) of Na$_V$Ae1, which is the domain controlling the temperature sensitivity of this channel. In the left panel the construct is shown as a monomer. When this is assembled in a tetramer and inserted in the plasma membrane (middle panel), the CTD should maintain the pore in a closed conformation (for clarity the EGFP are not shown in the tetramer). When a temperature increase occurs (right panel), the CTD should unfolds leading to the opening of the channel and the passage of K^+ ions.* ***B)*** *Aminoacidic sequence alignment of EGFP:Kcv$_{NTS}$ original construct and version 1 (v1) or version 2 (v2) of CTD addition. Kcv$_{NTS}$ sequence is underlined in light blue while Na$_V$Ae1 CTD sequence is double underlined in red. The arrow indicates the gating phenylalanine: in v1 the phenylalanine is inserted from Na$_V$Ae1, while in v2 is maintained from Kcv$_{NTS}$.*

Functional test of v1 and v2 constructs

To test the properties of v1 and v2 constructs, we expressed them in HEK293T cells and recorded currents by patch clamp from green fluorescent cells at room temperature using the voltage step protocol of Figure 9A. This protocol was adapted from that of Figure 7A, changing the holding potential to -20mV according to the solution used in these recordings (130mM K^+ inside, 40mM K^+ outside, calculated Nerst K^+ potential -30mV). Figure 9B shows a representative recording of a cell expressing EGFP:Kcv$_{NTS}$ before (top panel) and after (bottom panel) the addition of 5mM $BaCl_2$. The current measured with these new solutions and protocol is very similar to the prevoiusly obtained (Figure 7B). The situation changes dramatically looking at the representative recording of v1 shown in Figure 9C. In this case, the amount of current is almost zero, what is left could be given by the endogebous channels expressed by HEK cells. Addition of 5mM $BaCl_2$ has a small effect on the

endogenous HEK conductance, as previously shown (Alberio et al., 2018; Cosentino et al., 2015). Instead, v2 construct resembles the current elicited by EGFP:Kcv_{NTS} even if the amount of current appears to be reduced. To highlight the differences between the three constructs, in Figure 9E is reported the mean I/V relationship obtained by normalized currents recorded from cells expressing EGFP:Kcv_{NTS}(n=4), v1 (n=9) and v2 (n=6). Inset of Figure 9E shows an enlargement with the current reversal potentials of the three constructs. The calculated Nerst potential is -30mV. Both EGFP:Kcv_{NTS} and v2 has a reversal of -27mV, while for v1 is -14mV. Thus, v2 is still an open channel while v1 is not and the current recorded is probably only related to HEK293T endogenous current. A possible reason for the fact that v2 is partly open can be that the α-helices from Kcv_{NTS} TM2 and Na_vAe1 CTD are not perfectly fused into a single helix and this result in a channel that is not completely closed by the addition of the CTD.

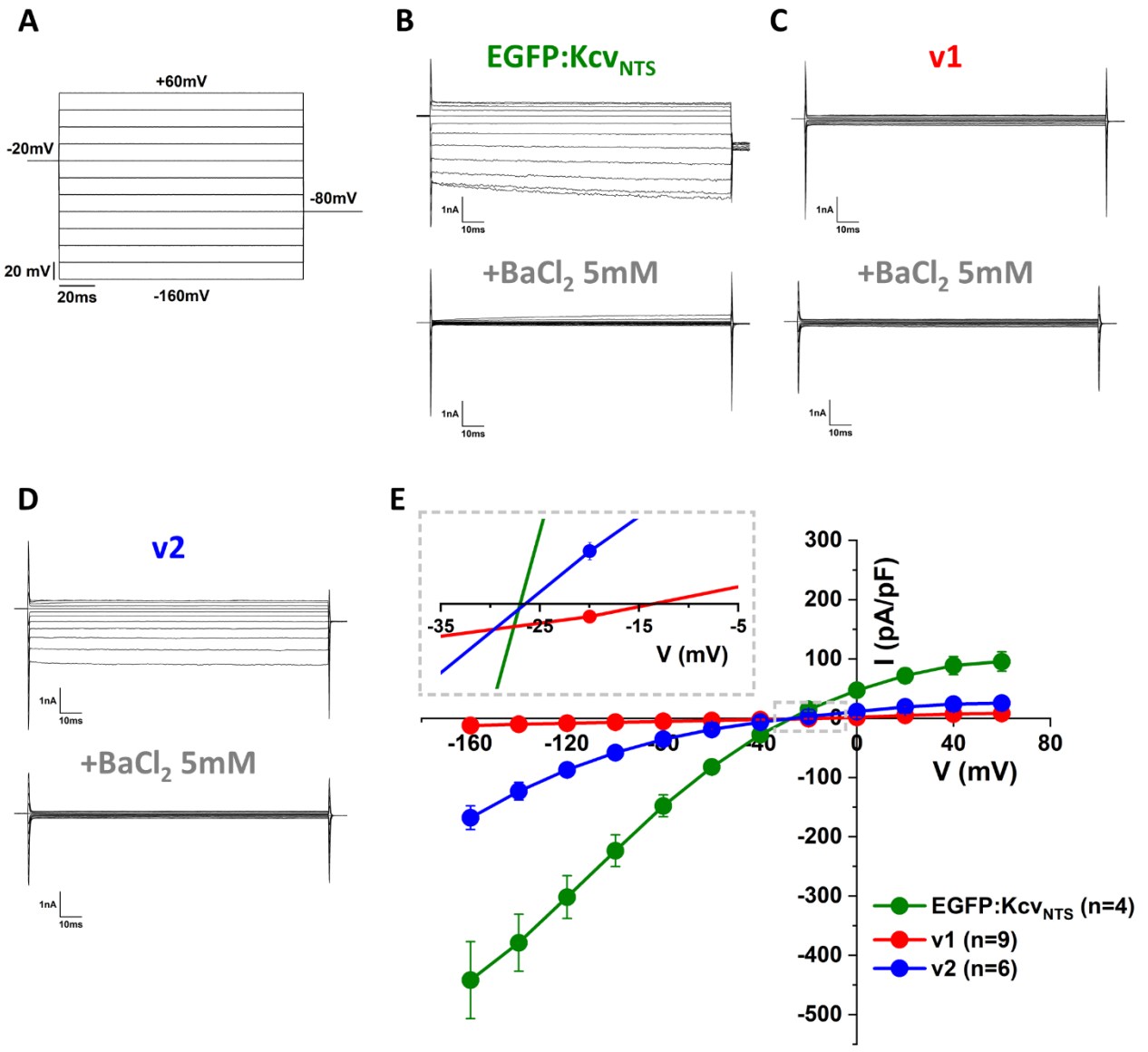

Figure 9: CTD addition to EGFP:KcvNTS has different effect depending on how much of the original sequence is maintained.

A) *Voltage step protocol applied in the recordings of this figure. 20mV steps were applied from +60 to -160mV. Holding was set at -20mV and tail current was recorded at -80mV. Intracellular solution contains 130mM K^+ while extracellular solution contains 40mM K^+ (calculated Nerst potential for K^+ is -30mV). All measurements were done at 25°C.* ***B)*** *Representative recording of HEK cell expressing EGFP:Kcv_{NTS} or v1* ***(C)*** *or v2* ***(D)*** *before (top panel) and after (bottom panel) addition of 5mM $BaCl_2$.* ***E)*** *I/V relationship of the average of 4 cells expressing EGFP:Kcv_{NTS} (green), 9 cells expressing v1 (red) or 6 cells expressing v2 (blue). EGFP:Kcv_{NTS} and v2 maintain the same I/V curve shape, even if the amount of current in v2 is reduced, while v1 expressing cells have a very small current, probably due only to endogenous HEK channels. In the inset (gray dotted line) is shown a zoom of the I/V curve to appreciate the reversal potential for the three different constructs. Both EGFP:Kcv_{NTS} and v2 have a reversal of -27mV, very close to the theoretical value of -30mV, while v1 has a reversal of -14mV, confirming that cells expressing v1 does not have an open Kcv.*

In the case of v1, we need to discriminate between two possible explanations: non-functional channel at the plasma membrane or lack of channel at the plasma membrane. To this end we have analyzed the cells to detect the localization of the fluorescent protein under confocal microscopy.

The synthetic Kcv_{NTS} constructs are localized in the plasma membrane

HEK293T cells were transfected with EGFP:Kcv_{NTS} (Figure 10A), v1 (Figure 10B) and v2 (Figure 10C). In all these three transfections a specific red marker for the plasma membrane (PM), called Cell Mask, was added. Merging the images with the EGFP signal (referring to the localization of the channel) and Cell Mask there gives no clear membrane signal for the GFP tagged channel (Figure 10A, B or C, upper right images). The expression pattern of the three constructs is similar, with no fluorescence inside the nucleus, as was previously observed (Figure 7E). But it is difficult to see any colocalization of the green signal (the channel) with the red signal of the PM marker. This is probably due to the low number of channels reaching the plasma membrane which, nevertheless, due to the high conductance of the Kcv_{NTS} channel, around 80 pS (Braun et al., 2014), can generate currents in the order of nA in whole cell recordings (see Figure 9 and Figure 7). If we applied the relationship $I= N \gamma (V-V_{rev})$, where I is the total measured current at a defined potential, N is the number of open channels in the membrane, γ is the single channel conductance (that is 80pS for Kcv_{NTS}), V is the applied voltage and V_{rev} is the reverse potential, we can calculate the number of channels contributing to the measured current (Alvarez et al., 2002). For instance, if we consider the current measured at -60mV for EGFP:Kcv_{NTS} in Figure 9, which is 82pA/pF with an average cell capacitance of 12pF, we obtain 370 open channels. This is just an approximation that does not consider the amount of current generated by endogenous HEK channels at that voltage but give an idea of the small number of Kcv_{NTS} expressed at the plasma membrane.

Therefore, localization of the few channels to the PM was demonstrated with another approach, i.e. identification of channels on the cell membrane that remain attached to the bottom of the petri-dish, after cell bursting. In this case, the petri dish was treated in advance with poly lysine to strengthen the adhesion of the cells. The treatment consists of ice-cold water addition to the cells and several rounds of washing so that the osmotic shock makes cells explode. After this treatment, the cells were visualized again at the confocal microscope and for all the samples a clear green signal, that colocalize with Cell Mask, is present (Figure 10A, B or C, bottom right image). This result

is very interesting for the v1 construct, indicating its presence at the plasma membrane at a level compatible with the two other constructs (Figure 10B). Therefore, we can conclude that v1 is present at the plasma membrane but in the closed form.

In conclusion, v1 channel is reaching the plasma membrane and is closed. The next step is to understand if an increase in temperature opens this synthetic channel.

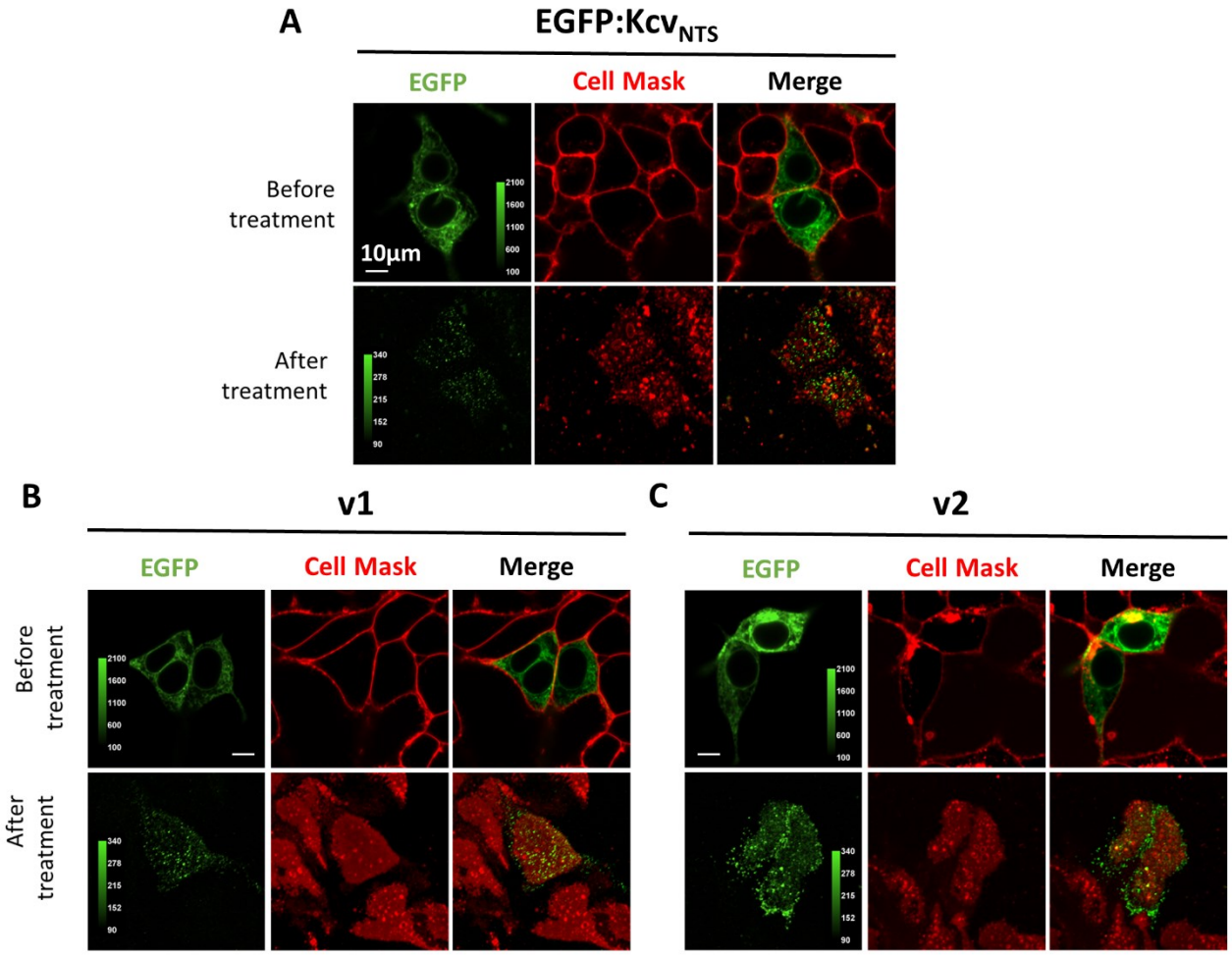

***Figure 10: Membrane localization of different Kcv constructs demonstrate that they all localize with the plasma membrane**.*

***A)** HEK cells were transiently transfected with EGFP:Kcv$_{NTS}$, v1 **(B)** or v2 **(C)**. For all, the three upper images are the cells after 24 hours from transfection. EGFP (left) refers to the EGFP directly fused to the channel, Cell Mask (middle) is the plasma membrane dye and merge of the two images (right) is used to understand if the channel co-localizes with the membrane dye (co-localization appears as yellow signal). The treatment consists in the bursting of the cells with ice-cold water and several washings with the goal to remove everything apart from the cells membrane that remain attached to the bottom of the petri dish. After this treatment the petri were visualized again (lower images) and all the green fluorescence resemble the population of membrane expressed channels. All the three constructs are expressed in plasma membrane. The cells shown before and after the treatment are not the same cells. Scale bar is the same in all images.*

The synthetic channel v1 can be efficiently activated by an increase in temperature

Initially, we have heated HEK293T cells expressing v1 using a Peltier-based system that warms the whole petri dish. Due to a technical problem related to thermic dilatation of the petri dish, it was not possible to record the current by patch clamp from the same cell during the temperature changes, because the movement of the cell was breaking the patch pipette. In this case, we could only compare recordings from population of cells kept at different temperatures. Non transfected (n.t.) cells were compared with cells expressing v1 either at 25°C and 50°C.

Figure 11A shows the voltage step protocol used in this experiment, that consists in 20mV steps from +80 to -120mV. The holding was set at -6mV according to the solution used in this experiment (130mM K^+ inside, 100mM K^+ outside, calculated Nerst K^+ potential: -6mV). This protocol was adopted as standard and used in all the next experiments presented in this thesis. Figure 11B, left column, shows representative recordings of non- transfected (n.t.) cells at 25°C (top panel), 50°C (middle panel) or at 50°C after the addition of 5mM $BaCl_2$ (bottom panel). In all three conditions the currents recorded from n.t. cells are very small (less than 200pA at -120mV). The same experiment was done for cells expressing v1 construct and the representative recordings are shown in Figure 11B, right column. At 25°C, the amount of current recorded is very similar to the one obtained in not transfected cells, however at 50°C a cell with a big current was found (almost 2nA at -120mV). All this current was inhibited by addition of 5mM $BaCl_2$ to the bath, confirming that the current was elicited by an open K^+ channel. The current elicited by v1 has the typical Kcv_{NTS} feature of decreasing conductance at extreme negative voltages (the amount of current at -120mV is almost the same of -100mV). This is particularly evident from the I/V relationship reported in Figure 11B, bottom.

Figure 11C summarizes data recorded from several cells. For each recorded cell, the value of current at -60mV was normalized to the capacitance (current density at -60mV expressed in pA/pF) and the absolute value of current density was plotted in a dot-plot graph. An increase in temperature from 25 to 50 °C, induced no changes in the control cells: at the reference voltage of -60 mV, the mean current is 3.3±2.6 pA/pF at 25°C (n=20) and 3.3±1.4 pA/pF at 50 °C (n=11). On the contrary, the mean current of v1-expressing cells is 1.9±0.4 pA/pF at 25°C (n=23) and 32.4±8.1pA/pF at 50°C (n=16), with a maximum value of 116 pA/pF. A significative difference is present only between v1 at 50°C and all the other samples ($p<0.001$), demonstrating that v1 is a synthetic channel that is closed at 25°C and opens at 50°C.

To understand how many of the tested cells have a current density that exceed the one given by the endogenous channels of HEK293T cells, we set a threshold of 10pA/pF to consider the cell responding to temperature. This value was chosen because 8.3pA/pF was the highest current density value found in non-transfected cells pooling together the values at 25 and 50°C, with a total n=31 (excluding only one cell at 25°C with a current of 10.7pA/pF which can be considered an outlier). With such threshold, 10 out of 16 v1 expressing cells respond to the temperature stimulus, corresponding to the 63% of cells. When another Kcv channel (PBCV-1 Kcv) was engineered to form the blue light K^+ channel BLINK1, the cells responding to blue light were just 10% of the total cell tested (Cosentino et al., 2015). This percentage was increased to 25% when BLINK1 was evolved in

BLINK2 (Alberio et al., 2018). Having a synthetic Kcv that already has a percentage of responding cells of 63% is a big improvement compared to previous synthetic Kcv tools.

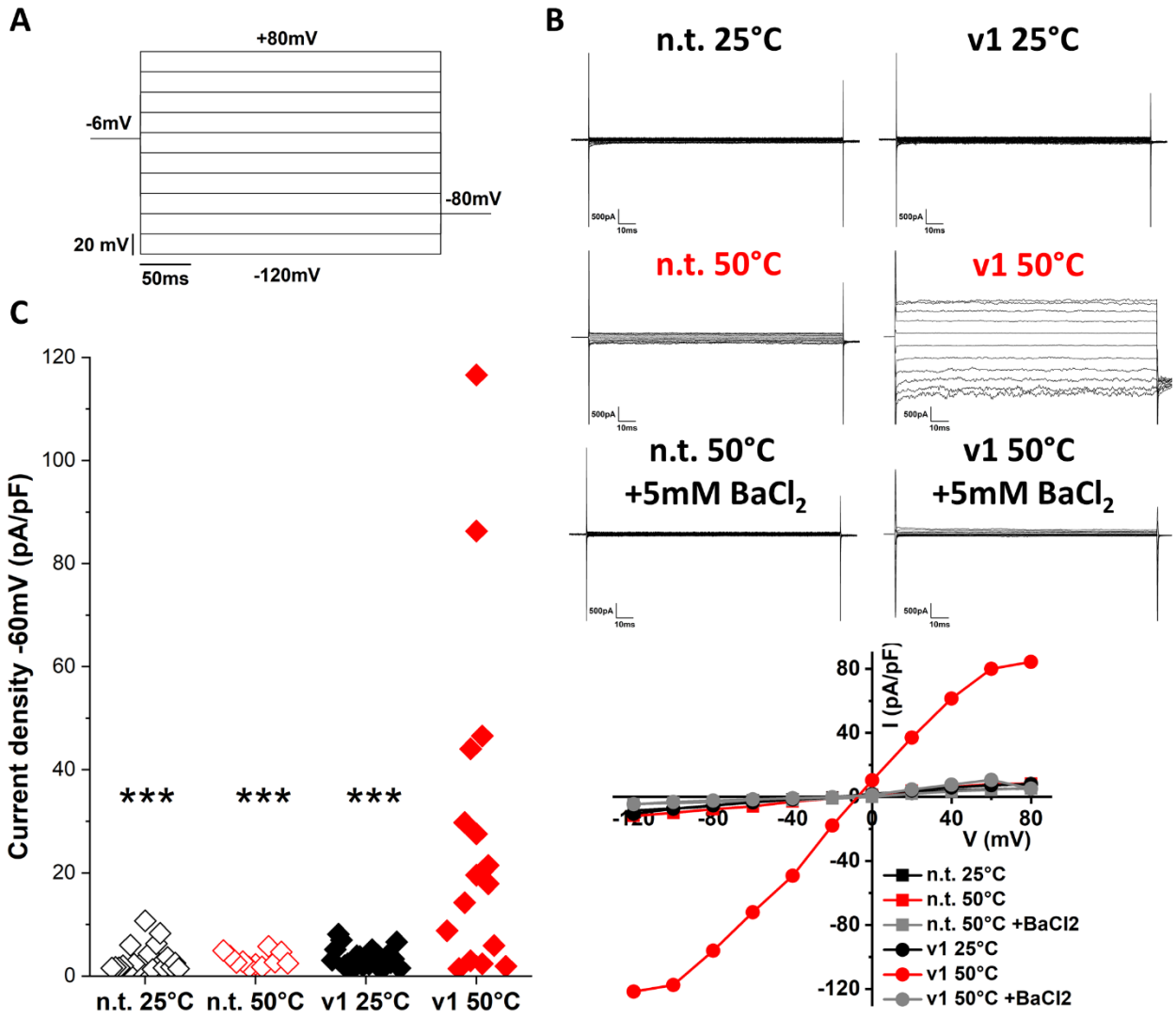

Figure 11: v1 is a temperature activated channel that opens efficiently at 50°C.

A) *Voltage step protocol used in the recordings present in this figure. 20mV steps were applied from +80 to -120mV. Holding was set at -6mV and tail current was recorded at -80mV. Intracellular solution contains 130mM K^+ while extracellular solution contains 100mM K^+ (calculated Nerst potential for K^+ is -6mV). This protocol has been used in all the recordings of this and following experiments present in this thesis.* ***B)*** *Representative current recorded from a not transfected (n.t.) HEK cell (left column) or a v1 expressing cell (right column) at 25°C (top panel), 50°C (middle panel) and 50°C +5mM $BaCl_2$ (bottom panel). The 25°C and 50°C conditions refer to 2 different cells, while the 50°C +5mM $BaCl_2$ is the same cell of 50°C. On the bottom is reported the I/V relationships of all the traces reported above. A Kcv-like current was found only in the cell expressing v1 at 50°C. All this current was depleted by the addition of $BaCl_2$.* ***C)*** *Dot-plot of current density absolute values (obtained normalizing the recorded current with the capacitance of the cell) at -60mV for not transfected HEK293T cells at 25°C (black empty diamonds, n=20, mean current=3.3±2.6pA/pF) and*

*50°C (red empty diamonds, n=11, mean current=3.3±1.4pA/pF) or cells expressing v1 at 25°C (black filled diamonds, n=23, mean current=1.9±0.4pA/pF) and 50°C (red filled diamonds, n=16, mean current=32.4±8.1pA/pF). One-way Anova followed by Fisher test was used to determine statistically significative differences (*p<0.05, **p<0.01, ***p<0.001) between every sample. Only v1 at 50°C has a significative difference (p<0.001) with all the other conditions.*

Single point mutations in the CTD of v1 affect the temperature dependence of the channel

After these first promising results, we set up to further study the temperature dependence of this construct more in details with the goal to discover the minimal temperature that triggers the opening of the v1 channel. We tested 4 different temperatures: 25°C, 40°C, 45°C and 50°C (Figure 12A). Data indicate that opening seem to occur between 40°C (n=8, mean=3.5±0.6 pA/pF, p<0.05) and 50°C (n=16, mean=30.0±8.1 pA/pF). At 45°C only 4 cells were tested but one of them was over the response threshold that we previously set at 10pA/pF at -60mV. The non-statistically significant difference between 45°C and 25° or 40°C is probably due to the low n tested under this condition.

Nonetheless, even 45 °C would be a too high threshold for future application in mammals. In fact, to use efficiently a temperature sensitive channel in mammals it is essential to have a channel that is closed at physiological temperature (36-37°C) and opens just a few degrees above (39-40°C), to avoid or reduce heat shock responses (Lang et al., 2021). To engineer this crucial property for our synthetic tools, we introduced single point mutations in the CTD with the idea to reduce the hydrophobic interactions that keep the four helices together in the coiled-coil motif (Figure 5C). We have chosen not to target the neck because this domain presumably has a higher impact on the folding of the whole domain. In fact, the introduction of 3 glycine in the neck region completely disrupts the temperature dependence of the channel (Arrigoni et al., 2016). We wondered whether mutations in the coiled coil domain would be milder compared to mutation in the neck and, since we just needed to decrease of some degrees the activation temperature, we decided to first test the impact of mutations in this region. We singularly mutated the residues M267, I271 and L274 into Alanine (numbering refers to the residue in the original channel Na_vAe1, Figure 5C). We decided to introduce an Alanine because of its smaller side chain compared to those of the original residues and because is an amino-acid that does not disrupt the α-helical structure. All three mutants were tested in HEK cells at different temperatures, as described before. In the case of the I271A mutant (Figure 12C), 2 out of 4 tested cells had already an open channel at 30°C, making this mutant useless for an application in mammals. For the L27A mutation, 1 over 7 cells recorded at 25°C had an open channel, also making this mutation not ideal for mammals. The most interesting mutation among the tested ones is M267A (Figure 12B). For this mutant, 13 and 24 cells were tested at 25°C (mean current=5.3±0.7 pA/pF) and 37°C (mean current=4.1±0.4 pA/pF) respectively and not a single one has shown at -60mV a current density exceeding the threshold value of 10pA/pF. However, at 40°C (n=12, mean current=8.7±2.8 pA/pF) 2 of 12 tested cells had an open channel (17%). The percentage of cells with an open channel increased with temperature: at 45°C 4 out of 8 cells, 50% (mean=17.5±7.6 pA/pF, n=8) while at 50°C 14 over 27, 52% (mean=21.8±3.8 pA/pF, n=27).

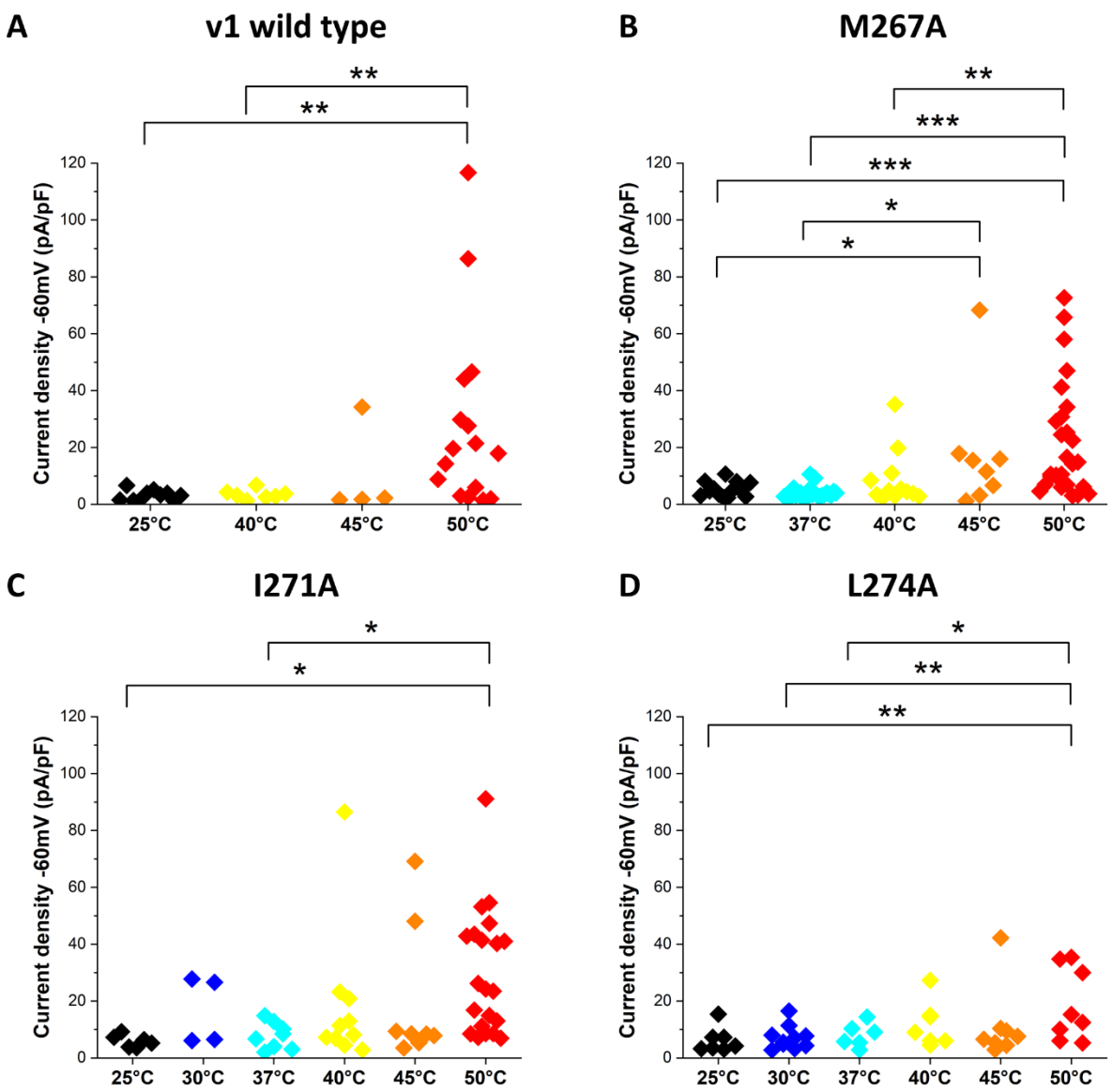

Figure 12: Single point mutations are sufficient to decrease the activation temperature of v1.

A) *Dot-plot of normalized current (expressed in pA/pF) at -60mV of cells expressing the wild type version of v1 at 25°C (n=10, mean current=3.2±0.6pA/pF), 40°C (n=8, mean current=3.5±0.7pA/pF), 45°C (n=4, mean current=9.9±8.2pA/pF) and 50°C (n=16, mean current=30.0±8.2pA/pF).* ***B)*** *Dot-plot of mutant M267A at 25°C (n=13, mean current=5.3±0.2pA/pF), 37°C (n=24, mean current=4.1±0.5pA/pF), 40°C (n=12, mean current=8.7±2.3pA/pF), 45°C (n=8, mean current=17.5±7.7pA/pF) and 50°C (n=27, mean current=21.8±3.9pA/pF).* ***C)*** *Dot-plot of mutant I271A at 25°C (n=6, mean current=5.9±0.9pA/pF), 30°C (n=4, mean current=16.7±6.1pA/pF), 37°C (n=8, mean current=7.8±1.7pA/pF), 40°C (n=10, mean current=18.5±7.9pA/pF), 45°C (n=8, mean current=20.0±8.8pA/pF) and 50°C (n=21, mean current=29.7±4.8pA/pF).* ***D)*** *Dot-plot of mutant L274A at 25°C (n=7, mean current=6.3±1.8pA/pF), 30°C (n=10, mean current=7.1±1.3pA/pF), 37°C (n=6, mean current=8.0±1.8pA/pF), 40°C (n=7, mean current=11.7±3.1pA/pF), 45°C (n=8, mean current=11.1±4.6pA/pF) and 50°C (mean current=18.6±4.6pA/pF). One-way Anova followed by Fisher test was used to determine statistically significative differences (*p<0.05, **p<0.01, ***p<0.001) between every sample. The mutations were designed looking at the structure of Na_vAe1 and inserting Alanine instead of the hydrophobic residues of the coiled-coil part. Mutations shifts the*

activation temperature of v1 to lower values. All this mutations were designed studying the structure of CTD from Na_vAe1 (Arrigoni et al., 2016). The numbers of residues refer to the numeration in the original channel Na_vAe1.

We further tested the combination of two or more mutations to check if they could have a cumulative effect on the temperature dependence. To test this hypothesis, we generated the double mutants M267A I271A and M267A L274A and test them as described above. Figure 13 shows the dot-plots of v1 wild type (data are the same of Figure 12A) and mutant channels. The double mutant M267A I271A, shown in Figure 13B, has 9 out of 11 cells (82%) with an open channel at 50°C (mean current 33.53±7.82 pA/pF) but no cells with an open channel at 45°C (n=3, mean=8.23±1.49 pA/pF) and only 1 out of 11 (9%) at 40°C (n=11, mean=10.34±2.57 pA/pF). None of the tested cells at 37°C (n=6, mean=7.24±0.59 pA/pF), 30°C (n=4, mean=6.53±1.01 pA/pF) or 25°C (n=4, mean=2.0±0.65 pA/pF) shows level of current above the threshold, indicating that these temperatures are not sufficient to activate this double mutant. It is interesting to note that while the two single mutants showed several cells with an open channel above 40°C (Figure 12B and C), the combination of the two mutations does not maintain this property. The results of the second double mutant, M267A L274A, are shown in Figure 13C: at 45°C 7 out of 8 cells, 88%, exhibits current values due to an open channel (mean current=39.51±7.96 pA/pF), 7 of 9 cells, 78%, at 40°C (mean current=14.95±1.82 pA/pF), 3 of 9 cells, 33%, at 37°C (mean current=9.27±1.41 pA/pF) and none of the 5 cells tested at 30°C (mean current=6.23±1.47 pA/pF). This double mutant seems to start to open efficiently at 37°C.

With the aim to further destabilize the CTD structure of v1, we combined the three mutations tested above obtaining the triple mutant M267A I271A L274A. This was tested at 25°C (n=4, mean current=19.27±4.10 pA/pF), and 37°C (n=3, mean current=16.02±1.88 pA/pF) with currents summarized in the dot-plot shown in Figure 13D; apart from 1 cell at 25°C, all the others show at -60mV a current density value over the threshold of 10pA/pF. In the inset of Figure 13D we have reported the I/V relationship as an average of cells tested either at 25°C or 37°C. The resulting I/V curves are almost overlapping, indicating that these channels are already open at 25°C and that an increase in temperature does not affect anymore the properties of this channel. Moreover, the I/V curves resemble the one obtained in cells expressing EGFP:Kcv_{NTS} and v2 constructs (Figure 9E). With the combination of three points mutations introduced in the coiled-coil region we make the CTD unable to maintains a constrain on the channel, leading to the opening of it. This finding highlights the importance of the coiled-coil region in keeping the pore of our synthetic channel closed, as already demonstrated in Na_vAe1, where deletion of the coiled-coil region turned it from a close to an open channel (Arrigoni et al., 2016).

Since the activation temperature range of M267A mutant, closed at 37°C and opening above 37°C, closely matches the temperature range that we consider optimal for mammalian expression, we renamed this variant "Temperature Induced Channel for K^+" (TICK1). Many magneto-genetic tools uses TRPV1, which has an activation threshold of 42°C (Patapoutian et al., 2003). This indicates that ferritin can locally increase the temperature up to 42°C at least. So TICK1 has the possibility to be activated through the same mechanism becoming the first K^+ selective magneto-genetic tool.

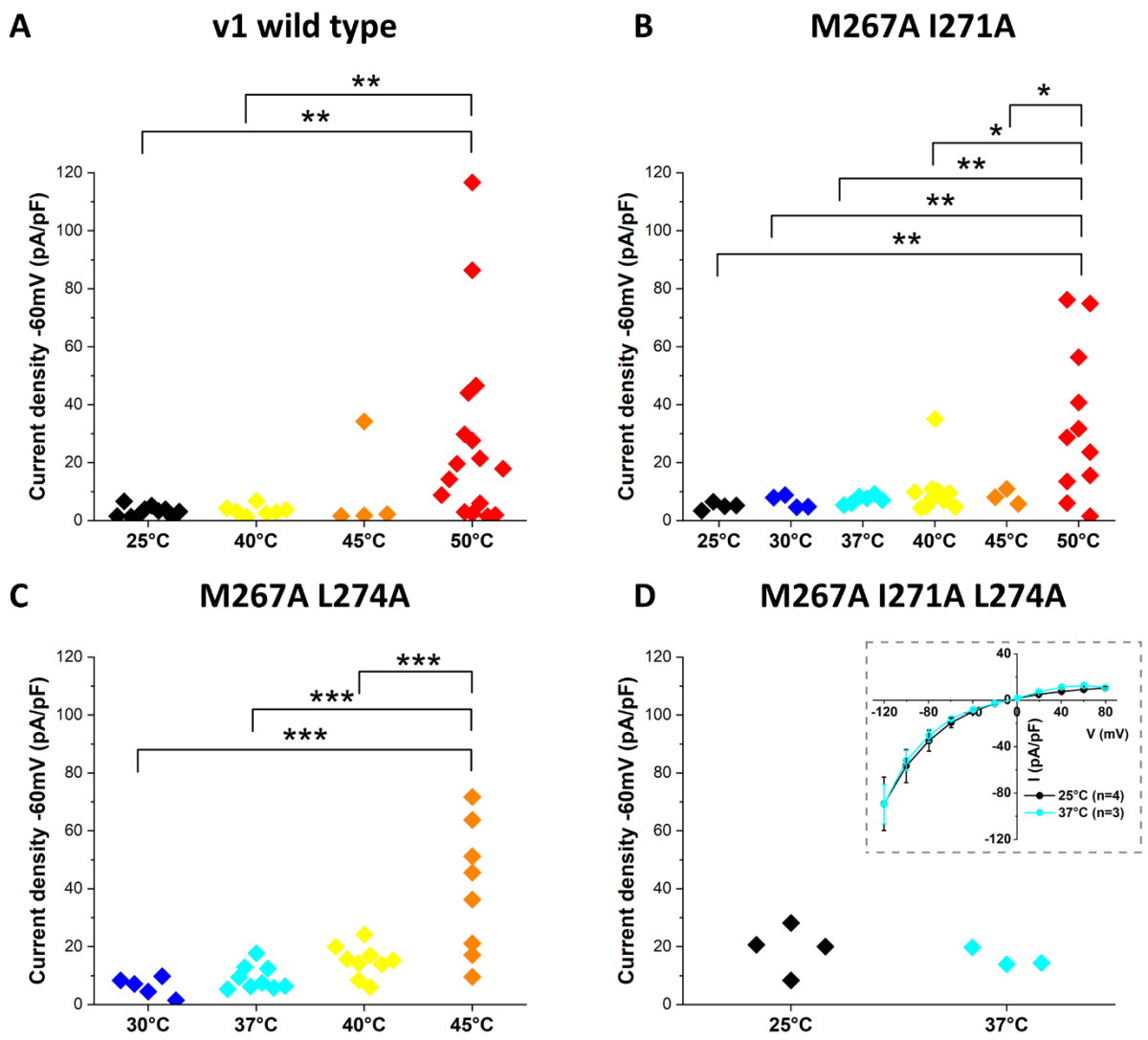

Figure 13: Effect of the combination of three different single points mutations of the coiled-coil region of CTD.

A) *Dot-plot of normalized current (expressed in pA/pF) at -60mV of cells expressing the wild type version of v1 at 25°C (n=10, mean=3.2±0.1pA/pF), 40°C (n=8, mean=3.5±0.1pA/pF), 45°C (n=4, mean=9.9±8.2pA/pF) and 50°C (n=16, mean=30.0±8.2pA/pF).* ***B)*** *Dot-plot of mutant M267A I271A at 25°C (n=4, mean=2.0±0.1pA/pF), 30°C (n=4, mean=6.53±1.0pA/pF), 37°C (n=6, mean=7..24±0.6pA/pF), 40°C (n=11, mean=10.34±2.6pA/pF), 45°C (n=3, mean=8.23±1.5pA/pF) and 50°C (n=11, mean=33.53±7.8pA/pF).* ***C)*** *Dot-plot of mutant M267A L274A at 30°C (n=5, mean=6.23±1.5pA/pF), 37°C (n=9, mean=9.27±1.4pA/pF), 40°C (n=9, mean=14.95±1.8pA/pF) and 45°C (n=8, mean=39.51±7.96 pA/pF).* ***D)*** *Dot-plot of mutant M267A I271A L274A at 25°C (n=4, mean=19.27±4.1pA/pF), and 37°C (n=3, mean=16.02±1.9pA/pF). In the inset (grey dotted line) are shown the I/V relationships obtained by the average of the same cells reported in the dot-plot. This triple mutant is a constitutively open channel and its I/V curve shape is the same of EGFP:Kcv$_{NTS}$ and v2 constructs. One-way Anova followed by Fisher test was used to determine statistically significative differences (*p<0.05, **p<0.01, ***p<0.001) between every sample.*

TICK1 trafficking is lower than other well-trafficking ion channels

Among the cells expressing TICK1, 52% of them showed an open channel at 50°C (Figure 12B). This could be due to a trafficking problem of this synthetic channel, a problem that already occurs with other synthetic Kcv-based channels (Alberio et al., 2018; Cosentino et al., 2015). To further investigate the trafficking of TICK1, we engineered it with an extracellular HA tag. HA-tag is an epitope derived from hemagglutinin protein of human influenza virus (Saiz-Baggetto et al., 2017); it has a sequence of 9 amino acids: YPYDVPDYA. Commercial anti-HA antibodies can be used to detect protein exposing the HA-tag. Kcv from PBCV-1 was previously engineered with an extracellular HA tag (Balss et al, data not published), exploiting the turret region of the channel which is exposed to the outer side of plasma membrane (Gazzarrini et al., 2003). Kcv_{NTS} does not contain this turret region, lacking a consistent extracellular portion (Gazzarrini et al., 2009). We thus decided to engineer TICK1 with the HA tagged turret region from PBCV-1 Kcv (FENNFSVANYPYDVPDYAPDKKA, HA sequence is underlined). This sequence was inserted between the residues G24 and T32 and the resulting construct was renamed TICK1-HA. The same was done for Kcv_{NTS}:EGFP construct to have a comparison with the original channel. Since we already know that TICK1 traffics to the plasma membrane, we decided to compare its trafficking with a channel that we know goes very well to the plasma membrane. This is the mouse isoform of Hyperpolarization-activated cyclic nucleotide-gated 2 (mHCN2) (Zagotta et al., 2003). EGFP:mHCN2 was already engineered to have an HA tag in the extracellular loop connecting S3 and S4 transmembrane domains. As negative control, TICK1 (without HA tag) was used. HEK cells were transfected with EGFP:mHCN2-HA, TICK1-HA, Kcv_{NTS}-HA:EGFP or TICK1 and stained with a primary antibody against HA tag (α-HA) and a secondary antibody conjugated with the fluorescent molecule Alexa633. Cells were then visualized by confocal microscopy and representative images for each sample are reported in Figure 14. For each construct the image of the green signal is reported, related to the fused EGFP. The red signal is due to antibody binding to the HA sequence. A third image shows the merge of the two images. For each sample, on the right are reported the laser power and gain parameter used to acquire the red signal. EGFP:mHCN2-HA shows a recognizable membrane profile already from the green signal, which co-localize with the α-HA signal giving a yellow pattern in the merge image. TICK1 does not give a clear green membrane profile, with a stronger signal in the internal compartment, as observed for its progenitor v1 (Figure 10B). Nevertheless, a detectable red signal was obtained indicating that the amount of TICK1 channels expressed in the membrane is enough to be recognized by this system. Is worth to notice that the red signal parameter used for TICK1-HA are higher than the one of EGFP:mHCN2-HA, with a laser power of 2 instead of 1 and a gain of 130 instead of 50. Was necessary to use different parameters to obtain neither a very low nor a saturating signal in the two samples. This indicates that qualitatively the amount of TICK1-HA channels present in the plasma membrane are less of the one of EGFP:mHCN2-HA. Anyway, the signal of TICK1-HA is higher than the one Kcv_{NTS}-HA:EGFP, indicating that probably the modifications present in TICK1 improved the membrane expression of Kcv_{NTS}. As expected, no red signal was found in the cells transfected with TICK1, since this does not contain the HA epitope necessary for antibody recognition.

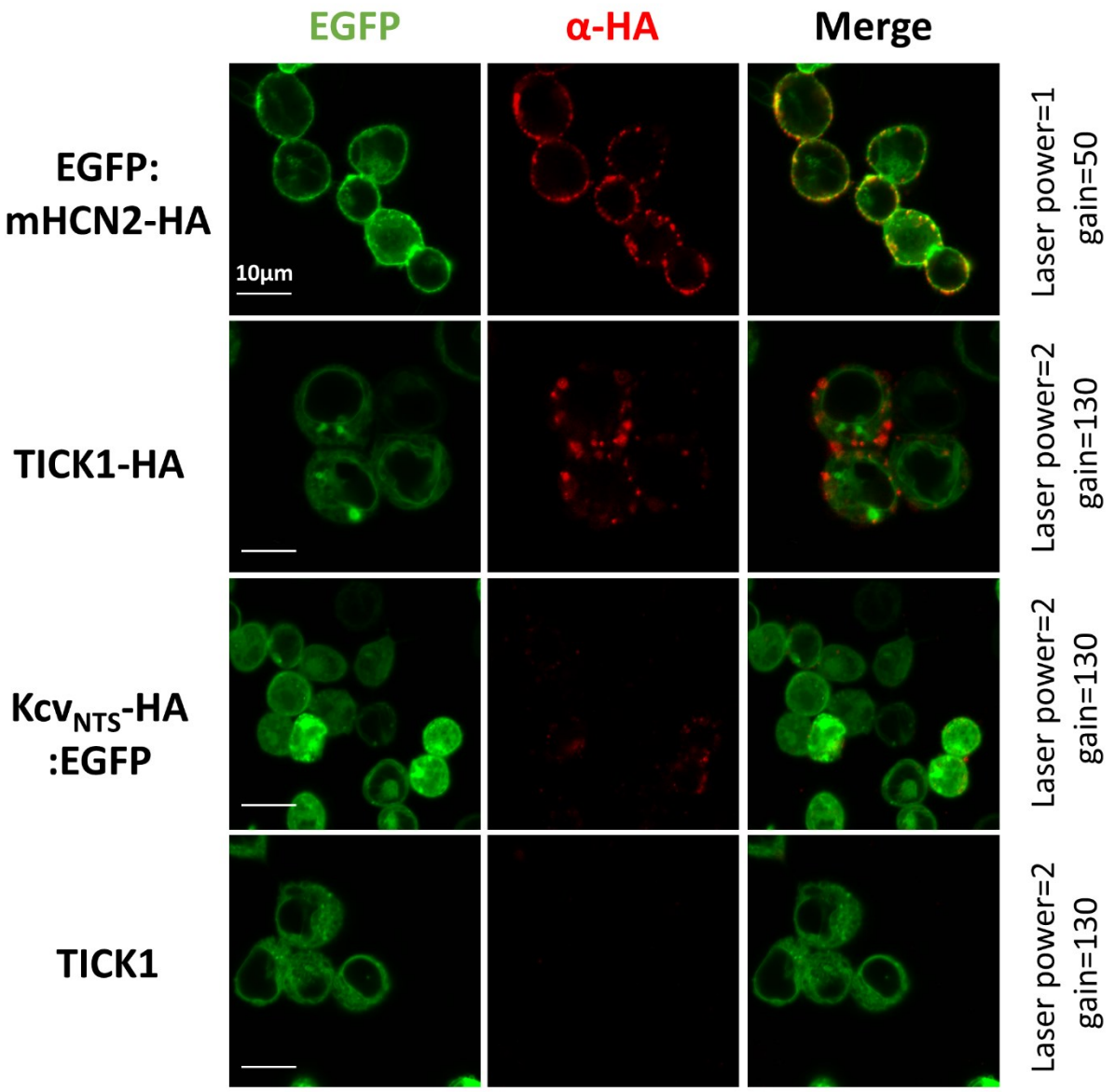

Figure 14: TICK1 trafficking is lower than mHCN2.

Representative images of immunofluorescence of HEK cells transfected with EGFP:mHCN2-HA, TICK1-HA, KcvNTS-HA:EGFP or TICK1. To visualize membrane profile of each construct a primary antibody against HA tag (α-HA) and a secondary antibody conjugated with Alexa633 were used. For each construct are shown the EGFP signal, the α-HA signal and the merge of the two. On the right are indicated the power of the laser and the gain used to visualize the α-HA signal. To see membrane expression of TICK1-HA the laser power and the gain were increased, indicating that this synthetic construct is less abundant at the plasma membrane compared to mHCN2.

Activation-deactivation kinetics of TICK1 are in the second to minute range

A crucial aspect to investigate is kinetic of TICK1 activation and deactivation. To study these properties, we had to set up a system allowing to record current from the same cell during temperature changes. In this case we used a perfusion system (Reid Dan Electronic) that exploits a resistive element to change the temperature of the solution that is perfused to the cell. With this

new setup we could change the temperature without encountering the dilatation of the plastic petri dish that previously prevented continuous patch clamp recordings from the same cell. The temperature of the cell was measured with a thin thermocouple (diameter 0.22mm) placed about 50-100µm from the cell and connected to a digital thermometer. We first evaluated the change in channel activation induced by increasing the temperature from 37°C to 40 °C. We used a gap-free protocol at -60mV. Figure 15A shows the recording from a TICK1 expressing cell: for the first 30 second the cell was maintained at 37°C and then moved to 40°C for 90 seconds. Before the start of the gap-free protocol the cell currents were recorded with the usual voltage step protocol (first light blue arrow) and the currents are shown in Figure 15B, left panel. At 37°C the current was quite stable, around 100pA. After moving the cell to 40°C, the current started to increase with a delay of about 10 sec, reaching a maximum value of around 350pA. We recorded the current with the voltage step protocol also with the cell at 40°C (red arrow). This recording is shown in Figure 15B, middle panel, and resembles the typical current of an open Kcv_{NTS} channel. Later the cell was brought back to 37°C until current reduction. The increase of current occurring at 40°C was stopped by the switching to 37°C, that stabilize the level of current for several minutes. Around 8 minutes after the cells was brought back to 37°C, current starts to slowly decrease and 4 minutes later reaches a stable value around 100pA, which corresponds to the initial value of current.

At the end of the gap-free, a voltage step protocol was made and the obtained recording is shown in Figure 15B, right panel. The current recorded after moving back the cell to 37°C is very similar to the one recorded at the beginning of the experiment, further confirming that the increase of current observed at 40°C was due to the opening of TICK1. This experiment shows us that TICK1 can be efficiently opened at 40°C and it takes 10 seconds to start to open. The increase of current obtained is around 250pA, from 100 to 350pA, at -60mV. TICK1 can be closed by reducing the temperature back to 37°C and the channel remains open for almost 10 minutes before to start to close.

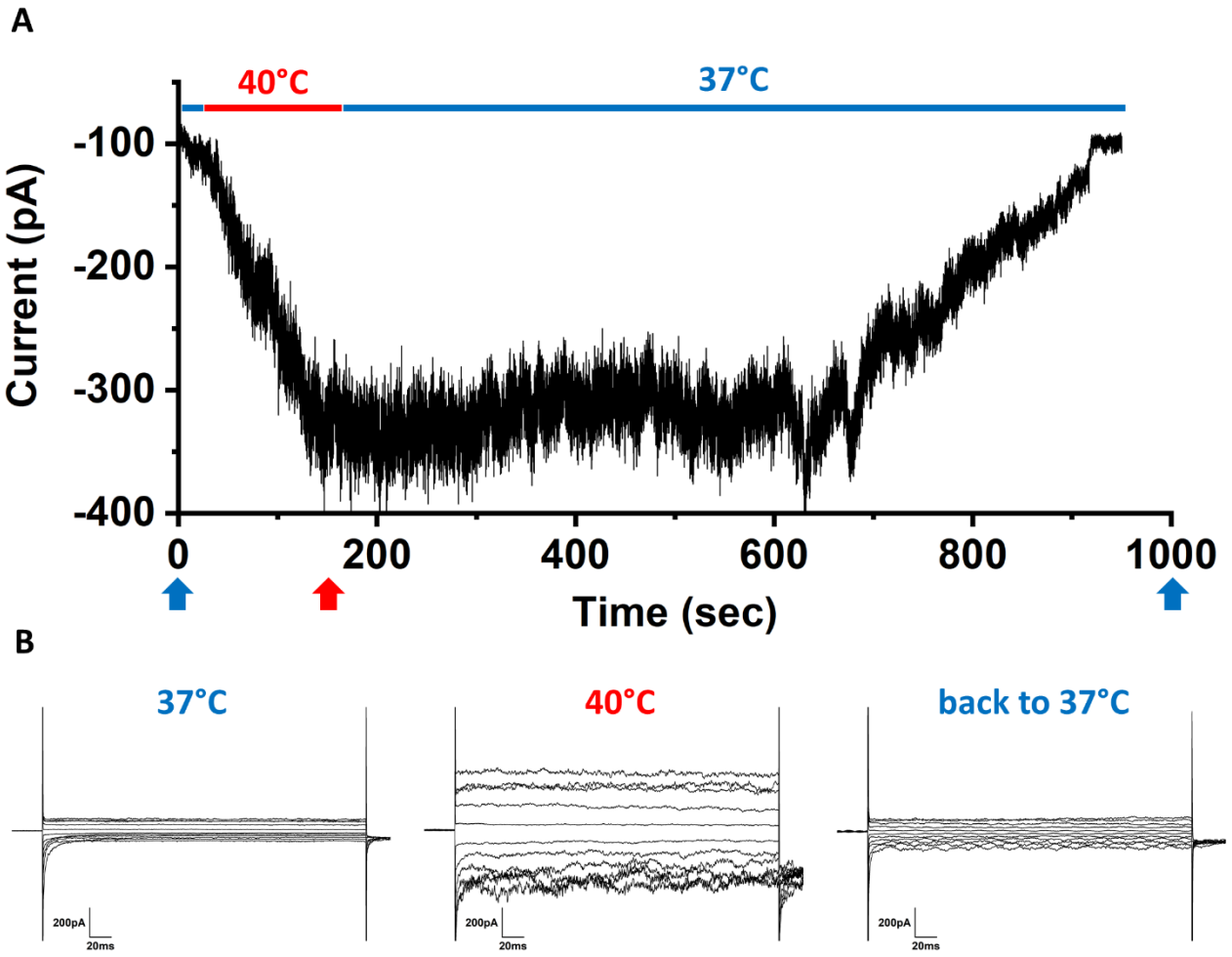

Figure 15: Activation and deactivation kinetic analysis of TICK1 made in gap-free on the same cell.

A) *-60mV gap-free protocol made on a cell expressing TICK1. For the first 30 seconds the cell was maintained at 37°C and then switched to 40°C. The change in temperature from 37 to 40°C required few seconds. The cell was maintained at 40°C for 90 seconds and then switched to 37°C and recorded until current reduction to the initial 37°C current.* ***B)*** *Recording of the same cell at 37°C before the gap-free protocol (first light blue arrow), at 40°C (red arrow) and at 37°C (second light blue arrow) at the end of the gap-free. At 37°C a small current was recorded, then a typical Kcv current was recorded at 40°C. After around 12 minutes back to 37°C the current goes back to the initial 37°C values. Temperature was measured with a thermocouple placed 50-100µm from the cell.*

Unfortunately, to obtain these data on the same cells big efforts were made and this was the only cell resisting the whole process. We thus decided to reduce the stress of the cells during the recording dividing the activation from the deactivation and passing from a gap-free protocol to a protocol in which current is recorded with a single step at -60mV every 10 seconds for the activation or 30 seconds for the deactivation.

TICK1 opening is in the range of tens of seconds

Figure 16 shows in panel A an exemplary experiment performed in this manner. In EGFP expressing cell, increasing the temperature from 37 to 40°C elicited an insignificant fluctuation in the amount

of current showing a small increase of around 2pA/pF. The endogenous current was slightly reduced by the addition of 5mM $BaCl_2$, as already reported (see Figure 11b) (Jiang et al., 2002; Ponce et al., 2018; Yu & Kerchner, 1998). In a TICK1 expressing cell the same temperature increase elicited a ten-time higher increase in current of almost 20pA/pF of increment, and this current was completely blocked by $BaCl_2$. For the kinetic of TICK1 activation the data were fitted with a mono-exponential function starting with the time points at 40°C before barium addition. The fitting is reported in Figure *16*A as a red dashed line. The τ obtained from this fitting is 5.5±2.7 seconds.

In Figure 16B we plot the average value of 5 different cells expressing either EGFP or TICK1, including the cells of Figure 16A. In this case the cells expressing TICK1 have in average an increase of current of 8pA/pF, that is less compared to the cell shown in Figure 16A but still more than the 2pA/pF of average increase recorded in the cells expressing EGFP. Looking at the activation kinetic of the 5 cells expressing TICK1, we can see that the current increase is measurable already after 10 seconds at 40°C, while it takes ca. 40 seconds to reach a plateau. To better evaluate the activation kinetic a mono-exponential fitting of the data was performed, obtaining a τ value of 10.2±3.1 seconds.

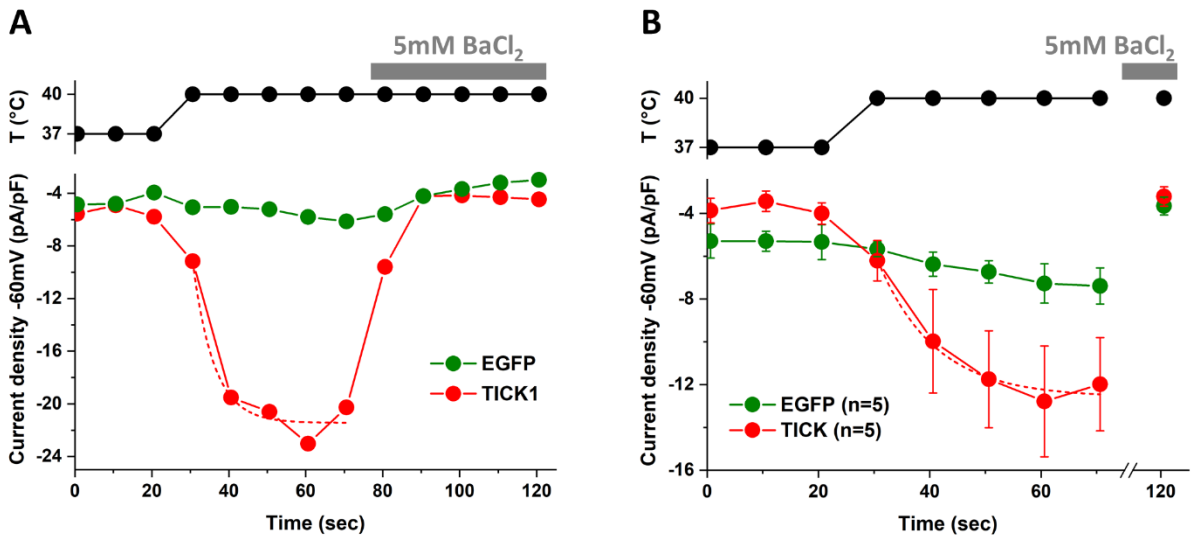

Figure 16: TICK1 activation reach saturation after 40 seconds at 40°C.

A) *Activation kinetic of TICK1. Cells transfected with TICK1 (red dots) or EGFP (green dots) were recorded for 300ms at -60mV every 10s. After 20 seconds (three points) at 37°C the same cell was moved at 40°C to follow the activation of the channel. At the end of the protocol 5mM $BaCl_2$ was added (gray bar on top) to test if the activation was due to the opening of a K^+ channel. For both a representative cell is shown. Only TICK1 expressing cell shows a robust current increase passing from 37 to 40°C. Red dashed line represents the mono exponential fitting of TICK1 activation at 40°C. The calculated τ is 5.5±2.7 seconds.* ***B)*** *Comparison of the mean current density of 5 cells transfected with EGFP (green dots) and 5 with TICK1 (red dots) moved from 37°C to 40°C. 5mM $BaCl_2$ was added at the end of every recording (grey bar on top). Red dashed line represents the mono exponential fitting of TICK1 activation at 40°C. The calculated τ is 10.2±3.1 seconds. Current density increases are negative because at -60mV the current is inward. Temperature was measured with a thermocouple placed 50-100µm from the cell; temperature values for each point are reported in the top part of the image.*

TICK1 closure kinetic is highly variable, ranging from few to tens of minutes

Similarly, we performed experiments to study the deactivation kinetic of TICK1. Together with the activation kinetic, this parameter is crucial for the *in vivo* application of TICK1. To study the deactivation kinetics cells were first brought at 40°C, to activate the channel, and then moved to 37°C. The Current level at -60mV was recorded every 30 seconds. We followed the kinetic of channel closure only in cells with a current density over the threshold value of 10pA/pF measured at 40°C. Figure 17A shows the measurements obtained in 2 cells expressing TICK1 recorded for up to 20 minutes. Data are fitted with a mono-exponential function. Both cells show a slow but constant reduction in current that, after 20 minutes at 37°C, didn't reach a stable level. The kinetic of closure appears different from the one obtained with the gap-free protocol (Figure 15B), in which the current remained stable for almost 10 minutes before starting to decrease. The calculated τ for the red cell is 673±139 seconds and 672±64 seconds for the gray cell. To better understand if the residual current of these two cells is due to open TICK1 channels, we used the voltage step protocol to record the current before and after the addition of 5mM $BaCl_2$. Figure 17B shows I/V relationship of red and gray cells at 37°C (filled circles), recorded at the end of 20 minutes at 37°C, and after the addition of barium (empty circles). In both cells the residual current resembled that of TICK1 and was efficiently reduced by barium addition, indicating that some TICK1 channels were still open.

Other 4 cells, recorded with the same protocol described before, are shown in Figure 17C. These cells are presented separated by the previous ones because in these a stable current plateau was reached. All these cells show faster kinetic of closure, with the calculated τ values of 72±10 seconds for the blue cell, 117±15 seconds for the green, 173±52 seconds for the brown and 66±6 seconds for the purple cell. The brown cell reaches a current level that was under the 10pA/pF threshold, while the blue, the green and the purple did not. We recorded the current of these cells at 37°C until we lost the seal, that coincides with the last point in the graph. For this reason, we couldn't terminate the experiment with the addition of barium.

In the last group we show 2 cells in which the recording was interrupted because the seals were lost before current reached a plateau. These two cells are shown in Figure 17D and the calculated τ values are 333±279 seconds for the gold and 420±314 seconds for the cyan cell. Looking at all the cells on which TICK1 deactivation kinetic was analyzed, the τ values vary in a range from 66 to 672 seconds. To better dissect this variability, further experiments are necessary. $BaCl_2$ addition at the end of every protocol, as done for cells in Figure 17A, would help to understand if open TICK1 channels are still present. The real problem of these measurement is cell loss during most of the measurement, given the slow kinetics of closure of the channel. We already switched from a gap-free to a point protocol, with the aim to reduce cells stress. An option would be to extend the time between every recording, that is now 30 seconds, even if this would negatively impact on the fitting quality, necessary to calculate τ value.

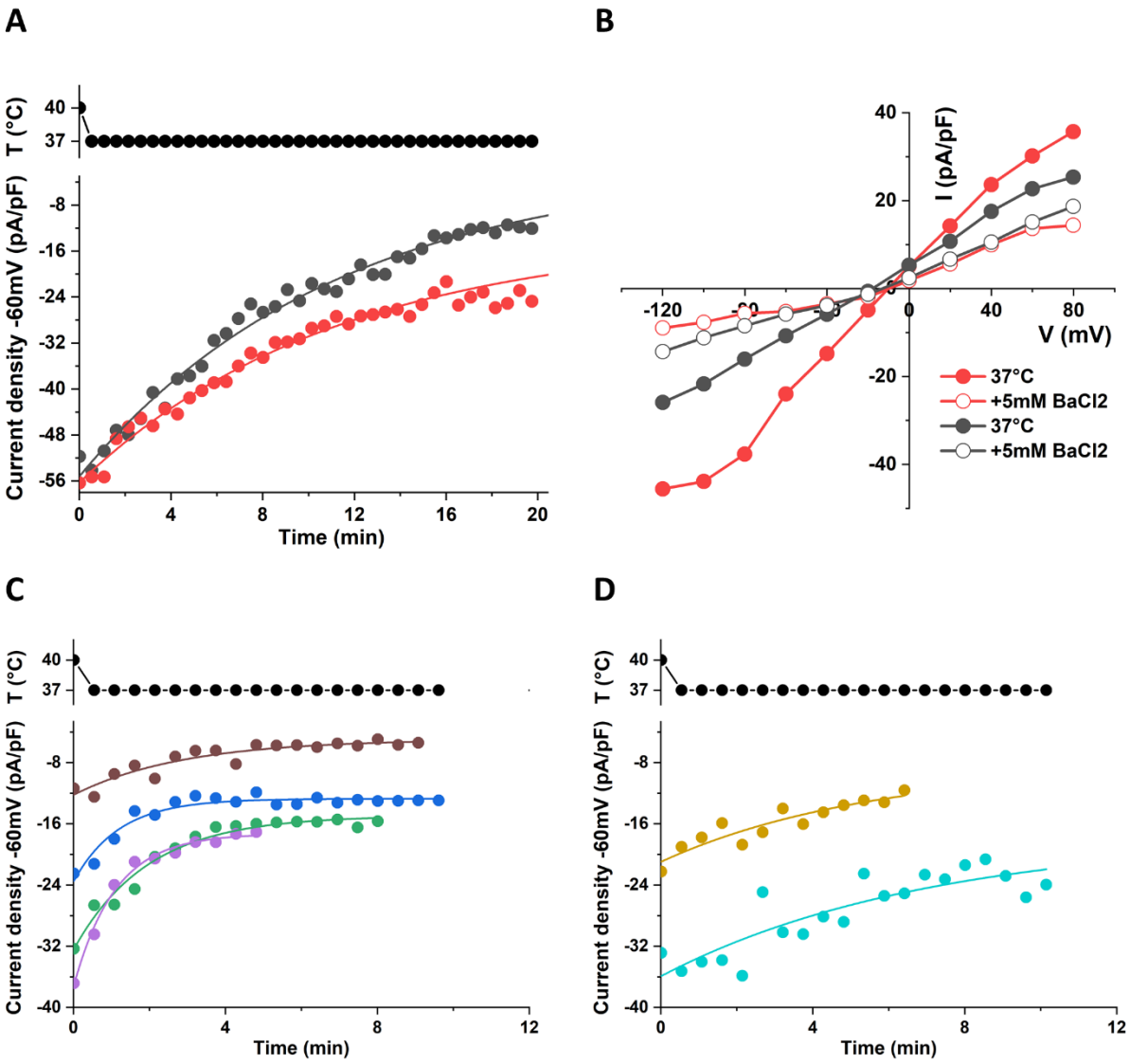

Figure 17: Deactivation kinetic of TICK1 is highly variable.

A) *2 different cells expressing TICK1 were first taken at 40°C (first point of each curve) and then passed to 37°C for 20 minutes to follow the kinetic of TICK1 closing. Current at -60mV was recorded for 300ms every 30 seconds. Lines resemble the mono-exponential fitting result. Temperature is indicated in the upper part of the image.* ***B)*** *I/V relationship of the red and gray cell of (A). For each are plotted the I/V curve obtained after 20 minutes at 37°C (after the end of the protocol applied in (A)) and after the addition of 5mM $BaCl_2$. In both the cells was still present some current that was efficiently blocked by barium addition.* ***C)*** *and* ***D)*** *Plot of current density values of different cells expressing TICK1 moved from 40 to 37°C. Current was recorded as in (A). Lines resemble the mono-exponential fitting result. Temperature is indicated in the upper part of images. The cells were divided in the two graphs depending on their behavior. In (C) are plotted cells that have reached a stable level of current, while in (D) cells with still varying currents.*

Chapter 2: Engineering magneto sensitivity in the temperature-dependent potassium channel

We followed the approach already taken by others (Stanley et al., 2015) to connect a ferritin at the N terminus of the channel. To this end, we added an EGFP-nanobody at the N terminus of TICK and co-transfected the channel and EGFP-ferritin. The expected outcome was to find part of the soluble EGFP-ferritin linked to TICK and thus localized to the cell membrane network.

We used two EGFP-ferritin constructs: in the first one EGFP was fused at the N-terminus of the human Ferritin Heavy chain (hFTH) gene (construct renamed EGFP-hFTH), while in the second one EGFP was fused to the N-terminus of the tandem construct formed by mouse ferritin heavy and light chain genes (construct renamed EGFP-mFT). EGFP-mFT was already used in the pioneer magneto genetic work of Stanley et al., 2015. The EGFP-hFTH construct was created because the ferroxidase activity of ferritin, which is needed for iron accumulation in the core, is found in the heavy chain (Arosio et al., 2017). In addition, looking ahead to the expression of the full magneto-genetic K^+ construct in recombinant adeno-associated viruses (AAV) for *in vivo* expression, it will become useful to have a construct with a shorter sequence length, since AAV allows limited packaging of exogenous DNA (up to 4.7 kilobases (kb))(Flotte, 2000).

First, we expressed the two constructs in HEK cells to follow their expression patterns by confocal microscopy. Figure 18A shows fluorescence and brightfield images of HEK cells expressing EGFP-hFTH (upper panels) or EGFP-mFT (lower panels). For EGFP-hFTH two different phenotypes were found: in both a diffused green signal is present, but only in one of the two phenotypes are also very bright green spots are present. These two phenotypes were found equally among the cells analyzed. These spots are present also in EGFP-mFT expressing cells, but without the green background signal.

To understand how these different expression patterns affect the assembling of ferritin constructs, we harvest the cells expressing either EGFP-hFTH and EGFP-mFT and then we broke them open to extract the total cytosolic proteins, obtaining what is usually called crude lysate. The crude lysate of EGFP-hFTH and EGFP-mFT were analyzed in a size exclusion chromatography column associated with a fluorescent module (F-SEC) in order to identify the protein by means of the fluorescent GFP signal. The result of crude lysate F-SEC is shown in Figure 18B. The column was first calibrated with a mix of protein standards with known molecular weights (mw) (black dashed line). The profile of EGFP-hFTH crude lysate (red line) shows two predominant peaks, marked with A and B. A has approximately the molecular weight of the fully assembled ferritin, 1128 KDa. The ferritin is composed of 24 monomers of 47kDa each (26kDa for EGFP + 21kDa for hFTH). Peak B, which is around 4 time higher than A, has a molecular weight of around 80kDa, compatible with a dimer of EGFP-hFTH, indicating a high degree of disassembly of the ferritin protein. This is probably related to the absence of the light chain, whose structural role is to promote the assembling of the 24-mer (Luscieti et al., 2010). The EGFP-mFT crude lysate (green line) shows an inverted situation. Here the most abundant peak, peak C, runs at the expected MW of the fully assembled ferritin, in this case a 12-mer of 804 KDa. In this construct indeed, the monomer contains the heavy and the light chain and has a molecular weight of 67kDa (26kDa of EGFP, 21kDa of heavy chain and 20kDa for light chain). Peak D instead is very low and corresponds to the mw of the EGFP, about 30 KDa, a

degradation product formed during purification. We thus decided to proceed with the EGFP-mFT construct only.

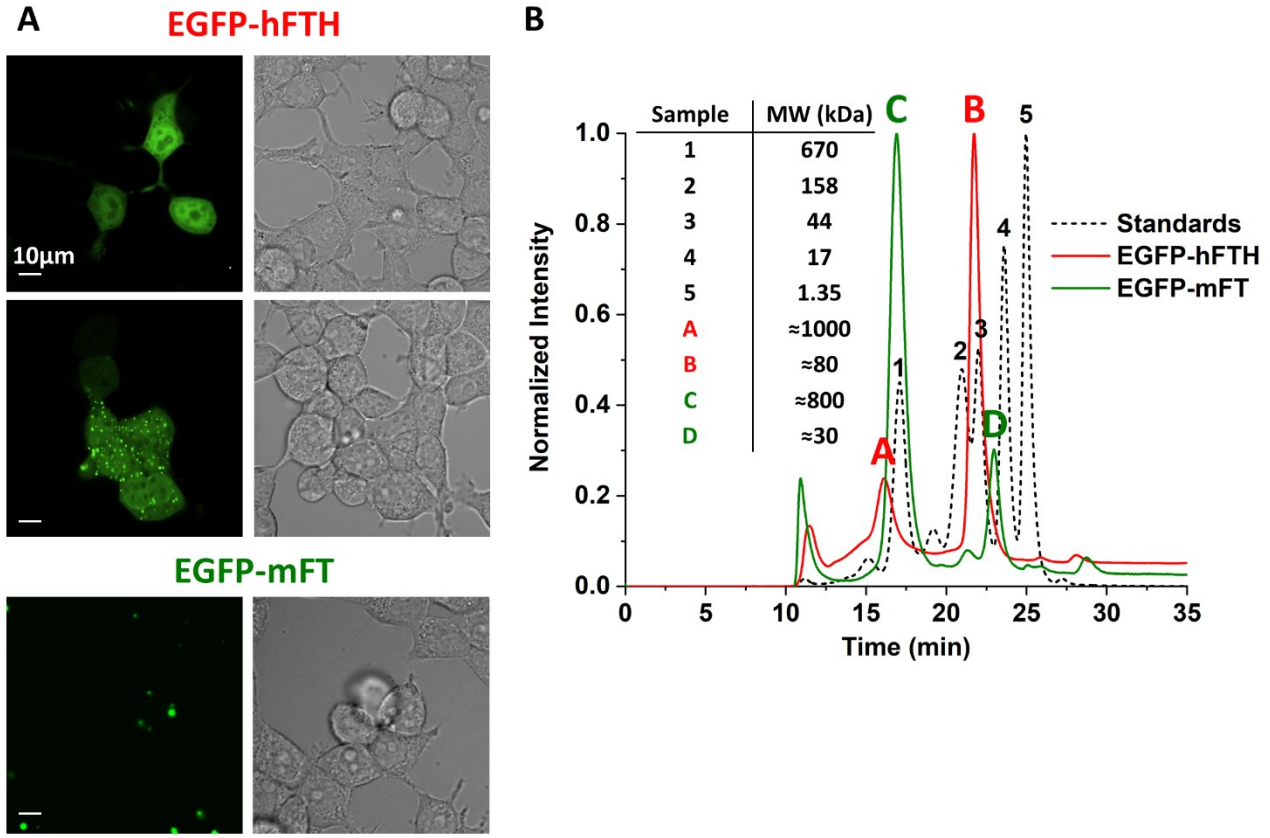

Figure 18: Characterization of expression pattern and dimension of the chimeric EGFP-Ferritin fusion.

A) *Confocal imaging of two different EGFP-Ferritin fusion constructs. Upper part: green fluorescent and brightfield signals from HEK cells transfected with EGFP fused to human Ferritin Heavy chain gene (EGFP-hTFH). Lower part: green fluorescent and brightfield signals from HEK cells transfected with EGFP fused to a fusion of mouse Ferritin light and heavy chain (EGFP-mFT). For EGFP-hFTH two different phenotypes of expression were found: a diffused expression (upper images) or a diffused green background signal together with bright green spots (lower images). For EGFP-mFT only one phenotype was observed, corresponding to very bright green spots corresponding probably to EGFP-mFT clusters.* ***B)*** *F-SEC profile of crude lysates of HEK cells expressing EGFP-hFTH (red) or EGFP-mFT (green). The dark dashed lines resemble the profile of a standard mix composed by 5 different proteins with known molecular weights. The table on the left shows the molecular weights (in kDa) of the 5 standards and the approximative molecular weights of the EGFP-ferritin samples peaks.*

Iron content of ferritins extracted from HEK 293 cells

Ferritin was chosen as alternative to magnetic nanoparticles for its ability to store iron inside its core; it is thus crucial in our view to understand if EGFP-mFT contains iron and how much it contains. We first analyzed iron content of EGFP-mFT with a colorimetric assay based on the chemical conversion of potassium ferrocyanide into ferric ferrocyanide in the presence of ferric iron (see Material and methods for the chemical reaction). Ferric ferrocyanide is a blue pigment formerly

known as Prussian blue and its formation is widely uses to assess the presence of iron in a biological sample (Kim et al., 2012). To have a positive control for iron identification in ferritin, we used the ferritin from the Archea *Pyrococcus furiosus* (Pf-FT), which was provided by Prof. A. Boffi (Università La Sapienza, Rome, Italy) in two versions: APO, that does not contain iron inside, and HOLO, which was *in vitro* loaded with iron. Purified Pf-FT HOLO, APO and the crude lysate from HEK293T cells expressing EGFP-mFT were analyzed on two non-denaturing gel for Native PAGE (PolyAcrylamide Gel Electrophoresis) protein separation (Figure 18C). One gel was stained with Coomassie Brilliant Blue (Figure 18A, left), to visualize all the proteins present in the gel, while the other was subjected to Prussian Blue staining (Figure 18A, right), to visualize the presence of iron. Both PfFT HOLO and APO shows a predominant band around 480kDa in the Coomassie stained gel, corresponding to the expected size of a 24-mer of P*yrococcus furiosus* ferritin (mw =500kDa) (Tatur et al., 2006). The bands, at lower molecular weight, are probably related to partially disassembled ferritins. EGFP-mFT crude lysate shows a smeared signal resembling the total protein content of the cells, since no purification step was applied to isolate specific proteins. No clear signal is present between the 720 and 1048 kDa markers, indicating that the EGFP-mFT 12-mer is not abundant enough in the sample to be detected with this technique. Accordingly, when the native gel is stained with Prussian blue Pf-FT HOLO shows an appreciable signal, with no signal coming from EGFP-mFT sample. The absence of the iron signal in EGFP-mFT could depend on the absence of iron inside the protein or on a sensitivity limit of the Prussian blue staining method. To understand the detection limit of this assay we should build a calibration curve using the Pf-FT HOLO, correlating the intensity of iron signal with the amount of protein.

Still, the presence of fully assembled ferritins as the predominant species in the crude lysate analyzed by F-SEC, prompted us to try an alternative approach, also based on fluorescence, that could provide indication on the iron content inside the ferritins. We performed Raster Image Correlation Spectroscopy (RICS) analysis to determine the diffusion coefficient of the protein in absence or presence of static magnetic fields. Only iron loaded ferritin should be affected by the presence of static magnetic fields. As a positive control we used a sample of purified EGFP, whose diffusion coefficient was reported to be between 80 and 90 $\mu m^2/s$ in standard conditions (Schenk et al., 2004). As permanent magnets, we tested two alternatives: i) a ring magnet (26mm width, 20mm internal diameter, 2mm height), placed inside the petri dish with the observation volume in the middle of the ring and ii) a bar magnet (5mmx5mmx20mm) with the observation volume near the edge of the bar. With both magnets the measured magnetic field was around 80mT but the shape of the filed was different. In one case, the ring, the magnetic field was perpendicular to the sample. In the second case, the bar magnet, the magnetic field was parallel to the sample.

Figure 19B shows a representative stack of images obtained during EGFP-mFT crude lysate measurement by RICS. Each image records the fluorescence of the scanning area where fluorescent proteins are free to diffuse. The brighter pixels correspond to moving proteins and their quasi-horizontal shape derive from the convolution of their movement with microscope line scanning occurring with similar rate.

In every RICS experiment 100 sequential images were collected; here just 6 are reported for clarity. The movie containing all the 100 images was analyzed by using a correlative software obtaining a bidimensional auto-correlation function: the result are reported in Figure 19C. This represents the average profile of ferritin diffusion and appears as a 3D gaussian. From the fitting of this curve the diffusion coefficients were obtained. These are reported in Figure 19D. The sample analyzed were purified EGFP (green), EGFP-mFT (in crude lysate) measured in the absence (red) and in the presence of a magnetic field delivered with a bar magnet (blue) or of a ring magnet (purple). EGFP has a diffusion coefficient of 83.3±2.8 $\mu m^2/s$ (n=22) that matches the values reported in the literature (Schenk et al., 2004). EGFP-mFT without magnet has a diffusion coefficient of 21.4±0.3 $\mu m^2/s$ (n=8), 22.7±0.4 $\mu m^2/s$ (n=13) with the bar magnet and 24.4±0.8 $\mu m^2/s$ (n=6) with the ring magnet. The smaller diffusion coefficient compared to purified EGFP is in line with the bigger size of EGFP-mFT compared to EGFP. Ferritin is a sphere with an external diameter of 12nm, while EGFP is a cylinder with a length of 4.2nm and a width of 2.4nm (Hink et al., 2000). The EGFP-mFT fusion has an expected diameter in the range of 16.8-20.4nm, depending on EGFP orientation. While differences are observed between EGFP and the EGFP-mFT samples ($p<0.001$, One-way Anova followed by Fisher test), no significative differences are present between the EGFP-mFT with or without the application of magnets, indicating that the applied static magnetic field of 80 mT does not exert an attractive/repulsive force on the ferritins strong enough to modify their diffusion coefficient in solution. Still, the open question is whether the absence of magnetic effect on EGFP-mFT is related to lack of iron inside the protein. We therefore went back to our previous strategy, i.e. to measure the iron content in purified ferritins.

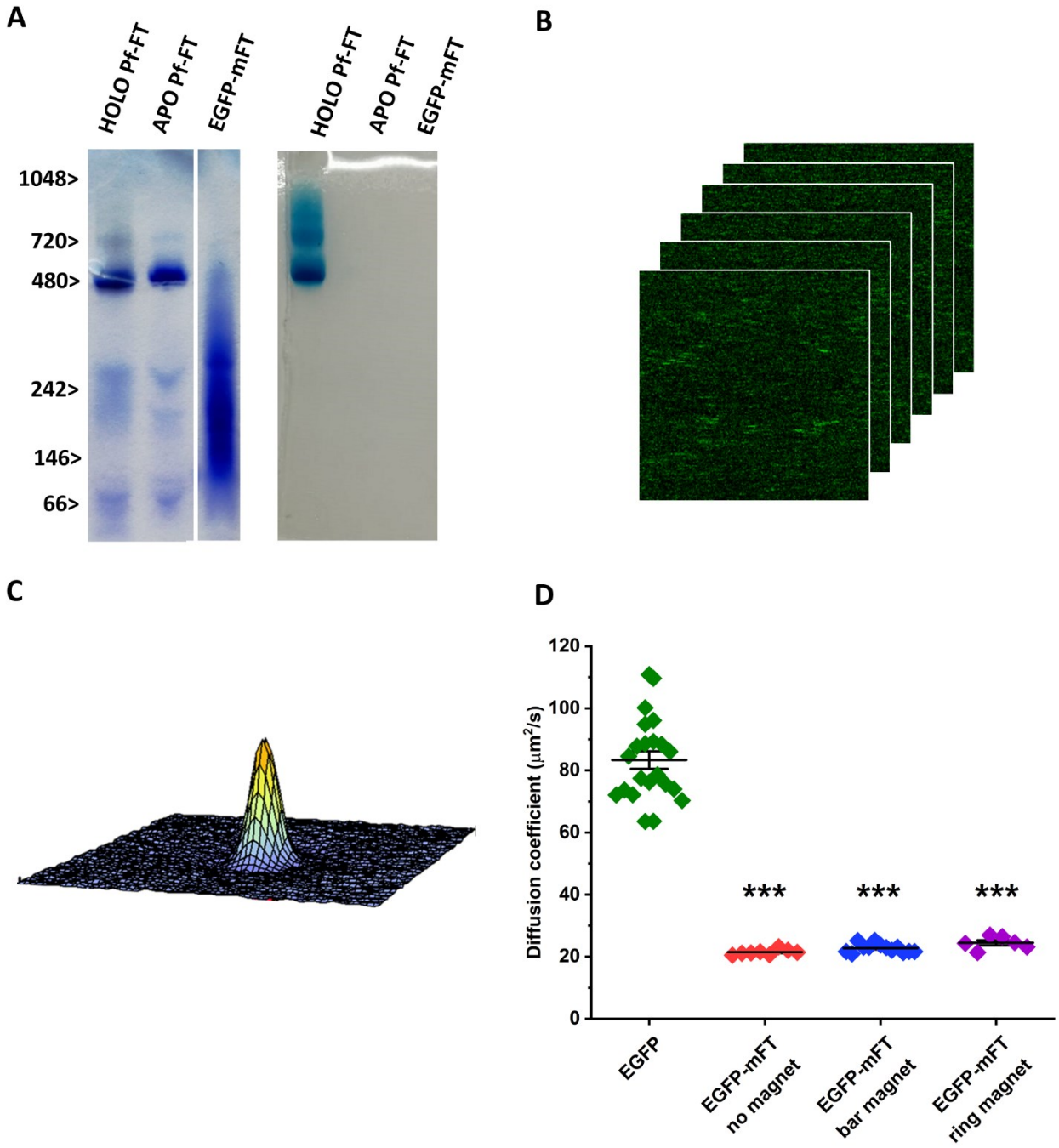

Figure 19: Iron content and magnetic properties of EGFP-mFT.

A) *Native protein gel of Pyrococcus furiosus ferritin (Pf-FT) HOLO, APO and EGFP-mFT crude lysate stained with Comassie Brilliant Blue (on the left), to visualize all the proteins present in the gel, or with Prussian blue staining (on the right), to visualize the iron present in the proteins. Only Pf-FT HOLO shows an appreciable presence of iron. On the left are indicated the molecular weights (in kDa) obtained using a native gel specific marker mix.* ***B)*** *Representative stack of images acquired during RICS measurements of EGFP-mFT crude lysate.* ***C)*** *Auto-correlation curve derived from mathematical analysis of previous stack.* ***D)*** *RICS results of diffusion coefficient (D) of pure EGFP (green, D=83.3±2.8 μm²/s, n=22), as positive control and reference standard, EGFP-mFT crude lysate without magnet addition (red, D=21.4±0.3 μm²/s, n=8), EGFP-mFT crude lysate in the presence of a bar permanent magnet (blue, D=22.7±0.4 μm²/s n=13) or a ring permanent magnet (purple, 24.4±0.8 μm²/s, n=6). One-way Anova followed by Fisher test was used to determine statistically*

*significative differences (*p<0.05, **p<0.01, ***p<0.001) between every sample. Statistically significative difference (p<0.001) was found only between EGFP and all the other samples, indicating no magnetic effect on EGFP-mFT.*

Purified EGFP-mFT disassembles in native protein gel

To purify EGFP-mFT from HEK293T cells we engineered a His-tag at the EGFP protein N terminus. Crude lysate of cells expressing this new construct (HIS-EGFP-mFT) were loaded on a Ni-NTA resin column and eluted with 300mM Imidazole. The eluate was loaded into a size exclusion chromatography (SEC) column and the protein profile was determined following UV (280nm) signal. Figure 20A shows the SEC profile of HIS-EGFP-mFT: a major broad peak occurred between 10-15 ml of elution volume. The two red lines identify the fractions of the peak that were collected, pooled and further analyzed. Figure 20B shows the F-SEC profile of the pooled fractions, in which UV and fluorescence signals were compared to confirm that the protein present in that fractions is fluorescent. To confirm the dimension of this purified protein we superimposed on the same graph the F-SEC profile previously obtained with EGFP-mFT crude lysate (Figure 18B). The crude lysate peak, resembling the EGFP-mFT 12-mer, overlaps with the peak of the purified protein, confirming that the protein is correctly assembled. Purified HIS-EGFP-mFT was then loaded on a native protein gel, with the aim to analyze its iron content by Prussian blue staining. Pf-FT HOLO and APO were again used as control for the staining. Figure 20C shows the native gel stained with Comassie brilliant blue (on the left) or Prussian blue (right). As for the crude lysate analysis performed before, also in this case only the Pf-FT HOLO shows detectable iron content, while no signal is present in the APO or in the purified EGFP-mFT samples. However, the Comassie staining further shows disassembly of the HIS-EGFP-mFT protein. The expected molecular weight is 800 kDa while on the gel, the most abundant band is about 242kDa, that roughly corresponds to a tetrameric assembly of the monomer (about 67 kDa). Also, when crude lysate was analyzed by Native-PAGE no band corresponding to 800kDa was found, even if F-SEC analysis demonstrates the corrected assembly of the protein (Figure 18B and Figure 19A). In that case we had assumed that the low amount of protein in the crude lysate was not enough to visualize it in the gel, but now we could speculate that EGFP-mFT tends to disassemble in native-PAGE gel.

This experiment was not repeated further because we had in the meantime set another procedure to quantify the iron content in purified ferritins.

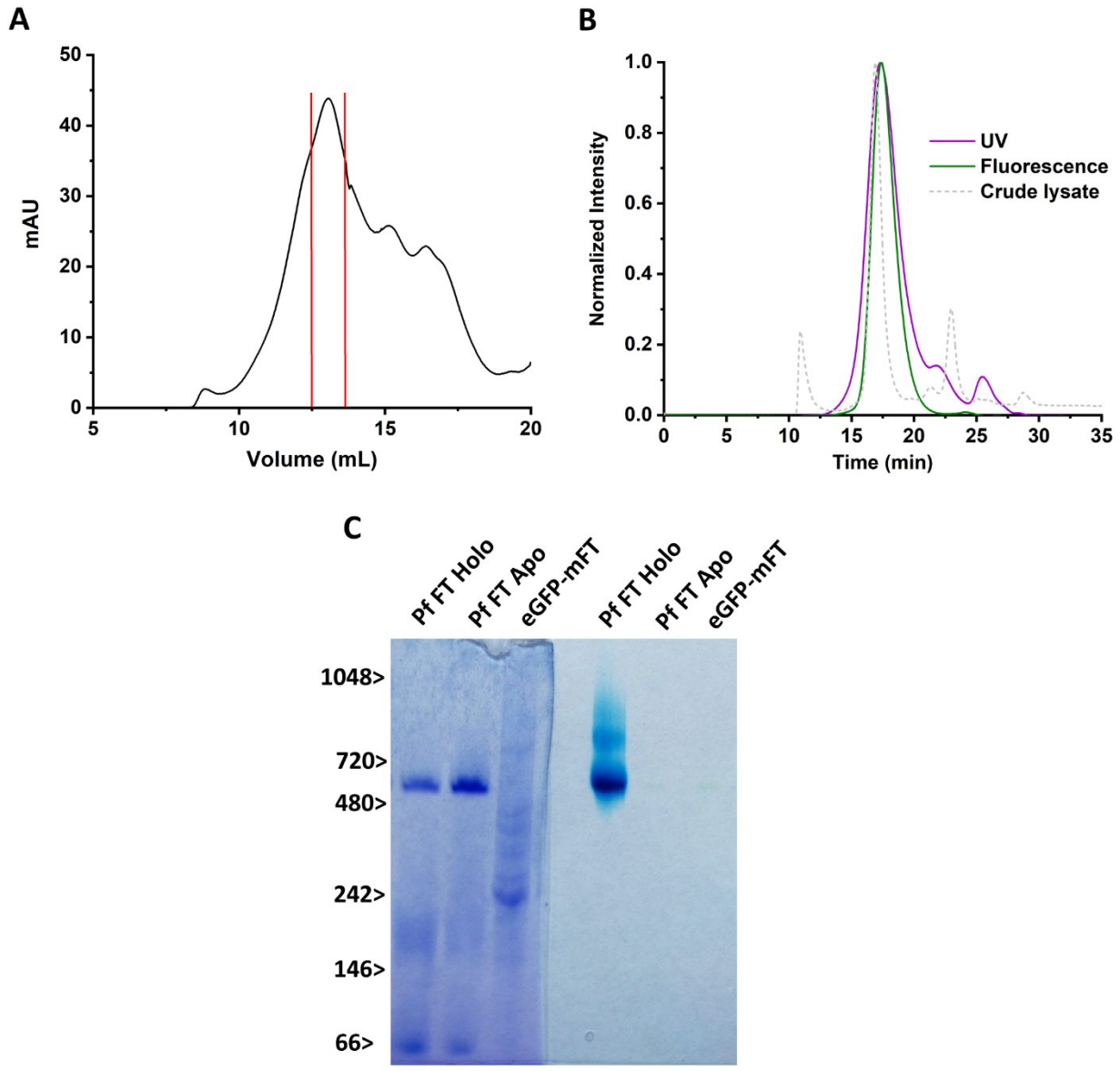

Figure 20: Purification and native protein gel of EGFP-mFT.

A) *Size Exclusion Chromatography (SEC) profile of purified EGFP-mFT. The red bars indicate the fractions that were collected from SEC and further analyzed.* ***B)*** *UV (purple) and fluorescence (green) profile of the EGFP-mFT fractions highlighted in (A) in F-SEC. For comparison, in dashed light gray is reported the F-SEC fluorescence profile of EGFP-mFT crude lysate.* ***C)*** *Native protein gel of Pf-FT Holo, Apo and purified EGFP-mFT stained either with Comassie brilliant Blue (left) or with Prussian Blue (right). Iron was detected only for Pf-FT Holo sample.*

EGFP-mFT contains 583 Fe atoms for each protein

The literature reports a theoretical limit of 4500 iron atoms/ferritin (Tatur et al., 2006). In most of the cases though, ferritins are reported to contain about 500 iron atoms at most. This is particularly true in the case of ferritins extracted from mammalian cells (Salgado et al., 2010)

To overcome the possible too low sensitivity of the Prussian blue assay and the poor stability of EGFP-mFT in native-PAGE, we decided to exploit in parallel other methods for the quantification of

the amount of iron present in the ferritins. In particular, we have exploited the Inductively Coupled Plasma Optical Emission Spectrometry (ICP-OES) technique. This is a spectroscopic technique widely used to measure concentration of elements in a solution sample. The use of this technique gives us two important advantages: first, we can measure the exact amount of iron inside the EGFP-mFT and thus determine how many iron atoms are present in each ferritin and second, even if the ferritin disassembles, the iron remains in solution and can be measured. We thus purified EGFP-mFT again with the same protocol applied before. The SEC profile of this purification (new) is shown in Figure 21A, overlapped with the one previously reported in Figure 20A (old). The fractions included in the red lines were pooled and used in further analysis. Prior to ICP-OES, we used Dynamic Light Scattering (DLS) to measure the protein hydrodynamic radius. DLS is a technique useful to determine the size and shape of molecules in suspension studying how these scatters an incident light beam (Stetefeld et al., 2016). DLS results obtained with the pooled fractions of purified EGFP-mFT are shown in Figure 21B. The sample appears as mono dispersed, since only one peak is present in the range of radius analyzed, from 0.1 to 1400nm. This peak is centered at 9nm of radius, that perfectly matches the theoretically dimension of the EGFP-mFT diameter (between 16.8-20.4nm). Next, we used ICP-OES to measure how much iron is present in this EGFP-mFT sample. The ICP-OES results are shown in Figure 21C. As a control, we included an aliquot of the same buffer solution (PBS) in which the protein was eluted. To measure the iron content of our samples a calibration curve was built using 4 different iron standards with increasing iron concentrations, in the range 0.04 to 0.4 mg/L. Figure 21D reports the values of the 4 standards and our samples. PBS has an iron concentration of 0.045mg/L, while EGFP-mFT of 0.065mg/L. The iron contained in PBS can be presumably attributed to iron contaminations coming from impurity in the powders used for PBS preparation. The iron present in the EGFP-mFT, subtracted for PBS iron, is 0.02mg/L. From the protein concentration, measured by 280nm absorbance, we calculated the moles of ferritin in the sample. These were divided by the moles of iron to estimate how many iron atoms are present in each EGFP-mFT molecule. The result is 583 iron atom/ferritin. This value matches the amount of iron found in mammalian ferritin in physiological condition (Salgado et al., 2010) and is in the range found in mammalian ferritin extracted from horse spleen, which can vary from few hundreds to 5000 (Jian et al., 2016).

This experiment should be repeated to confirm the data, possibly extending the calibration curve in the lower range since iron concentration of our samples are between the first and second point of the curve. Anyway, this is a promising result that demonstrate that the fusion between EGFP and a chimeric light and heavy chain ferritin does contain iron in a physiological range.

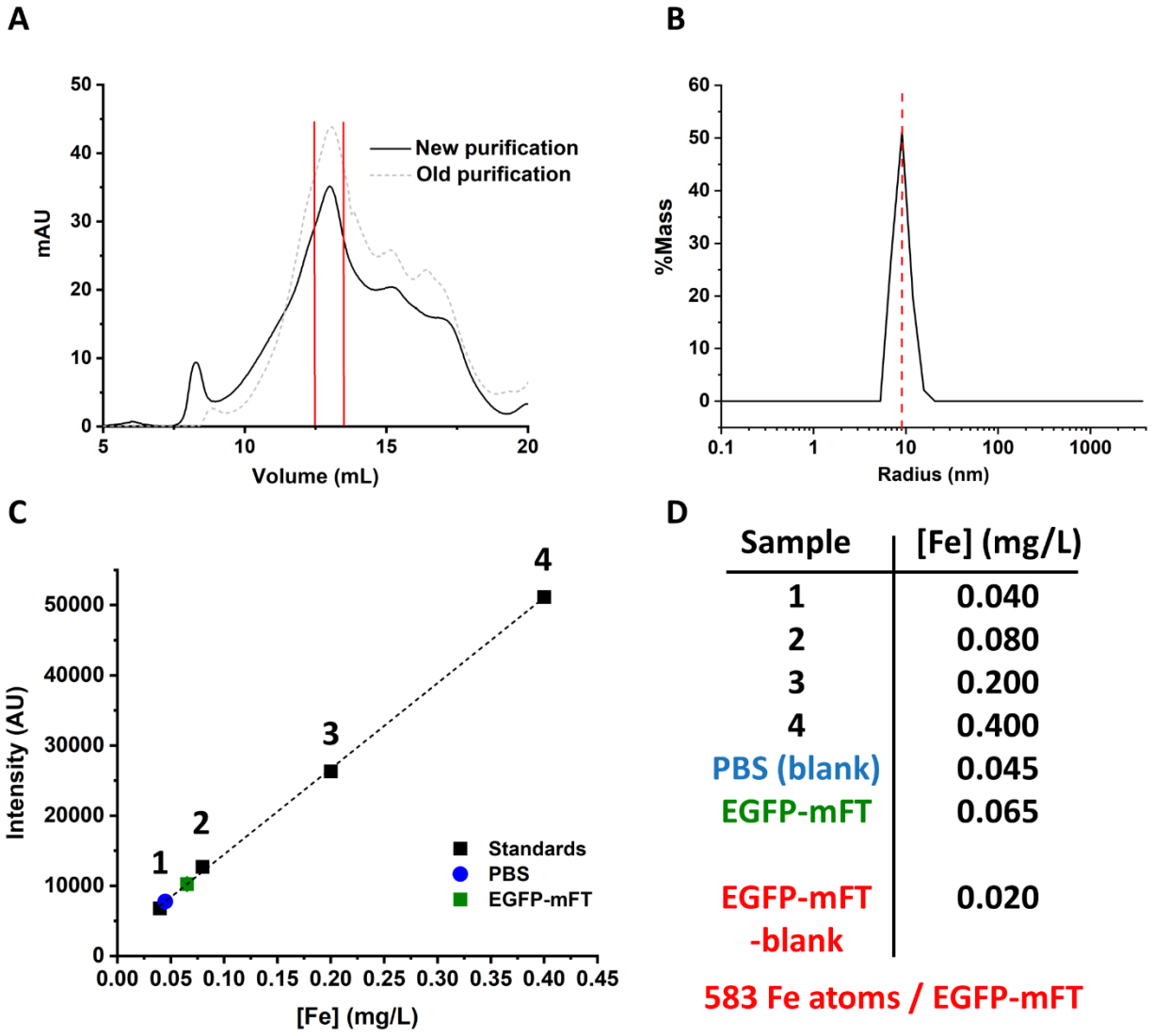

Figure 21: EGFP-mFT iron quantification by ICP-OES reveals that are present 583 iron atoms for each ferritin.

A) *Superimposition of SEC profile of the new EGFP-mFT purification (black line) and old purification (dashed grey line). Red lines indicate the fractions collected and used for DLS and ICP-OES analysis.* ***B)*** *Dynamic Light Scattering (DLS) of collected fractions of EGFP-mFT. The sample is mono dispersed with a radius of 9nm, compatible with the theoretical EGFP-mFT diameter of 16.8-20.4nm.* ***C)*** *ICP-OES analysis of EGFP-mFT. A calibration curve was built using 4 standards (black squares) with different iron concentrations. The same PBS used for the purification was measured as blank.* ***D)*** *Table of Fe concentrations (expressed in mg/L) for all the samples analyzed by ICP-OES. EGFP-mFT corrected for PBS has an iron concentration of 0.020mg/L. Protein concentration was used to calculate how many Fe atoms are present in each EGFP-mFT protein, which correspond to 583 atoms of iron in each ferritin.*

A novel approach to accurate temperature measurements

Another aspect of this study is the detection of putative temperature changes elicited by magnetic stimulation of ferritins (see Introduction, page 15). These changes are expected to be elicited by the iron core of the ferritins in response to oscillating magnetic fields. To analyze if ferritin generates

heat in response to magnetic field we decided to use the genetically encoded thermometer gTEMP protein (Nakano et al., 2017). The original gTEMP uses mT-Sapphire and Sirius fluorescent proteins, which changes their emission spectra in a temperature-dependent manner. However, our confocal microscope is not equipped with the correct laser/filter combination to efficiently visualize Sirius fluorescence. For this reason we decided to modify gTEMP using mCherry instead of Sirius, which shows a similar temperature dependence (Nakano et al., 2017), as reported in Figure 4A. Before creating and expresings the final construct in HEK cells, we decided to characterize first the temperature dependence of mT-Sapphire and mCherry purified proteins. Both proteins were cloned in a bacterial expression vector, containing a N-terminal histidine tag, expressed in *E. coli* and purified trough standard nickel column protocol. The SEC profile of nickel column eluate is shown in Figure 22A. Both proteins show a main peak around 16mL, and, in case of mT-Sapphire, the amount of protein is so high that the 280nm signal saturates. The central peak fractions were collected, and their protein content was quantified. To analyze proteins temperature dependence, equimolar amount of the two proteins were subjected to incremental temperature in a Real-Time PCR machine and fluorescence intensities were recorded during the measurement. Six individual replicates were made. Figure 22B shows the normalized fluorescence intensity at different temperature of mCherry (red) and mT-Sapphire (cyan). mT-Sapphire slightly increases its fluorescence, with a 24% increment from 10 to 50°C. This result is in contrast with the finding of (Nakano et al., 2017), which shows a small decrease of mT-Sapphire fluorescence at increasing temperature (Figure 4A). On the contrary, mCherry decreases its fluorescence of 43% from 10 to 50°C, accordingly to the previously published result (Nakano et al., 2017). We used the data of Figure 22B to calculate the ratio between mT-Sapphire and mCherry fluorescence changes with temperature (Figure 22C). The calculated ratios were fitted with an exponential curve, showing an increase from 1.0 to 2.2 passing from 10 to 50°C. The ratio is smaller compared to that of the original gTEMP construct, which in the same 10-50°C range, increases from 3.0 to 8.0.

We nevertheless test this system in HEK cells. We first created a construct containing mT-Sapphire and mCherry separated by a T2A sequence. The T2A site is a viral derived sequence of 18 amino-acid that, when inserted between two genes in the same plasmid, acts at the level of ribosome translation preventing the formation of a peptide bond between two amino-acid at the C-terminus of the T2A site (Donnelly et al., 2001). In this way is possible to produce two distinct proteins from only one coding sequence with a 1:1 ratio of the two proteins. We renamed this construct gTEMP2. gTEMP2 was expressed in HEK cells and mCherry and mT-Sapphire fluorescence emission was recorded at various temperature. The cells were first cooled down to 9°C and then heated up to 50°C. Temperature was monitored during the measurement using the same thermocouple described previously in TICK1 experiments. Images of 25 different cells in the same field were taken at 9, 24, 27.5, 29, 33 and 50°C. Figure 22D shows the mT-Sapphire/mCherry ratio of gTEMP2 expressing cells at various temperature. Black lines represent mean and standard deviation of each temperature. At the two extremes temperatures, the ratios are 0.89±0.1 at 9°C vs 1.58±0.23 at 50°C, not much different from those obtained with the purified proteins (1.0 and 2.2). Detection in the range 24°-33°C is not very accurate as the values tend to be similar: 24°C=1.19±0.21, 27.5°C=1.18±0.14, 29°C=1.12±0.15, 33°C=1.26±0.17. To better understand the reason of this, we

analyzed the level of mCherry and mT-Sapphire expression in cells transfected with gTEMP2. Figure 22E shows on the left the mCherry signal and on the right the mT-Sapphire signal of gTEMP2 expressing HEK cells. Theoretically, protein expression ratio should be 1:1 thanks to T2A sequence. In the lower image of Figure 22E we built a scatter plot of mCherry and mT-Sapphire fluorescent intensity of the upper images. In the lower left corner of the image, resembling the cells with low proteins expression, the signal is linear. Going to the upper right corner the signal starts to bifurcate, indicating that cells with higher protein expression tends to express preferentially one of the two proteins. For gTEMP2 working is essential to maintain a linear expression of the two proteins, otherwise the ratio of different cells cannot be compared, so this not uniform expression is probably the reason of gTEMP2-related problems that we have encountered. In conclusion, we still have to set a system that will allow us to detect temperature changes induced by oscillating MF in cells expressing ferritins. A possible alternative is to use an infrared camera connected to the microscope.

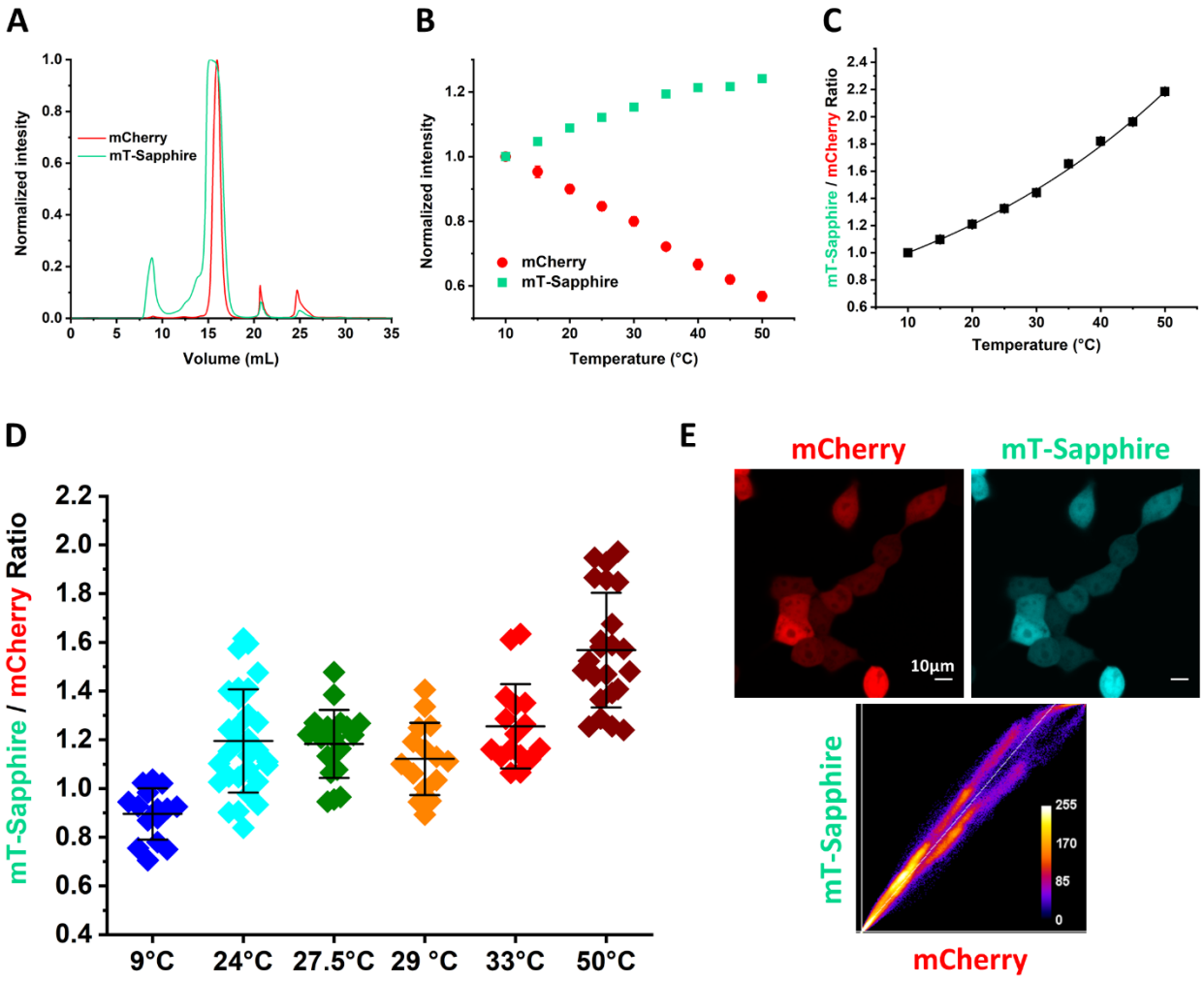

Figure 22: Characterization of a modified version of gTEMP.

A) *SEC profile of purified mCherry (red) and mT-Sapphire (cyan). Both proteins were expressed in E. coli and purified trough histidine tag/nickel resin interaction. The highest peak fractions were collected and used in the following in vitro tests.* ***B)*** *Equimolar amounts of purified mCherry (red) and mT-Sapphire (cyan) were separately heated from 10 to 50°C, with 5°C steps, and fluorescent intensity*

was recorded (mCherry Ex:580nm/Em:610nm; mT-Sapphire Ex:390nm/Em:520nm). Data are the average of 6 individual measurements. mT-Sapphire slightly increase its fluorescence at increasing temperature, while mCherry greatly decrease its fluorescence intensity. ***C)*** *Ratio of mT-Sapphire fluorescence over mCherry fluorescence at different temperature derived from the data obtained in (B). The line represents the exponential fitting of the points.* ***D)*** *mSapphire/mCherry fluorescence ratio of HEK cells expressing gTEMP2 construct (mT-Sapphire-T2A-mCherry) at different temperatures. Data are derived from 25 different cells of the same field first cooled down to 9°C and then heated at various temperature up to 50°C.* ***E)*** *Confocal images of mCherry and mT-Sapphire fluorescence of cells expressing gTEMP2. In the lower image was built a scatter-plot to compare the fluorescence intensity of the two proteins, that shows a non-homogenous expression ratio.*

Further steps towards MAGNETO: connecting the ferritin moiety to the TICK channel

Our working hypothesis is that an oscillating magnetic field produced by a moving permanent magnet and applied to the cells expressing both EGFP-mFT and TICK1, can induce a local increase in temperature in the iron core of the ferritin and that this, in turn, can trigger the opening of TICK1 (Figure 23A). Following the same rational of the magneto-genetic channel described by Stanley et al in 2015, we connected TICK1 to EGFP-mFT by means of a EGFP-nanobody (Kirchhofer et al., 2010). Nanobodies comprise the variable portion only of camelid antibody that are in turn formed by a single heavy chain only (Wesolowski et al., 2009). To ensure EGFP-ferritin interaction with TICK1, we added to the very N-terminus of TICK1 a nanobody developed against EGFP (EGFP-nanobody). Downstream of the nanobody we added a tagRFP for channel detection and renamed the construct nanoTICK1 (Figure 23A). Co-expression of nanoTICK1 with EGFP-mFT should result in the assembly of "Magnetic KCV" (MagKCV), a TICK1 channel that is covalently linked to EGFP-mFT. In principle each TICK1 monomer can capture one soluble EGFP-mFT and the EGFP-mFT can form a 12-mer by assembling with others endogenous ferritin present in HEK cells. Given the large dimension of the fully assembled EGFP-Ferritin (18nm, see Figure 21B) compared to that of the TICK1 tetramer ,Kcv_{NTS} has a maximum diameter of 5nm (obtained measuring residues distance of Kcv_{NTS} structural model reported in Rauh et al., 2018), we assume that each TICK1 channel can only be bound to one EGFP-Ferritin, if any. We have not proven the stoichiometry between TICK1 and ferritins yet as we needed to improve expression level of the construct first, see below. Nonetheless we believe that it should be possible to determine roughly the stoichiometry of the complex by F-SEC on detergent-solubilized cell extracts.

We have tested two different expression systems for MagKCV. In the first one, nanoTICK1 and EGFP-ferritin were delivered by separate plasmids co-transfected in HEK cells (Figure 23C), while in the second one the two gene sequences were cloned in the same plasmid, separated by a 2A self-cleaving peptide sequence (Figure 23D). Since nanoTICK1 assembles in a tetramer while EGFP-mFT is a 12mer, with the T2A system one EGFP-mFT is produced every 3 tetrameric nanoTICK1 channels. We have analyzed the localization of MagKCV in HEK cells comparing the expression obtained by co-transfection of the two components alone or together. Figure 23B shows that the fluorescent signal of nanoTICK1 alone has the same expression pattern of v1 (Figure 10B), indicating that the nanobody at the N terminus does not alter the localization of the channel. EGFP-mFT tends to form big fluorescent clusters inside the cells, as already observed (Figure 18A). When channel and ferritin are

transfected together either with the co-transfection system (Figure 23C) or with the T2A system (Figure 23D), the signal of EGFP-mFT still tends to assemble in clusters but they are smaller and distributed mostly at the cell surface. Furthermore, nanoTICK1 and EGFP-mFT perfectly co-localize, as demonstrated by the yellow signal present in the merge of green and red images (Figure 23C and Figure 23D bottom panels). For MagKCV expressed by T2A we have also added the same plasma membrane marker used previously, Cell Mask, to understand if some of the yellow signal co-localize with cell external membrane. In the left bottom panel of Figure 23D Cell Mask is shown in purple and few yellow spots are in proximity of purple signal, indicating that MagKCV is correctly assembled and reaches the plasma membrane.

HEK cells expressing MagKCV, either by co-transfection or T2A, were tested by patch clamp at 25°C or 50°C. The resulting dot-plot is shown in Figure 23E. MagKCV expressed by T2A shows that the channel is open in 1 cell among the 8 tested at 25°C, 12.5%, and in 3 over 5 cells at 50°C, 60%. The percentage of responding cells with TICK1 at 50°C is 52% (Figure 12B). The recorded current of the only cell with open MagKCV at 25°C is shown in the dashed black square of Figure 23E; for comparison, the recording of a 50°C responding cell is shown in the dashed red square and also I/V relationship of both cells are reported on the right panel. The cell with an open channel at 25°C has the same features of temperature responding cells indicating that MagKCV channels were already open at 25°C. The statistics is nonetheless quite low and data tend to indicate that the channel is controlled by temperature and is predominantly closed at 25°C, while it opens at 50°C. For the co-transfection system, no open MagKCV was found in the 6 tested cells at 25°C while it was open in 2 over 6 cells, 33.3%. In conclusion, in both cases we found a temperature-activated channel expressed at the PM. In principle the channel should be MagKCV but we cannot exclude the possibility that these currents are due to the presence of nanoTICK1 channels that are not connected to a fully assembled EGFP-FT. We decided to move on with the MagKCV construct expressed through the T2A system only, given the higher percentage of temperature responding cells, and to test if it responds to the magnetic fields.

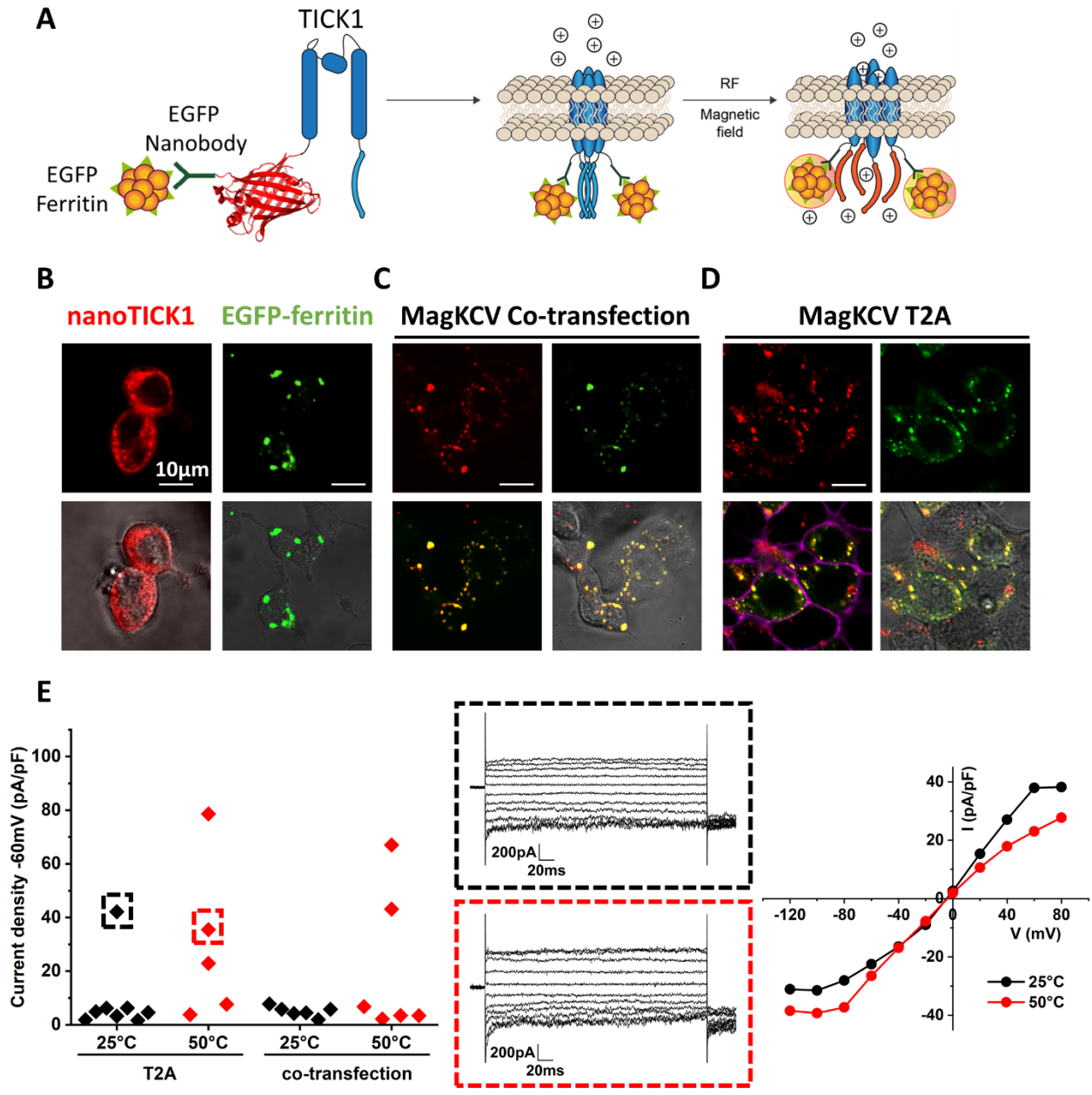

Figure 23: Design, localization and temperature sensitivity of "Magnetic KCV" (MagKCV).

A) *Structure and function of MagKCV. The left panel shows the cartoon representation of MagKCV monomer that includes: nanoTICK1, formed by TICK1 linked to the N terminal tagRFP and EGFP nanobody, and EGFP-mFT. MagKCV assemble as a tetramer and goes to the plasma membrane. For clarity, tagRFP is not shown in the tetrameric version and only two ferritin are shown coupled to the channel. When a magnetic field is applied, the local increase of temperature should trigger the opening of the channel.* ***B)*** *Confocal imaging showing the localization of the two components forming MagKCV (nanoTICK1 and EGFP-mFT) when expressed alone in HEK cells. Upper and lower panels show red or green fluorescent emission channels and fluorescent channel merged with brightfield, respectively.* ***C)*** *Confocal imaging of the co-transfection of the two components of MagKCV, shown separated (upper panels) and merged (lower panels, alone or superimposed to the brightfield image to show the cell contours).* ***D)*** *Confocal imaging of MagKCV expressed by one plasmid with a T2A sequence between KCV and Ferritin. Upper panels show red and green signals*

deriving from the two components of MagKCV. Lower panels show superimposition of the two signals without and with the bright filed image. The plasma membrane marker Cell Mask was added and is visible in purple in the lower left panel. ***E)*** *Dot-plot of -60mV current density of MagKCV expressed by T2A system at 25°C (mean current=8.8±4.8pA/pF, n=8) or 50°C (mean current=29.7±13.5pA/pF, n=5) compared with MagKCV expressed by co-transfection of nanoTICK1 and EGFP-mFT at 25°C (mean current=5.0±0.8pA/pF, n=6) or 50°C (mean current=21.0±11.2pA/pF, n=6). In the middle are shown the recordings of the only cell with open MagKCV-T2A at 25°C (black dashed square) and of the cell expressing the same construct at 50°C (red dashed square). On the right, the I/V relationship of these two cells is reported.*

Oscillating magnetic field can triggers the opening of MagKCV

As described in the introduction, a permanent magnet moving in the range of Hz is compatible with electrophysiology recordings (Stanley et al., 2016). More important, a moving magnet is needed for the magnetocaloric effect (Duret et al., 2019). Finally, this system was successfully used to triggers the opening of other magneto-genetic tools (Duret et al., 2019; Stanley et al., 2016; Wheeler et al., 2016). We have thus prepared an experimental setup in which a permanent magnet is moved manually back and forth over the sample at ca. 1Hz. The magnetic field oscillates between 50mT and 3mT. These intensities are in the same range of those reported by others, which varied from 32mT (Stanley et al., 2015) to 50mT (Wheeler et al., 2016). We conduct the experiment at 37°C. At this temperature TICK1 is closed and its requirement for activation is a small increase in temperature (2-3°C only). The experimental setup is shown in Figure 24A, a cartoon scheme on the top and a real picture on the bottom. A representative experiment of a cell expressing MagKCV is shown in Figure 24B. The current at -60mV was sampled every 5 second and the cell was kept at 37°C during the whole recording. Magnetic field stimulation (MF) was performed for 5 minutes as previously described. After an initial small decrease in current (at -60 mV the current values are negative), probably due to an improved pipette sealing to the membrane, the current gradually started to increase, after about 3 minutes of MF. In this case the increase of current continued for others 3 minutes without reaching a plateau. The total increase of current is of 10pA/pF, reaching a maximum current value of 14pA/pF. The experiment was terminated by adding 5mM $BaCl_2$ that blocked the current to the initial level. Current was also recorded with the usual voltage step protocol before MF (blue arrow), before barium addition (red arrow) and after barium addition (black arrow). The corresponding recordings are shown in Figure 24C, while the I/V relationships are presented in Figure 24D. The I/V curve show a typical Kcv current shape after the magnetic field treatment, with rectification either at high positive or negative voltages. Moreover, the effect of $BaCl_2$, suggests that the increase of current is due to MagKCV opening. The calculated reversal potential for K^+ with the solutions used in this experiment (130mM K^+ inside and 100mM K^+ outside) is -6mV, which is in fact the inversion potential of the I/V curve of 13B, strengthening the indication that the increase of current recorded during magnet exposure is related to a K^+ channel.

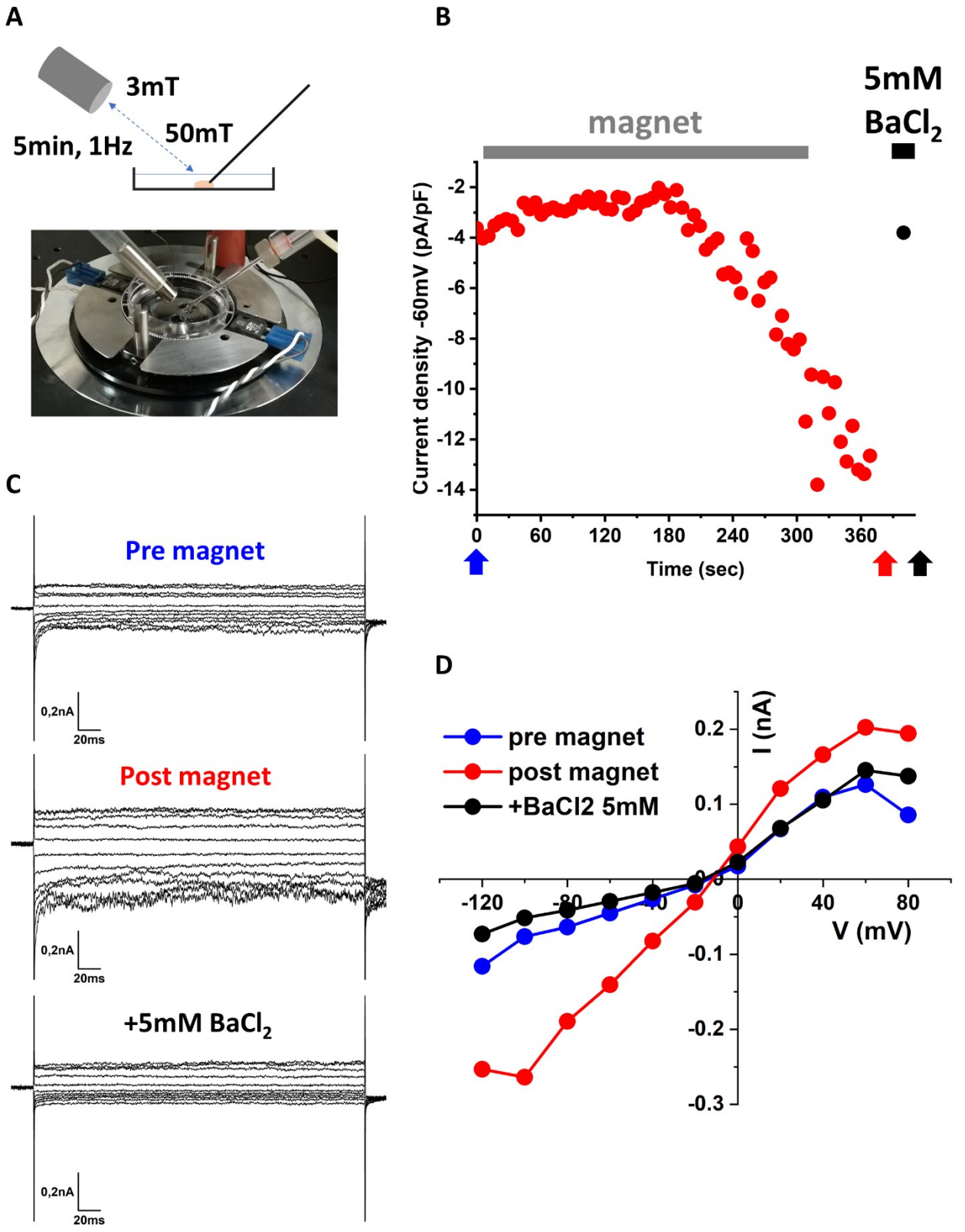

Figure 24: Activation of MagKCV through a moving permanent magnet.

A) *Experimental setup for the recording of HEK cells during the application of magnetic field. In the upper panel are shown in gray the permanent magnet, in black the petri dish and the glass capillary used for the electrical recording, in pink the tested HEK cell and in light blue the level of extracellular*

solution present in the petri. The permanent magnet is moved continuously at 1Hz for 5 minutes. In the closest position the measured magnetic field at the level of the cell is around 50mT while is around 3mT in the further position. In the lower panel an image of the setup is shown. The petri heating system was used to maintain the cells at 37°C. ***B)*** *Current recorded for 300ms every 5 second at -60mV of one representative cell expressing MagKCV. The cell was kept at 37°C during the whole measure and the magnet was applied at 1Hz for 5 minutes starting 10 second after the beginning of the recording. The increase of current starts around 3 minutes after magnet application, with a total increase of 10pA/pF. 5mM $BaCl_2$ was added at the end of the protocol.* ***C)*** *Recordings of the cell shown in (B) before the starting of magnetic field delivery (blue arrow), before barium addition (red arrow) and after 5mM $BaCl_2$ addition (black arrow).* ***D)*** *I/V relationship of the recordings shown in (C).*

20% of cells expressing MagKCV shows channel activation after MF

We have performed the same experiment in 46 cells in total. As controls, we have tested 40 cells expressing MagKcv recorded in the absence of MF, 10 cells expressing nanoTICK1, subjected to MF and 10 non-transfected cells not exposed to MF stimulation (the latter current values of non-transfected cells at 37°C, a condition that was never tested before). Figure 25 shows the dot-plot of the normalized current recorded at -60mV for individual cells of the above-mentioned experiments. In red are shown the currents of cells expressing MagKCV after 5 minutes of magnetic field exposure (mean current=5.7±1.0pA/pF, n=46). Usually, one cell was recorded during the MF stimulation and 3 or 4 cells on the same petri dish were tested after MF stimulation. Nine over 46 cells (19.6%) had a current value above the 10pA/pF threshold previously set for TICK1. In 3 of these cells the current increase was recorded during MF stimulation (one of these recordings is shown in Figure 24). In the absence of MF, out of 40 cells recorded, only one had a current above threshold (pink diamonds, n=40, mean current=4.9±0.6pA/pF) indicating that MagKCV is predominantly closed at 37°C. The inset (dashed black square) of Figure 25 shows the I/V relationship of the two cells indicated by the black arrows. In both cases the I/V shape resembles that of TICK1 and the current is efficiently abolished by barium addition.

The other controls, cells transfected with nanoTICK1 exposed to magnetic field (green diamonds, n=10, mean current=2.9±0.3pA/pF) or non- transfected cells not exposed to magnetic field (gray diamonds, n=11, mean current=3.3±0.4pA/pF), always showed basal (endogenous) current levels. A one-way ANOVA test was performed between all these samples, but no statistically significative difference was found. This is probably related to the low number of tested cells responding to the magnet with a MagKCV activation.

In conclusion, our preliminary experiments with the magnetic fields indicate that about 20% (19.6%) of MagKCV-expressing cells respond to MF. The fact that not all the cells are activated by magnetic field could be due to several factors. First, also not all the cells expressing TICK1 respond to the temperature increase (about 52%, see Figure 12B). This % is conserved in MagKCV, where we found that about 60% of cells responded to temperature (Figure 23E), however this are a very preliminary data because of the low number of tested cells. Second, the percentage of responding cells increases with increasing temperature (Figure 12B) and it is possible that the rise of temperature induced by the MF, if any, is small; it may not exceed the threshold for activation of TICK1 and therefore of

MagKCV. Third, the addition of ferritin to nanoTICK1 could affect its trafficking, reducing the amount of channels that reaches the plasma membrane. This can lead to subthreshold responses in our experiments. Another aspect that must be taken in account is that in 1 out of 40 cells (i.e., 2.5%) MagKCV channels were already open channel at 37°C. This never occurred with TICK1 and indicates that MagKCV might be slightly less regulated than TICK1. Increasing the statistics is therefore mandatory.

Nevertheless, the fact that about 19.6% cells, even though with varying degrees of intensities, were affected by the magnetic fields makes MagKCV a promising starting point to develop a magneto-genetic K^+ tool.

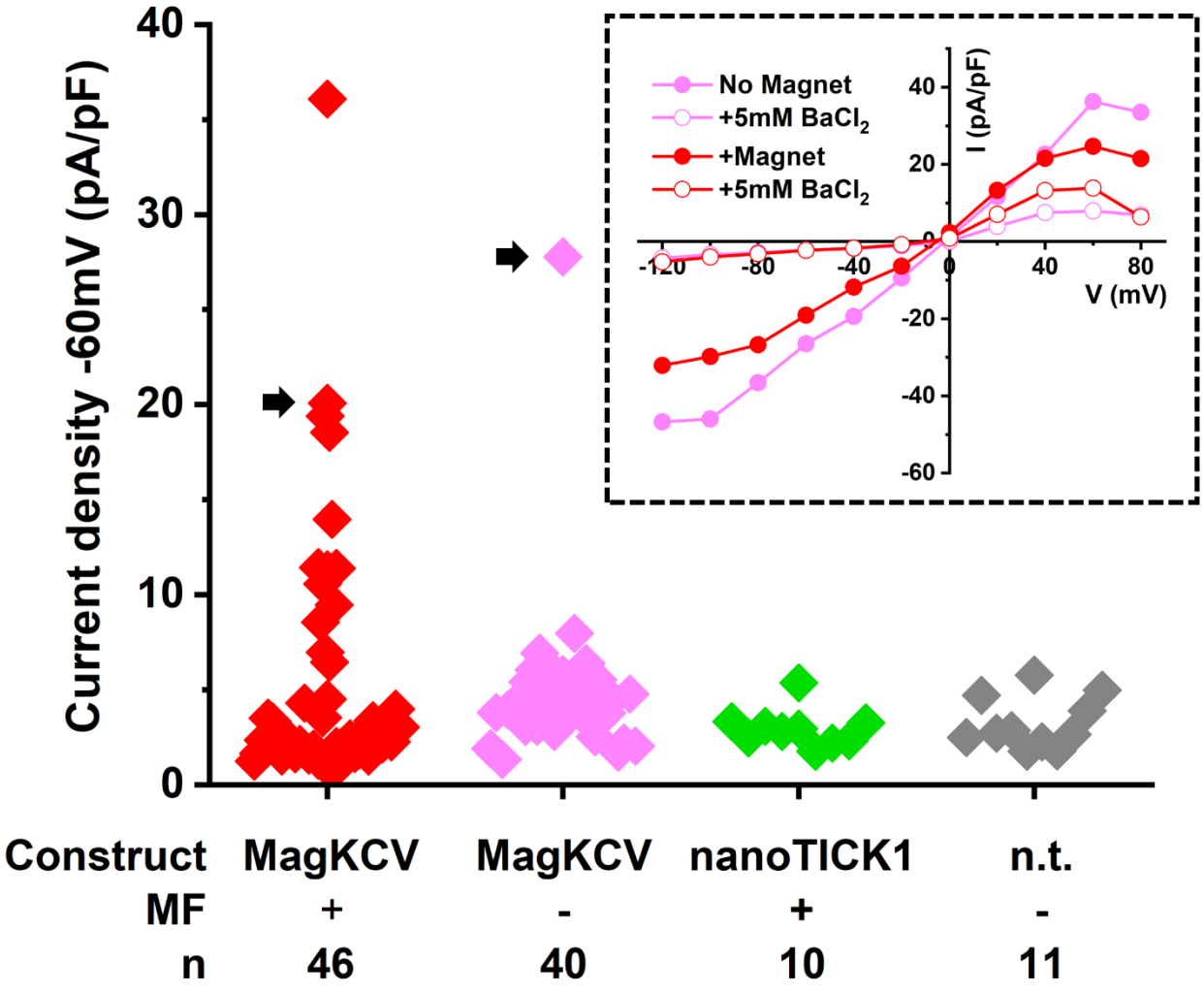

Figure 25: Cells expressing MagKCV subjected to MF shows higher percentage of channel activation.

Dot plot graph of cells expressing MagKCV treated with MF (mean current=5.7±1.0pA/pF, n=46) or without MF (mean current=4.9±0.6pA/pF, n=40), expressing nanoTICK1 subjected to MF (mean current=2.9±0.3pA/pF, n=10) or not transfected cells not subjected to MF (mean current=3.2±0.4pA/pF, n=11). Cells were kept at 37°C in all conditions while MF consists in 1Hz, 50mT for 5 minutes as described in Figure 24A. Dashed black square inset shows I/V relationship of cells

indicated by the black arrows, before and after 5mM $BaCl_2$ addition. Cells with current over 10pA/pF are 9/46 for MagKCV +MF (19.6%) and 1/40 for MagKCV -MF (2.5%).

Further experiments are required to assess the magnetic activation of MagKCV

The data shown in the paragraphs above are a preliminary indication that a 50mT/1Hz oscillating magnetic field is enhancing the percentage of cells with an open MagKCV, from 2.5 to 19.6%.

Unfortunately, the attempt to repeat this data after almost one year did not produce the same effect reported in this thesis. Further investigation will be necessary to understand the reason of this inconsistent result. Moreover, additional controls are necessary to validate the magnetic activation of MagKCV. It would be necessary to standardize the experimental procedure, avoiding the testing of several cells in the same petri dish. In this way only real-time effect would be recorded, as the one described in Figure *24*, making the results more comparable. Moreover, a greater statistic should be reached for the cells expressing nanoTICK1 subjected to MF, to exclude any ferritin independent magnetic activation of the channel. Also, untransfected cells should be tested with MF, to exclude aspecific effects. The finding that in some cells, either at 25 or 37°C, MagKCV is open without any MF stimulation must be better analyzed. During TICK1 mutants selection several construct were discarded because they have shown cells with an open channel at temperature ≤37°C, making them unsuitable for mammals expression. Further optimization of MagKCV is thus necessary.

Conclusions

Magneto-genetics has the potentiality to revolutionize neurobiology, as much as optogenetics did more than 10 years ago. The harmless nature and the efficient tissue penetration of magnetic fields make these tools ideals for pathology treatment. In this context, it is essential to understand building principles of these tools in order to expand the toolbox, so far limited to TRPV channels. Here we successfully built a first prototype of a magneto-genetic potassium channel.

MagKCV activates only in 20% of tested cells (Figure 25), a percentage that is encouraging but still suboptimal. Its progenitor TICK1 opens in 52% of tested cells (Figure 12B) and shows suboptimal membrane expression (Figure 14). Thus, improving TICK1 surface expression could presumably positively affects MagKCV membrane trafficking and consequently its activation. This is a rather common problem in protein engineering. We believe that this will be successfully improved, also in the case of MagKCV, by following successful strategies reported in literature. In the case of the magneto-genetic tool "Magneto", the percentage of responding cells, around 17%, was increased to 58% with the addition of a plasma membrane trafficking signal (Wheeler et al., 2016). This improvement was obtained following the same rational used for the optogenetic tool NpHR, in which addition of several trafficking motif dramatically improved the plasma membrane expression (Gradinaru et al., 2010). Also the Kcv based optogenetic tool BLINK1 had a trafficking problem (Cosentino et al., 2015), which was mitigated by the addition of binding site for 14-3-3 proteins (Alberio et al., 2018), a class of adaptors that controls surface expression of eukaryotic channels (Saponaro et al., 2017). All the above-mentioned trafficking improvements were obtained by the addition of C-terminal sequences. The C-terminal of TICK1 is the region controlling the temperature sensitivity of the channel, and we demonstrated that single point mutations in this region are enough to affect channel's temperature dependence (Figure 12 and Figure 13). It is therefore important to carefully consider any modification of the C-terminus of TICK1. An alternative could be the introduction of N-terminal trafficking signals, like the ER export signal identified in HCN1, which is necessary for plasma membrane localization of the channel in photoreceptors (Pan et al., 2015).

On the other hand, it could be useful to enhance the local heat generated by the ferritin when exposed to magnetic field. Even if it was indirectly demonstrated in other magneto-genetic tools that a temperature rise is the mechanism at the base of activation (Duret et al., 2019), still the heat generated by the ferritin was never directly measured. Our attempts with the genetically encoded thermometer gTEMP (Nakano et al., 2017) failed probably due to the non-homogenous expression of mCherry and mT-Sapphire in HEK cells (Figure 22). An alternative system would be the use of a high-resolution infrared camera mounted on the confocal microscope. An interesting option could also be L-DNA molecular beacons (L-MBs), which were efficiently used to measure temperature changes in living cells (Ke et al., 2012). These consist in a nucleotide hairpin sequence, with a fluorophore and a quencher at the two opposite ends of the molecule. These two are maintained in close proximity at low temperatures; when temperature increases, the progressive melting of L-MBs, which passes from a double strand to a single strand configuration, moves away the quencher from the fluorophore leading to fluorescence increase (Ke et al., 2012). This method could allow the measurement of local ferritin-induced temperature rise.

In order to strengthen the magnetocaloric effect of ferritins, we will also try to enhance the iron content of EGFP-mFT. We have already proved that ferritins formed by EGFP-mFT contain in average 583 iron atoms/ferritin (Figure 21). This value is in agreement with that reported for endogenous ferritins (Salgado et al., 2010), but it is much lower from the maximum iron loading capacity of ferritins, that is around 4500 iron atoms (Arosio et al., 2017). To increase iron uptake, a possible strategy is to co-express in cells a specific iron transporter (Kim et al., 2012). Another possible approach is *in vitro* evolution of ferritin, to increase the iron uptake capacity. This last approach was used for *Escherichia coli* (Liu et al., 2016) and *Pyrococcus furiosus* (Matsumoto et al., 2015) ferritin, leading to the identification of single point mutations that increases ferritin iron uptake activity. Given the high degree of ferritin conservation among different organisms, it could be interesting to test if these mutations identified in Bacteria and Archea can improve also our eukaryotic construct.

Finally, the joining between ferritin and TICK1 in MagKCV should be further optimized. In the present construct, their interaction is indirectly mediated by binding of a nanobody to EGFP, introducing a distance between the channel and the ferritin that can disperse heat. In order to reduce this distance, an alternative approach could be to attach at the N terminal of TICK a nanobody for the endogenous ferritins. This strategy does not require the co-transfection with the engineered ferritins, reducing the risk to form toxic aggregates in the cell. Moreover, preventing ferritin overexpression may increase the iron content of endogenous ferritins. Finally, in the view of a gene therapy based on AAV, the construct will be shorter and thus compatible with the size requirement of this viral vector. Another approach reported in literature is the connection of endogenous ferritin to TRPV1 and TRPV4 C-terminus through the ferritin binding domain of kininogen-1 (Hutson et al., 2017).

One of the aims of this thesis was also to confirm the temperature induced pathway of magneto-genetic tools activation. For this, TICK1 was specifically designed to be regulated only by temperature. However, to convincingly demonstrate that MagKCV magnetic-field gating is temperature dependent, further control experiments are needed. At the moment, we do not have a system to abolish TICK1 temperature sensitivity. Moreover, mutations that disrupt K^+ channels conductance, which were identified in Shaker channel (Heginbotham et al., 1994; Perozo et al., 1993), KcsA channel (Splitt et al., 2000), PBCV-1 Kcv (Tan et al., 2010) or in Kcv_{NTS} (Rauh et al., data not published), would not be useful since these would prevent any activation pathway of MagKCV. A possibility is to remove M267A mutation in MagKCV and restore the original v1 construct, which temperature activation occurs over 45°C. In addition, instead of maintaining cells at 37°C during magnetic field exposure, we could leave them at room temperature, increasing the heat necessary to activate the channel. If MagKCV magnetic field activation would not occurs in this condition, we could conclude that temperature is the mechanism behind MagKCV magnetic gating.

Establishing the mechanism for magnetic activation, at least in this family of temperature-dependent channels, will positively contribute to establish magneto-genetics principles of operation and will promote further this technique as a valid alternative to optogenetics.

Bibliography

Alberio, L., Locarno, A., Saponaro, A., Romano, E., Bercier, V., Albadri, S., Simeoni, F., Moleri, S., Pelucchi, S., Porro, A., Marcello, E., Barsotti, N., Kukovetz, K., Boender, A. J., Contestabile, A., Luo, S., Moutal, A., Ji, Y., Romani, G., … Moroni, A. (2018). A light-gated potassium channel for sustained neuronal inhibition. *Nature Methods*, *15*(11), 969–976. https://doi.org/10.1038/s41592-018-0186-9

Alvarez, O., Gonzalez, C., & Latorre, R. (2002). Counting channels: A tutorial guide on ion channel fluctuation analysis. *American Journal of Physiology - Advances in Physiology Education*, *26*(1–4), 327–341. https://doi.org/10.1152/advan.00006.2002

Arenkiel, B. R., Peca, J., Davison, I. G., Feliciano, C., Deisseroth, K., Augustine, G. J. J., Ehlers, M. D., & Feng, G. (2007). In Vivo Light-Induced Activation of Neural Circuitry in Transgenic Mice Expressing Channelrhodopsin-2. *Neuron*, *54*(2), 205–218. https://doi.org/10.1016/j.neuron.2007.03.005

Arosio, P., Carmona, F., Gozzelino, R., Maccarinelli, F., & Poli, M. (2015). The importance of eukaryotic ferritins in iron handling and cytoprotection. *Biochemical Journal*, *472*(1), 1–15. https://doi.org/10.1042/BJ20150787

Arosio, P., Elia, L., & Poli, M. (2017). Ferritin, cellular iron storage and regulation. *IUBMB Life*, *69*(6), 414–422. https://doi.org/10.1002/iub.1621

Arrigoni, C., Rohaim, A., Shaya, D., Findeisen, F., Stein, R. A., Nurva, S. R., Mishra, S., McHaourab, H. S., & Minor, D. L. (2016). Unfolding of a Temperature-Sensitive Domain Controls Voltage-Gated Channel Activation. *Cell*, *164*(5), 922–936. https://doi.org/10.1016/j.cell.2016.02.001

Arrigoni, C., Schroeder, I., Romani, G., Etten, V., Thiel, G., & Moroni, A. (2013). The voltage-sensing domain of a phosphatase gates the pore of a potassium channel. *Journal of General Physiology*, *141*(3), 389–395. https://doi.org/10.1085/jgp.201210940

Banghart, M., Borges, K., Isacoff, E., Trauner, D., & Kramer, R. H. (2004). Light-activated ion channels for remote control of neuronal firing. *Nature Neuroscience*, *7*(12), 1381–1386. https://doi.org/10.1038/nn1356

Barbic, M. (2019). Possible magneto-mechanical and magneto-thermal mechanisms of ion channel activation in magnetogenetics. *ELife*, *8*, 1–18. https://doi.org/10.7554/eLife.45807

Ben-Ari, Y. (2002). Excitatory actions of GABA during development: The nature of the nurture. *Nature Reviews Neuroscience*, *3*(9), 728–739. https://doi.org/10.1038/nrn920

Bezrukov, L., Blank, P. S., Polozov, I. V., & Zimmerberg, J. (2009). An adhesion-based method for plasma membrane isolation: Evaluating cholesterol extraction from cells and their membranes. *Analytical Biochemistry*, *394*(2), 171–176. https://doi.org/10.1016/j.ab.2009.07.027

Bi, A., Cui, J., Ma, Y. P., Olshevskaya, E., Pu, M., Dizhoor, A. M., & Pan, Z. H. (2006). Ectopic Expression of a Microbial-Type Rhodopsin Restores Visual Responses in Mice with Photoreceptor Degeneration. *Neuron*, *50*(1), 23–33.

https://doi.org/10.1016/j.neuron.2006.02.026

Boyden, E. S., Zhang, F., Bamberg, E., Nagel, G., & Deisseroth, K. (2005). Millisecond-timescale, genetically targeted optical control of neural activity. *Nature Neuroscience*, *8*(9), 1263–1268. https://doi.org/10.1038/nn1525

Braun, C. J., Lachnit, C., Becker, P., Henkes, L. M., Arrigoni, C., Kast, S. M., Moroni, A., Thiel, G., & Schroeder, I. (2014). Viral potassium channels as a robust model system for studies of membrane-protein interaction. *Biochimica et Biophysica Acta - Biomembranes*, *1838*(4), 1096–1103. https://doi.org/10.1016/j.bbamem.2013.06.010

Brier, M. I., Mundell, J. W., Yu, X., Su, L., Holmann, A., Squeri, J., Zhang, B., Stanley, S. A., Friedman, J. M., & Dordick, J. S. (2020). Uncovering a possible role of reactive oxygen species in magnetogenetics. *Scientific Reports*, *10*(1), 1–13. https://doi.org/10.1038/s41598-020-70067-1

Chen, J. T. C., Guo, D., Campanelli, D., Frattini, F., Mayer, F., Zhou, L., Kuner, R., Heppenstall, P. A., Knipper, M., & Hu, J. (2014). Presynaptic GABAergic inhibition regulated by BDNF contributes to neuropathic pain induction. *Nature Communications*, *5*. https://doi.org/10.1038/ncomms6331

Chen, R., Romero, G., Christiansen, M. G., Mohr, A., & Anikeeva, P. (2015). Wireless magnetothermal deep brain stimulation. *Science*, *347*(6229), 1477–1480. https://doi.org/10.1126/science.1261821

Chow, B. Y., Han, X., Dobry, A. S., Qian, X., Chuong, A. S., Li, M., Henninger, M. A., Belfort, G. M., Lin, Y., Monahan, P. E., & Boyden, E. S. (2010). High-performance genetically targetable optical neural silencing by light-driven proton pumps. *Nature*, *463*(7277), 98–102. https://doi.org/10.1038/nature08652

Colloca, L., Ludman, T., Bouhassira, D., Baron, R., Dickenson, A. H., Yarnitsky, D., Freeman, R., Truini, A., Attal, N., Finnerup, N. B., Eccleston, C., Kalso, E., Bennett, D. L., Dworkin, R. H., & Raja, S. N. (2017). Neuropathic pain. *Nature Reviews Disease Primers*, *3*, 1–20. https://doi.org/10.1038/nrdp.2017.2

Cosentino, C., Alberio, L., Gazzarrini, S., Aquila, M., Romano, E., Cermenati, S., Zuccolini, P., Petersen, J., Beltrame, M., Van Etten, J. L., Christie, J. M., Thiel, G., & Moroni, A. (2015). Engineering of a light-gated potassium channel. *Science*, *348*(6235), 707–710. https://doi.org/10.1126/science.aaa2787

DiFrancesco, M. L., Gazzarrini, S., Arrigoni, C., Romani, G., Thiel, G., & Moroni, A. (2015). Engineering a Ca++-sensitive (Bio)sensor from the pore-module of a potassium channel. *Sensors (Switzerland)*, *15*(3), 4913–4924. https://doi.org/10.3390/s150304913

Donnelly, M. L. L., Luke, G., Mehrotra, A., Li, X., Hughes, L. E., Gani, D., & Ryan, M. D. (2001). *Analysis of the aphthovirus 2A / 2B polyprotein ' cleavage ' mechanism indicates not a proteolytic reaction , but a novel translational effect : a putative ribosomal ' skip .'* 1013–1025.

Duret, G., Polali, S., Anderson, E. D., Bell, A. M., Tzouanas, C. N., Avants, B. W., & Robinson, J. T.

(2019). Magnetic Entropy as a Proposed Gating Mechanism for Magnetogenetic Ion Channels. *Biophysical Journal*, *116*(3), 454–468. https://doi.org/10.1016/j.bpj.2019.01.003

Fenno, L., Yizhar, O., & Deisseroth, K. (2011). The Development and Application of Optogenetics. *Annual Review of Neuroscience*, *34*(1), 389–412. https://doi.org/10.1146/annurev-neuro-061010-113817

Flotte, T. R. (2000). Size does matter: Overcoming the adeno-associated virus packaging limit. *Respiratory Research*, *1*(1), 16–18. https://doi.org/10.1186/rr6

Fortin, D. L., Dunn, T. W., Fedorchak, A., Allen, D., Montpeti, R., Banghart, M. R., Trauner, D., Adelman, J. P., & Kramer, R. H. (2011). Optogenetic photochemical control of designer K+ channels in mammalian neurons. *Journal of Neurophysiology*, *106*(1), 488–496. https://doi.org/10.1152/jn.00251.2011

Fortin, J. P., Gazeau, F., & Wilhelm, C. (2008). Intracellular heating of living cells through Néel relaxation of magnetic nanoparticles. *European Biophysics Journal*, *37*(2), 223–228. https://doi.org/10.1007/s00249-007-0197-4

Franco, V., Blázquez, J. S., Ingale, B., & Conde, A. (2012). The magnetocaloric effect and magnetic refrigeration near room temperature: Materials and models. In *Annual Review of Materials Research* (Vol. 42, pp. 305–342). https://doi.org/10.1146/annurev-matsci-062910-100356

Gazzarrini, S., Kang, M., Abenavoli, A., Romani, G., Olivari, C., Gaslini, D., Ferrara, G., Van Etten, J. L., Kreim, M., Kast, S. M., Thiel, G., & Moroni, A. (2009). Chlorella virus ATCV-1 encodes a functional potassium channel of 82 amino acids. *Biochemical Journal*, *420*(2), 295–303. https://doi.org/10.1042/BJ20090095

Gazzarrini, S., Severino, M., Lombardi, M., Morandi, M., DiFrancesco, D., Van Etten, J. L., Thiel, G., & Moroni, A. (2003). The viral potassium channel Kcv: Structural and functional features. *FEBS Letters*, *552*(1), 12–16. https://doi.org/10.1016/S0014-5793(03)00777-4

Gibson, D. G., Young, L., Chuang, R. Y., Venter, J. C., Hutchison, C. A., & Smith, H. O. (2009). Enzymatic assembly of DNA molecules up to several hundred kilobases. *Nature Methods*, *6*(5), 343–345. https://doi.org/10.1038/nmeth.1318

Gradinaru, V., Zhang, F., Ramakrishnan, C., Mattis, J., Prakash, R., Diester, I., Goshen, I., Thompson, K. R., & Deisseroth, K. (2010). Molecular and Cellular Approaches for Diversifying and Extending Optogenetics. *Cell*, *141*(1), 154–165. https://doi.org/10.1016/j.cell.2010.02.037

Grandl, J., Kim, S. E., Uzzell, V., Bursulaya, B., Petrus, M., Bandell, M., & Patapoutian, A. (2010). Temperature-induced opening of TRPV1 ion channel is stabilized by the pore domain. *Nature Neuroscience*, *13*(6), 708–714. https://doi.org/10.1038/nn.2552

Greiner, T. (2011). *Characterization of novel potassium transport proteins from Chlorella viruses*. 1–115. http://tuprints.ulb.tu-darmstadt.de/2685/

Heginbotham, L., Lu, Z., Abramson, T., & MacKinnon, R. (1994). Mutations in the K+ channel signature sequence. *Biophysical Journal*, *66*(4), 1061–1067. https://doi.org/10.1016/S0006-3495(94)80887-2

Hernández-Morales, M., Shang, T., Chen, J., Han, V., & Liu, C. (2020). Lipid Oxidation Induced by RF Waves and Mediated by Ferritin Iron Causes Activation of Ferritin-Tagged Ion Channels. *Cell Reports*, *30*(10), 3250-3260.e7. https://doi.org/10.1016/j.celrep.2020.02.070

Hink, M. A., Griep, R. A., Borst, J. W., Van Hoek, A., Eppink, M. H. M., Schots, A., & Visser, A. J. W. G. (2000). Structural dynamics of green fluorescent protein alone and fused with a single chain Fv protein. *Journal of Biological Chemistry*, *275*(23), 17556–17560. https://doi.org/10.1074/jbc.M001348200

Honoré, E. (2007). The neuronal background K2P channels: Focus on TREK1. *Nature Reviews Neuroscience*, *8*(4), 251–261. https://doi.org/10.1038/nrn2117

Huang, H., Delikanli, S., Zeng, H., Ferkey, D. M., & Pralle, A. (2010). Remote control of ion channels and neurons through magnetic-field heating of nanoparticles. *Nature Nanotechnology*, *5*(8), 602–606. https://doi.org/10.1038/nnano.2010.125

Hutson, M. R., Keyte, A. L., Hernández-Morales, M., Gibbs, E., Kupchinsky, Z. A., Argyridis, I., Erwin, K. N., Pegram, K., Kneifel, M., Rosenberg, P. B., Matak, P., Xie, L., Grandl, J., Davis, E. E., Katsanis, N., Liu, C., & Benner, E. J. (2017). Temperature-activated ion channels in neural crest cells confer maternal fever-associated birth defects. *Science Signaling*, *10*(500), 1–17. https://doi.org/10.1126/scisignal.aal4055

Iordanova, B., Robison, C. S., & Ahrens, E. T. (2010). Design and characterization of a chimeric ferritin with enhanced iron loading and transverse NMR relaxation rate. *Journal of Biological Inorganic Chemistry*, *15*(6), 957–965. https://doi.org/10.1007/s00775-010-0657-7

Janovjak, H., Szobota, S., Wyart, C., Trauner, D., & Isacoff, E. Y. (2010). A light-gated, potassium-selective glutamate receptor for the optical inhibition of neuronal firing. *Nature Neuroscience*, *13*(8), 1027–1032. https://doi.org/10.1038/nn.2589

Jian, N., Dowle, M., Horniblow, R. D., Tselepis, C., & Palmer, R. E. (2016). Morphology of the ferritin iron core by aberration corrected scanning transmission electron microscopy. *Nanotechnology*, *27*(46). https://doi.org/10.1088/0957-4484/27/46/46LT02

Kaneko, H., Putzier, I., Frings, S., Kaupp, U. B., & Gensch, T. (2004). Chloride accumulation in mammalian olfactory sensory neurons. *Journal of Neuroscience*, *24*(36), 7931–7938. https://doi.org/10.1523/JNEUROSCI.2115-04.2004

Kang, J. Y., Kawaguchi, D., Coin, I., Xiang, Z., O'Leary, D. D. M., Slesinger, P. A., & Wang, L. (2013). In vivo expression of a light-activatable potassium channel using unnatural amino acids. *Neuron*, *80*(2), 358–370. https://doi.org/10.1016/j.neuron.2013.08.016

Ke, G., Wang, C., Ge, Y., Zheng, N., Zhu, Z., & Yang, C. J. (2012). L -DNA molecular beacon: A safe, stable, and accurate intracellular nano-thermometer for temperature sensing in living cells. *Journal of the American Chemical Society*, *134*(46), 18908–18911. https://doi.org/10.1021/ja3082439

Kim, T., Moore, D., & Fussenegger, M. (2012). Genetically programmed superparamagnetic behavior of mammalian cells. *Journal of Biotechnology*, *162*(2–3), 237–245. https://doi.org/10.1016/j.jbiotec.2012.09.019

Kirchhofer, A., Helma, J., Schmidthals, K., Frauer, C., Cui, S., Karcher, A., Pellis, M., Muyldermans, S., Casas-Delucchi, C. S., Cardoso, M. C., Leonhardt, H., Hopfner, K. P., & Rothbauer, U. (2010). Modulation of protein properties in living cells using nanobodies. *Nature Structural and Molecular Biology*, *17*(1), 133–139. https://doi.org/10.1038/nsmb.1727

Lang, B. J., Guerrero, M. E., Prince, T. L., Okusha, Y., Bonorino, C., & Calderwood, S. K. (2021). The functions and regulation of heat shock proteins; key orchestrators of proteostasis and the heat shock response. *Archives of Toxicology*, *95*(6), 1943–1970. https://doi.org/10.1007/s00204-021-03070-8

Liu, X., Lopez, P. A., Giessen, T. W., Giles, M., Way, J. C., & Silver, P. A. (2016). Engineering Genetically-Encoded Mineralization and Magnetism via Directed Evolution. *Scientific Reports*, *6*(October), 1–10. https://doi.org/10.1038/srep38019

Luscieti, S., Santambrogio, P., D'Estaintot, B. L., Granier, T., Cozzi, A., Poli, M., Gallois, B., Finazzi, D., Cattaneo, A., Levi, S., & Arosio, P. (2010). Mutant ferritin L-chains that cause neurodegeneration act in a dominant-negative manner to reduce ferritin iron incorporation. *Journal of Biological Chemistry*, *285*(16), 11948–11957. https://doi.org/10.1074/jbc.M109.096404

Mahn, M., Prigge, M., Ron, S., Levy, R., & Yizhar, O. (2016). Biophysical constraints of optogenetic inhibition at presynaptic terminals. *Nature Neuroscience*, *19*(4), 554–556. https://doi.org/10.1038/nn.4266

Matsumoto, Y., Chen, R., Anikeeva, P., & Jasanoff, A. (2015). Engineering intracellular biomineralization and biosensing by a magnetic protein. *Nature Communications*, *6*, 1–10. https://doi.org/10.1038/ncomms9721

Meister, M. (2016). Physical limits to magnetogenetics. *ELife*, *5*(AUGUST), 1–14. https://doi.org/10.7554/eLife.17210

Nakano, M., Arai, Y., Kotera, I., Okabe, K., Kamei, Y., & Nagai, T. (2017). Genetically encoded ratiometric fluorescent thermometer with wide range and rapid response. *PLoS ONE*, *12*(2), 1–14. https://doi.org/10.1371/journal.pone.0172344

Nimpf, S., & Keays, D. A. (2017). Is magnetogenetics the new optogenetics? *The EMBO Journal*, *36*(12), 1643–1646. https://doi.org/10.15252/embj.201797177

Nogueron, I. (1988). Intracellular Chloride Regulation in Amphibian Dorsal. *Physiology*, *c*, 225–246.

Pan, Y., Laird, J. G., Yamaguchi, D. M., & Baker, S. A. (2015). An N-terminal ER export signal facilitates the plasma membrane targeting of HCN1 channels in photoreceptors. *Investigative Ophthalmology and Visual Science*, *56*(6), 3514–3521. https://doi.org/10.1167/iovs.15-16902

Patapoutian, A., Peier, A. M., Story, G. M., & Viswanath, V. (2003). Thermotrp channels and beyond: Mechanisms of temperature sensation. *Nature Reviews Neuroscience*, *4*(7), 529–539. https://doi.org/10.1038/nrn1141

Perozo, E., MacKinnon, R., Bezanilla, F., & Stefani, E. (1993). Gating currents from a nonconducting mutant reveal open-closed conformations in Shaker K+ channels. *Neuron*, *11*(2), 353–358.

https://doi.org/10.1016/0896-6273(93)90190-3

Plugge, B., Gazzarrini, S., Nelson, M., Cerana, R., Van Etten, J. L., Derst, C., DiFrancesco, D., Moroni, A., & Thiel, G. (2000). A potassium channel protein encoded by chlorella virus PBCV-1. *Science*, *287*(5458), 1641–1644. https://doi.org/10.1126/science.287.5458.1641

Qin, S., Yin, H., Yang, C., Dou, Y., Liu, Z., Zhang, P., Yu, H., Huang, Y., Feng, J., Hao, J., Hao, J., Deng, L., Yan, X., Dong, X., Zhao, Z., Jiang, T., Wang, H. W., Luo, S. J., & Xie, C. (2016). A magnetic protein biocompass. *Nature Materials*, *15*(2), 217–226. https://doi.org/10.1038/nmat4484

Radu, I., Bamann, C., Nack, M., Nagel, G., Bamberg, E., & Heberle, J. (2009). Conformational changes of channelrhodopsin-2. *Journal of the American Chemical Society*, *131*(21), 7313–7319. https://doi.org/10.1021/ja8084274

Rauh, O., Urban, M., Henkes, L. M., Winterstein, T., Greiner, T., Van Etten, J. L., Moroni, A., Kast, S. M., Thiel, G., & Schroeder, I. (2017). Identification of Intrahelical Bifurcated H-Bonds as a New Type of Gate in K+ Channels. *Journal of the American Chemical Society*, *139*(22), 7494–7503. https://doi.org/10.1021/jacs.7b01158

Rojas, A., Wu, J., Wang, R., & Jiang, C. (2007). Gating of the ATP-sensitive K+ channel by a pore-lining phenylalanine residue. *Biochimica et Biophysica Acta - Biomembranes*, *1768*(1), 39–51. https://doi.org/10.1016/j.bbamem.2006.06.027

Rossow, M. J., Sasaki, J. M., Digman, M. A., & Gratton, E. (2010). Raster image correlation spectroscopy in live cells. *Nature Protocols*, *5*(11), 1761–1774. https://doi.org/10.1038/nprot.2010.122

Sahel, J.-A., Boulanger-Scemama, E., Pagot, C., Arleo, A., Galluppi, F., Martel, J. N., Esposti, S. D., Delaux, A., de Saint Aubert, J.-B., de Montleau, C., Gutman, E., Audo, I., Duebel, J., Picaud, S., Dalkara, D., Blouin, L., Taiel, M., & Roska, B. (2021). Partial recovery of visual function in a blind patient after optogenetic therapy. *Nature Medicine*. https://doi.org/10.1038/s41591-021-01351-4

Saiz-Baggetto, S., Méndez, E., Quilis, I., Igual, J. C., & Bañó, M. C. (2017). Chimeric proteins tagged with specific 3xHA cassettes may present instability and functional problems. *PLOS ONE*, *12*(8), e0183067. https://doi.org/10.1371/JOURNAL.PONE.0183067

Salgado, J. C., Olivera-Nappa, A., Gerdtzen, Z. P., Tapia, V., Theil, E. C., Conca, C., & Nuñez, M. T. (2010). Mathematical modeling of the dynamic storage of iron in ferritin. *BMC Systems Biology*, *4*, 147. https://doi.org/10.1186/1752-0509-4-147

Saponaro, A., Porro, A., Chaves-Sanjuan, A., Nardini, M., Rauh, O., Thiel, G., & Moroni, A. (2017). Fusicoccin activates KAT1 channels by stabilizing their interaction with 14-3-3 proteins. *Plant Cell*, *29*(10), 2570–2580. https://doi.org/10.1105/tpc.17.00375

Schenk, A., Ivanchenko, S., Röcker, C., Wiedenmann, J., & Nienhaus, G. U. (2004). Photodynamics of Red Fluorescent Proteins Studied by Fluorescence Correlation Spectroscopy. *Biophysical Journal*, *86*(1 I), 384–394. https://doi.org/10.1016/S0006-3495(04)74114-4

Schöbel, N., Radtke, D., Lübbert, M., Gisselmann, G., Lehmann, R., Cichy, A., Schreiner, B. S. P.,

Altmüller, J., Spector, A. C., Spehr, J., Hatt, H., & Wetzel, C. H. (2012). Trigeminal Ganglion Neurons of Mice Show Intracellular Chloride Accumulation and Chloride-Dependent Amplification of Capsaicin-Induced Responses. *PLoS ONE*, *7*(11). https://doi.org/10.1371/journal.pone.0048005

Shaya, D., Findeisen, F., Abderemane-Ali, F., Arrigoni, C., Wong, S., Nurva, S. R., Loussouarn, G., & Minor, D. L. (2014). Structure of a prokaryotic sodium channel pore reveals essential gating elements and an outer ion binding site common to eukaryotic channels. *Journal of Molecular Biology*, *426*(2), 467–483. https://doi.org/10.1016/j.jmb.2013.10.010

Splitt, H., Meuser, D., Borovok, I., Betzler, M., & Schrempf, H. (2000). Pore mutations affecting tetrameric assembly and functioning of the potassium channel KcsA from Streptomyces lividans. *FEBS Letters*, *472*(1), 83–87. https://doi.org/10.1016/S0014-5793(00)01429-0

Stanley, S. A., Gagner, J. E., Damanpour, S., Yoshida, M., Dordick, J. S., & Friedman, J. M. (2012). Radio-wave heating of iron oxide nanoparticles can regulate plasma glucose in mice. *Science*, *336*(6081), 604–608. https://doi.org/10.1126/science.1216753

Stanley, S. A., Kelly, L., Latcha, K. N., Schmidt, S. F., Yu, X., Nectow, A. R., Sauer, J., Dyke, J. P., Dordick, J. S., & Friedman, J. M. (2016). Bidirectional electromagnetic control of the hypothalamus regulates feeding and metabolism. *Nature*, *531*(7596), 647–650. https://doi.org/10.1038/nature17183

Stanley, S. A., Sauer, J., Kane, R. S., Dordick, J. S., & Friedman, J. M. (2015). Remote regulation of glucose homeostasis in mice using genetically encoded nanoparticles. *Nature Medicine*, *21*(1), 92–98. https://doi.org/10.1038/nm.3730

Stetefeld, J., McKenna, S. A., & Patel, T. R. (2016). Dynamic light scattering: a practical guide and applications in biomedical sciences. *Biophysical Reviews*, *8*(4), 409–427. https://doi.org/10.1007/s12551-016-0218-6

Taberner, F. J., Fernández-Ballester, G., Fernández-Carvajal, A., & Ferrer-Montiel, A. (2015). TRP channels interaction with lipids and its implications in disease. *Biochimica et Biophysica Acta - Biomembranes*, *1848*(9), 1818–1827. https://doi.org/10.1016/j.bbamem.2015.03.022

Tan, Q., Shim, J. W., & Gu, L. Q. (2010). Separation of heteromeric potassium channel Kcv towards probing subunit composition-regulated ion permeation and gating. *FEBS Letters*, *584*(8), 1602–1608. https://doi.org/10.1016/j.febslet.2010.03.023

Tatur, J., Hagedoorn, P. L., Overeijnder, M. L., & Hagen, W. R. (2006). A highly thermostable ferritin from the hyperthermophilic archaeal anaerobe Pyrococcus furiosus. *Extremophiles*, *10*(2), 139–148. https://doi.org/10.1007/s00792-005-0484-x

Watanabe, M., & Fukuda, A. (2015). Development and regulation of chloride homeostasis in the central nervous system. *Frontiers in Cellular Neuroscience*, *9*(September), 1–14. https://doi.org/10.3389/fncel.2015.00371

Wesolowski, J., Alzogaray, V., Reyelt, J., Unger, M., Juarez, K., Urrutia, M., Cauerhff, A., Danquah, W., Rissiek, B., Scheuplein, F., Schwarz, N., Adriouch, S., Boyer, O., Seman, M., Licea, A., Serreze, D. V., Goldbaum, F. A., Haag, F., & Koch-Nolte, F. (2009). Single domain antibodies:

Promising experimental and therapeutic tools in infection and immunity. *Medical Microbiology and Immunology*, *198*(3), 157–174. https://doi.org/10.1007/s00430-009-0116-7

Wheeler, M. A., Deppmann, C. D., Patel, M. K., & Güler, A. D. (2019). Reply to: Magneto is ineffective in controlling electrical properties of cerebellar Purkinje cells, Assessing the utility of Magneto to control neuronal excitability in the somatosensory cortex and Revaluation of magnetic properties of Magneto. *Nature Neuroscience*, *1*. https://doi.org/10.1038/s41593-019-0472-6

Wheeler, M. A., Smith, C. J., Ottolini, M., Barker, B. S., Purohit, A. M., Grippo, R. M., Gaykema, R. P., Spano, A. J., Beenhakker, M. P., Kucenas, S., Patel, M. K., Deppmann, C. D., & Güler, A. D. (2016). Genetically targeted magnetic control of the nervous system. *Nature Neuroscience*, *19*(5), 756–761. https://doi.org/10.1038/nn.4265

Yu, L., Lei, Y., Ma, Y., Liu, M., Zheng, J., Dan, D., & Gao, P. (2021). A Comprehensive Review of Fluorescence Correlation Spectroscopy. *Frontiers in Physics*, *9*(April), 1–21. https://doi.org/10.3389/fphy.2021.644450

Zagotta, W. N., Olivier, N. B., Black, K. D., Young, E. C., Olson, R., & Gouaux, E. (2003). Structural basis for modulation and agonist specificity of HCN pacemaker channels. *Nature*, *425*(6954), 200–205. https://doi.org/10.1038/nature01922

Zhang, F., Wang, L. P., Brauner, M., Liewald, J. F., Kay, K., Watzke, N., Wood, P. G., Bamberg, E., Nagel, G., Gottschalk, A., & Deisseroth, K. (2007). Multimodal fast optical interrogation of neural circuitry. *Nature*, *446*(7136), 633–639. https://doi.org/10.1038/nature05744

Zhang, G., Gurtu, V., & Kain, S. R. (1996). An enhanced green fluorescent protein allows sensitive detection of gene transfer in mammalian cells. *Biochemical and Biophysical Research Communications*, *227*(3), 707–711. https://doi.org/10.1006/bbrc.1996.1573

Declaration of own work

Experiments, data analysis, data representation and writing of the thesis were exclusively performed by myself with the exception of:

Addition of the temperature domain to KcvNTS: Design of the constructs was done together with Dr. Andrea Saponaro, who helped also in the design of single point mutations.

Functional test of v1 and v2 constructs: Whole cell recordings were performed by Dr. Federica Gasparri.

Iron content of ferritins extracted from HEK 293 cells: RICS experiments were performed by Dr. Gerardo Abbanondato.

EGFP-mFT contains 583 Fe atoms for each protein: ICP-OES experiments were performed by the group of Dr. Marco Schiavoni, with the support of Dr. Alessandro Caselli.

In general, Dr. Gerardo Abbandonato gave support in all the experiments involving confocal imaging, while Dr. Alessandro Porro gave support for the electrophysiology experiments.

Acknowledgments

I need to thank many people for the help and the support during this doctorate.

First of all, I want to thank Prof. Anna Moroni for the opportunity to spend these three great years in her lab, for her guidance within this challenging and intriguing project and for her passion for science, which inspires the people who work with her. I also need to thank Dr. Gerhard Thiel for giving me the opportunity to present my work in this university and for the precious help with thesis writing and results discussion.

The time passed in this lab made me grow not only as scientist but also as person. I know fell more confident and conscious of the skill I have gained. All this would not be possible without the people I met. Some of them are still in this lab, some of them have taken different lifepaths but in every case I joyfully keep the company that they have made me during this journey. They have transformed laboratory life into family life and for this I will never thank them enough. I hope that the friendships created in these years will be maintained, regardless of which path each one will take. I don't want to mention each member of the laboratory one by one because they have all been important for me and I would risk to forget someone. I will therefore say a general thanks to all those who accompanied me to the end of this journey. You made this experience incredibly beautiful.

Curriculum Vitae

Personal information

Name	Lorenzo Brocca
Date of birth	19/09/1991
Place of birth	Milano (MI), Italy
Nationality	Italian

Academic career

10/2015 – 02/2018	**Master degree** in Industrial Biotechnology University of Milano-Bicocca, Milano (MI), Italy Faculty of Bioscience and Biotechnology Thesis title: Gamma zeins, *Zea mays* insoluble storage proteins, but not Phaseolin, *Phaseolus vulgaris* soluble storage proteins, induce the Unfolded Protein Response (UPR). Final score: 110/110 cum laude
10/2011 – 07/2015	**Bachelor degree** in Biotechnology University of Milano-Bicocca, Milano (MI), Italy Faculty of Bioscience and Biotechnology Thesis title: Vitamin D as an antitumoral agent. Polymorphisms in the vitamin D receptor gene associated with breast cancer risk. Final score: 92/110

Conference contributions

02/2021	Author of the abstract "A screening strategy to improve surface expression of the synthetic channel BLINK2 in mammalian cells" presented at the Biophysical society 65th Annual Meeting (February 22-26, 2021, virtually).
09/2018	Presentation of the Poster “Towards the engineering of a magneto sensitive potassium channel” at the International Symposium Ion channel design using experimental and computational inputs, Gargnano (BS) Italy 10TH-12TH September 2018
09/2017	Presentation of the poster "Gamma-zeins, but not phaseolin, trigger the endoplasmic reticulum unfolded protein response" at two congress: 1) European Network for Plant Endomembrane Research (ENPER), Prague, 12TH-15TH SEPTEMBER, 2017 2) Joint congress SIBV-SIGA "Sustainability of agricultural environment: contributions of plant genetics and physiology", Pisa, 19TH-22ND SEPTEMBER, 2017

Ehrenwörtliche Erklärung

Ich erkläre hiermit ehrenwörtlich, dass ich die vorliegende Arbeit entsprechend den Regeln gutter wissenschaftlicher Praxis selbstständig und ohne unzulässige Hilfe Dritter angefertigt habe.

Sämtliche aus fremden Quellen direkt oder indirekt übernommenen Gedanken sowie sämtliche von Anderen direkt oder indirekt übernommenen Daten, Techniken und Materialien sind als solche kenntlich gemacht. Die Arbeit wurde bisher bei keiner anderen Hochschule zu Prüfungszwecken eingereicht.

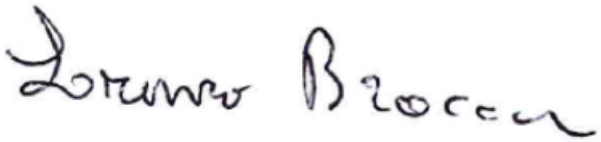

Milano, den 29.07.2021